University of California
Berkeley
Seismological Laboratory

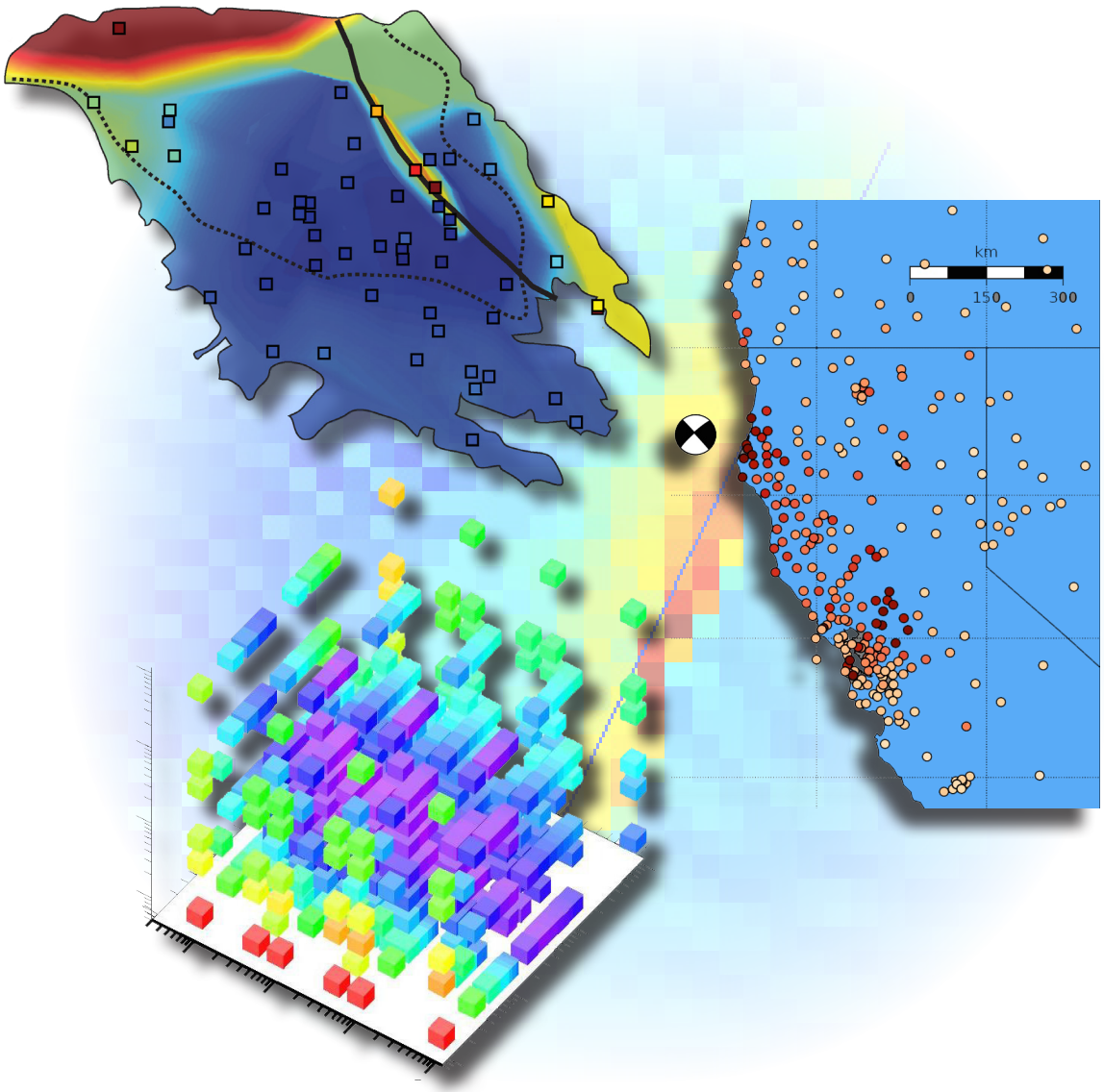

Annual Report

July 2013–June 2014

Berkeley Seismological Laboratory

Annual Report
July 2013—June 2014

Contents

Chapter 1

Director's Report

Highlights

It is a great pleasure to present this year's Berkeley Seismological Laboratory (BSL) Annual Report—my third report as Director. Each year it is exhilarating to be reminded of the wide range of BSL activities, as captured in these pages. This year we are also delighted to be **ranked number 1 in Geophysics and Seismology** for the first time by US News and World Reports. This is a ranking based on surveys sent to academics in the field. I see this as an acknowledgement of the dynamic and wide-ranging research program fostered by BSL faculty, researchers and students. The BSL is also unique for our cutting-edge geophysical observing facility that includes broadband and strong-motion seismometers, high-rate real-time GPS, and borehole instrumentation along active faults. Spanning both the research and network-facility realms, BSL provides an environment in which the extramural research program is strengthened and broadened by the facility, and the facility continues to push the boundaries of terrestrial observations in response to research needs. In addition, the BSL continues to reach out and connect with the consumers of our data and our science. These include researchers around the world, students, the public, and private or public sector institutions with a need and desire for an improved understanding of solid Earth processes.

In my report this year I highlight three of BSL's ongoing activities. The first is the wide reach of the BSL datasets as I review who is downloading data from our data center. Secondly, I want to highlight the progress that we have made toward building a public earthquake warning system for the United States. I will then provide a quick overview of the range of two-page research contributions in this year's report. Personnel news, a review of our facilities, and acknowledgements follow.

Firstly, the reach of BSL data resources. The BSL geophysical networks—which I highlighted in my report last year—include our broadband and strong motion seismic network (the Berkeley Digital Seismic Network, BDSN), the real-time GPS network (the Bay Area Regional Deformation Network, BARD), and our borehole seismic networks along active faults focused in the Parkfield area of central California and the Bay Area. When possible and appropriate, these different instrument types are co-located. In sum, our geophysical instrumentation occupies about 70 locations across Northern California (See Figure 1.1). Data from all these sites stream into our real-time processing center here at UC Berkeley and are used to provide rapid earthquake information. In addition, all the data are archived at the Northern California Earthquake Data Center (http://ncedc.org/) here at UC Berkeley, and delivered openly and immediately to the scientific community around the world. The study of solid Earth deformation requires long-term data collection for periods of decades, while also providing high sample rates—up to hundreds of samples per second—in order to capture the details of sudden, rapid events such as earthquakes. The NCEDC provides this service for the research community.

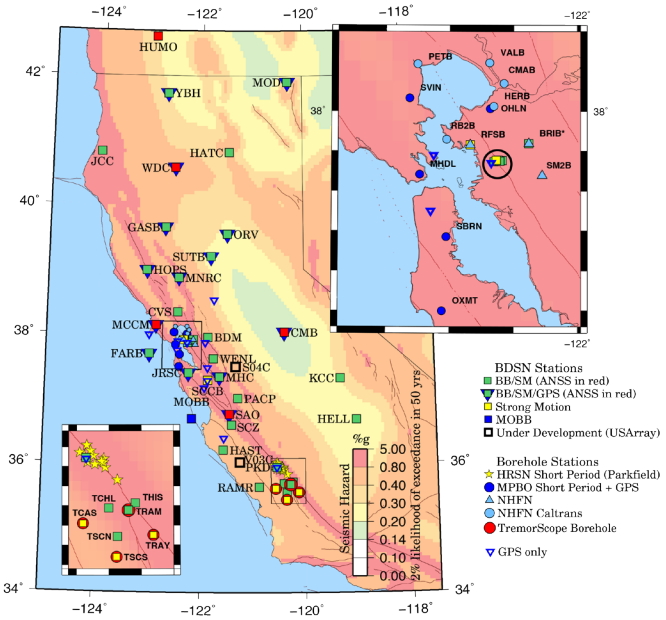

Figure 1.1: The BSL geophysical network. The color scale shows seismic hazard. The colors represent a percent of the acceleration due to gravity that has greater than a 2% probability of exceedance in the next 50 yers.

With the BSL networks we strive for extremely high-quality datasets. This means that the instruments are installed in high-quality, low-noise vaults. Extensive quality control is applied to our data to identify any deterioration of the instrumentation and remedy it immediately. The BDSN network boasts 99.23% data completeness for the 2013–2014 fiscal year. Also, 67% of the stations have a single data segment for the year, meaning that not a single data sample was lost. This level of completeness is unrivaled by any other seismic network and allows researchers to study very long-term deformation processes that have very small detectable signals.

In addition to archiving data from the BSL networks, the NCEDC archives data from all the major geophysical networks in Northern California, including networks operated by the US Geological Survey, the California Department of Water Resources, PG&E, and Calpine. The total size of the NCEDC digital archive today is 80 Tb, and data extend back to 1984, however, records extend all the way back to 1887, when UC Berkeley installed the first seismometers in the western hemisphere, and paper records—which are still periodically used by visiting scientists—go back to 1910. In the past year we added 10 Tb to the archive. The data are freely available via a range of tools, including a new suite of tools, "web services", developed over the last few years, that make use of the http-type requests to access

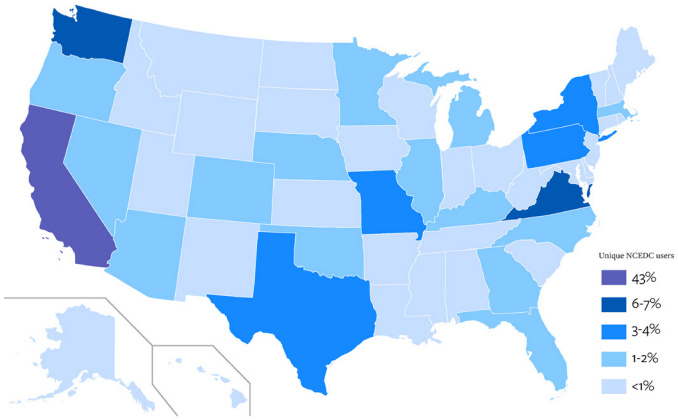

Figure 1.2: The distribution of NCEDC users as a percentage of the total US users for 2013–2014.

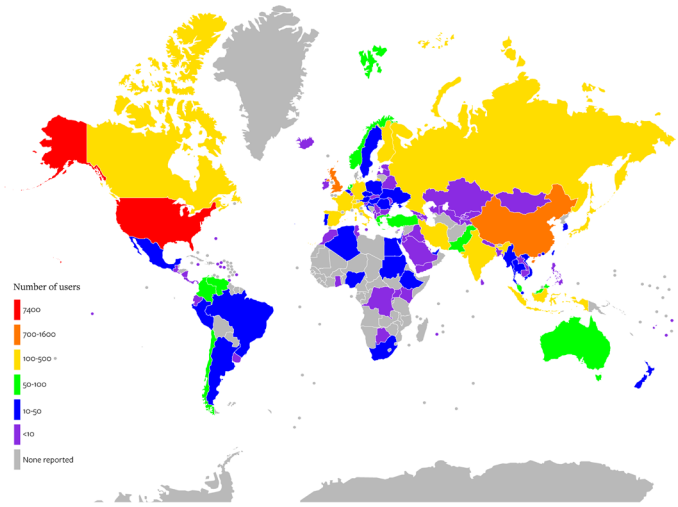

Figure 1.3: The distribution of NCEDC users worldwide colored according to total number of users on a per country basis for 2013–2014.

timeseries data and all associated metadata. For the past year we have compiled a list of people downloading data from the NCEDC. As some of the older data access tools do not allows us to track users, the list is incomplete. Still, we identified over 14,000 users. Figures 1.2 and 1.3 show the distribution of these users. Not surprisingly, the greatest number of users is here in the US, and specifically in California. However, the global reach of the data is remarkable. There are many users in Russia, China, Germany, the UK, India, Canada, Iran, Japan, France, Italy, Spain, Australia and Indonesia. There are also smaller numbers of users in dozens of other countries on every continent except Antarctica. While the funding for our geophysical network facility is primarily driven by the need for real-time earthquake hazard information in Northern California, the high-quality data we produce and archive are then used for a plethora of research activities that are truly global.

The second topic I would like to highlight is progress towards a public earthquake early warning (EEW) system. This past year has seen rapid progress towards a system for the west coast of the Unites States. The BSL has been involved in developing the capabilities for early warnings since 2005 both with active research programs and though leadership in the collaborative effort. At the beginning of this past year, Governor Jerry Brown signed into law the EEW legislation introduced by Senator Alex Padilla. The legislation calls for a statewide EEW system but does not allocate funding, instead calling on the Governor's Office of Emergency Services to identify sources of funding. At the end of this review year, the House Appropriations Committee in Washington DC included partial EEW funding in their FY2015 appropriation. The cost of building and operating a west coast system for the first 5 years is $120M, and while there is still much work to be done to obtain full funding, these were both significant steps forward.

This year has also seen significant technical progress with EEW. In March and April a series of earthquakes were felt across the Los Angeles region, the largest being the March 28, 2014, M5.1 La Habra earthquake. Recent improvements to the seismology-based ElarmS EEW methodology—developed here at BSL and now operating along the entire U.S. west coast—provided the first alerts for all of the earthquakes associated with this sequence. While the time needed to process the data still means that it was not possible to generate an alert for the epicentral region, the vast majority of Angelenos shaken by these quakes could have received a warning (Figure 1.4, see http://youtu.be/Lt7aBD4CUIQ). Also, our real-time GPS-based EEW methodology, named G-larmS, is now operational and is undergoing testing on the real-time system in Northern California. It uses the BSL's BARD network along with other GPS stations across the region to detect permanent displacements generated by earthquakes. A rapid inversion solves for the distribution of slip on the identified fault plane and provides a magnitude estimate that is more robust than seismology-based estimates for big (M>7) earthquakes.

The EEW project is an example of the synergies produced when active research programs are brought together with cutting-edge observational facilities, and where there are also direct interactions with consumers of hazard information. The arc of the project started with a few researchers and computers, asking the question of how quickly the magnitude of an earthquake can be determined. It progressed through initial, pseudo-real-time testing to full implementation on the real-time system in California. Now, while the research and development continues, BSL staff are talking to public and private sector entities about how best to use earthquake alerts. Legislators have taken note of the important implications of this new hazard-reduction capability, and are enacting legislation to support it at state and federal levels. BSL researchers and staff are, of course, supporting these efforts. Finally, all of this is only possible thanks to the close collaboration between BSL, Caltech, University of Washington, ETH Zürich, SCEC, the Gordon and Betty Moore Foundation and the U.S. Geological Survey.

Having highlighted the NCEDC and the EEW project, I want to provide a summary of the wide-ranging research conducted at the BSL. The active research efforts of the students, postdocs, researchers, faculty and visitors are at the heart of BSL activities. Section 2 of our report contains 36 research summaries describing ongoing projects. The research groups headed by nine of our faculty members have contributed to this year's report. The topics covered fall into five broad categories:

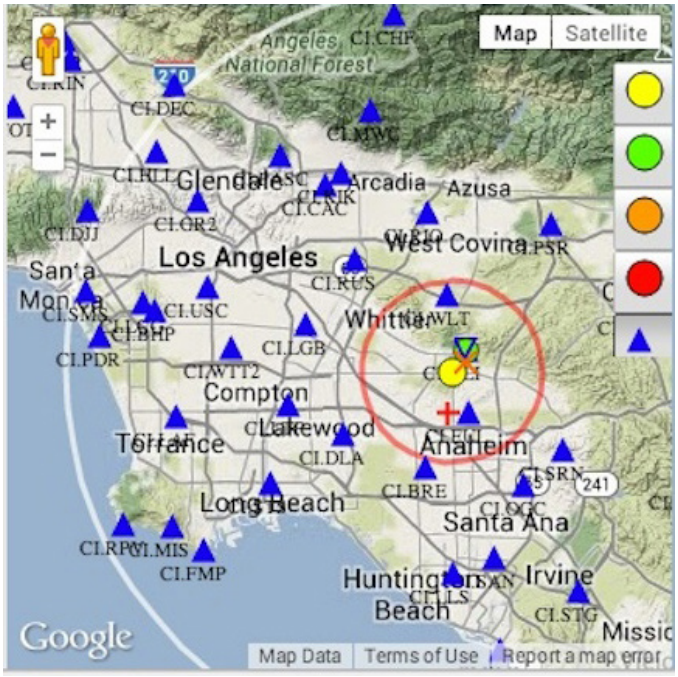

Figure 1.4: The red circle on this map of Southern California shows the area that would not have received alerts for the *M*5.1 La Habra earthquake. This is the so called blind zone caused by computational time and station density limitations.

1. The Mineral Physics section includes experimental and numerical experiments on the properties of minerals found in the Earth's crust and mantle, and on the miscibility of terrestrial materials in the early Earth. The effects of permafrost on seismic velocity are also described in this section.

2. The Earth Structure section includes new regional and global studies of structure and processes. Our focus on North America continues with studies of the Juan de Fuca plate and the Canadian Craton, while global imaging provides ever-improved constraints on upwelling and downwelling features in the mantle. New receiver function methods to constrain discontinuity structure are being developed, to improve imaging in complex regions, and across entire oceans.

3. The Rheology and Fault Mechanics section includes studies of deformation across Tibet, Japan and California as well as the more local process of land sliding. The links between hydrologic processes, seismicity and landslides are also explored in China and California. Fault processes are also investigated through triggering, repeating earthquakes and micro-seismicity on faults.

4. The Seismic Source section begins with a study of intraslab seismicity following the Tohoku-Oki earthquake. Seismic source characterization continues with studies of a sinkhole, the Geysers geothermal region and shallow seismicity. The final study in the section describes an effort to improve our ability to characterize offshore-seismicity on the Juan de Fuca plate.

5. Various research efforts contribute to improving observational capabilities. This year's Enhancements to Observational Systems research papers include a summary of both the seismic (ElarmS) and geodetic (GlarmS) earthquake early warning algorithms we are developing. A description of how we are using smartphone accelerometers to detect earthquakes, and observations of shaking amplification effects in data from high-rate GPS. Also, the application of InSAR to assessing aquifer changes, using data from borehole instrumentation to detect tremor on the San Andreas Fault, and assessing instrument quality using normal modes.

Many of these research efforts are stimulated and inspired by our facilities. These include our geophysical networks that continuously collect a variety of data from across Northern California, and the NCEDC that delivers the data to researchers around the world and within the BSL. More information about these networks and their development can be found in the Facilities Review below.

BSL Personnel News

One new PhD graduate student, William Hawley, and two Postdoctoral Fellows, Marco Calo and Estelle Chaussard joined the lab during the 2013-14 academic year. Three PhD students graduated, their names and thesis titles were: Mong-Han Huang, "Crustal Deformation During Co- and Postseismic Periods"; Zhao Zheng (Allen), "Refining Constraints on Seismic Discontinuities and Elastic Structure in the Earth's Upper Mantle"; and Scott French, "Global Full-Waveform Tomography using the Spectral Element Method: New Constraints on the Structure of Earth's Interior". Graduate student Ryan Turner completed his MS thesis entitled "Exploration of Slip Rate Variation on the Central San Andreas Fault Using Repeating Earthquakes and Geodesy". Three of our Postdoctoral Fellows moved on to new positions elsewhere. Serdar Kuyuk took up a faculty position at Sakarya University, Turkey. Lingsen Meng is now an assistant professor at UCLA, and Ronni Grapenthin will be starting as an assistant professor at New Mexico Tech in the Fall 2014 semester.

The BSL also continued to provide a range of research projects for undergraduate students, two of whom have contributed research reports. This year's cohort consisted of Rohan Agarwal, Amanda Atkinson, Joel Bai, Michael Faggetter, James Hoenig, Voon Hui Lai, Frances (Julie) Leiva, Brenda Luna, and Michael Tran.

As usual, a stream of visitors spent varying amounts of time at the lab. These included Pierre Clouzet from IPG Paris, and Yuzhu Liu from Tongji University visiting Barbara Romanowicz's group; Seung-Hoon Yoo visiting Doug Dreger's group, and Men-Andrin Meier and Yannick Behr from ETH Zürich visiting my group.

During the year one staff member retired, Gretchen vonDuering, who has been providing HR support to the BSL for the past few years. We had one new arrival, that of Steve Allen who joined the IT group. During the year, the BSL also transitioned into the new Campus Shared Services (CSS) model for administrative support. As a result several staff moved into CSS including Matt Carli (purchasing) and Marion Banks (travel). Our research administration staff, Clarissa Foreman and Raluca Iordache, also became part of CSS but remain located in McCone Hall. Judith Coyote (department manager) and Dawn Geddes (financial analyst) remain part of the BSL.

Facilities Review

The Berkeley Seismological Laboratory (BSL) is an Organized Research Unit (ORU) on the UC Berkeley campus. Its mission is unique in that, in addition to research and education in seismology, geophysics, and earthquake-related science, it is responsible for providing real-time earthquake information. This information is required by the UC Berkeley constituency, various local and state governments and private organizations including emergency response, and is consumed by the general public. The BSL is therefore both a research center and a facility/data resource, which sets it apart from most other ORUs. A major component of our activities is focused on developing and maintaining several regional observational networks, and participating, along with other agencies, in various aspects of the collection, analysis, archival, and distribution of data pertaining to earthquakes, while maintaining a vigorous research program on earthquake processes and Earth structure. In addition, the BSL staff spend considerable time on public relations activities, including tours, talks to public groups, response to public inquiries about earthquakes, and an informational web presence (http://earthquakes.berkeley.edu/).

UC Berkeley installed the first seismograph in the Western Hemisphere at Mount Hamilton (MHC) in 1887. Since then, it has played a leading role in the operation of state-of-the-art seismic instruments and in the development of advanced methods for seismic data analysis and interpretation. Notably, the installation, starting in 1927, of Wood-Anderson seismographs at four locations in Northern California (BKS, ARC, MIN, and MHC) allowed the accurate determination of local earthquake magnitude from which a unique historical catalog of regional earthquakes has been maintained to this day, providing crucial input to earthquake probability studies.

Over the years, the Berkeley Seismographic Stations (BSS), as the BSL was then called, continued to drive technological improvements. The first centrally telemetered network using phone lines in an active seismic region was installed by BSS in 1960. The BSS was the first institution in California to operate a three-component "broadband" system (1963). It played a major role in the early characterization of earthquake sources using "moment tensors" and source-time functions. The BSS also made important contributions to the early definitions of detection/discrimination of underground nuclear tests and, jointly with UCB Engineering, to earthquake hazards work.

Starting in 1986, the BSS acquired four state-of-the-art broadband instruments (STS-1), while simultaneously developing PC-based digital telemetry. These two developments laid the groundwork for the modern networks we operate today. As telecommunication and computer technologies made rapid progress, in parallel with broadband instrument development, paper record reading was abandoned in favor of automated analysis of digital data. One paper-based helicorder does remain operational, primarily for the press and visitors to view.

Today, the BSL's networks can be divided into three groups of instrumentation that are deployed at a total of ~70 sites across Central and Northern California. The instrumentation types predominantly consist of broadband plus strong motion seismic, borehole seismic, and GPS equipment, and are often co-located when appropriate. Data from all instrumentation stream continuously into the BSL's real-time monitoring system which provides earthquake warnings, notification and characterization. It is also delivered to the archive where it can be accessed immediately by researchers from around the world for scientific study.

The Berkeley Digital Seismic Network (BDSN) is our regional seismic network of about 40 sites where both broadband and strong motion seismic instrumentation is installed. This network is the backbone of the BSL's operations, feeding the necessary data for real-time estimation of location, size and rupture parameters for earthquakes in Central and Northern California. This network has been steadily growing since the 1990's and consists of very high quality, low-noise sites, making the data ideal for a range of research efforts. The array can be used to study local or global earthquake sources, and provides data for investigation of 3D crustal structure in California and its effects on regional waveform propagation, which in turn affect the intensity of ground shaking in larger earthquakes. Recent additions to the network include an ocean bottom seismometer in the Monterey Bay (MOBB) providing real-time data via an undersea cable (operated in collaboration with MBARI), and also the Tremorscope stations along the Cholame section of the San Andreas Fault just south of Parkfield.

The real-time data are also Berkeley's contribution to the California Integrated Seismic Network (CISN), which is a federation of networks that jointly provide all real time earthquake information in the state. Since 1996, the BSL and the USGS in Menlo Park have closely cooperated to provide the joint earthquake notification program for Northern California. This program capitalizes on the complementary capabilities of the networks operated by each institution to provide rapid and reliable information on the location, size and other relevant source parameters of regional earthquakes. The real-time earthquake information is made available through the BSL's website (http://earthquakes.berkeley.edu).

The BSL's borehole networks represent the second grouping of instrumentation. The High Resolution Seismic Network (HRSN) was installed in 1987 and now consists of 12 operating sites. Additional borehole sites will soon be added as part of the Tremorscope project (see Research Section 2.34). These instruments have led to wide-ranging research into earthquake processes due to their high sensitivity, low noise, and proximity to micro-earthquakes, earthquake clusters and tremor sources along the highly studied Parkfield section of the San Andreas Fault (see Research Section 2.23). In the Bay Area, the Hayward Fault Network also includes 15 borehole instruments that have been installed progressively since the 1990s. The goal of this network is again to collect high signal-to-noise data for micro-earthquakes along the Hayward Fault to gain insight into the physics that govern fault rupture and its nucleation.

The third instrumentation type is GPS. The BSL operates the Bay Area Regional Deformation (BARD) Network consisting of 32 primary sites, 18 collocated with BDSN seismometers. All sites record with a 1 Hz sample rate and telemeter the data to the BSL in real time. Continuous GPS data track the motion of the

tectonic plates and allow us to assess the strain buildup along faults as well as its release either through creeping episodes or through earthquakes. The application of GPS data feeds to real-time earthquake information is also a relatively new development. Very rapid processing now generates displacement waveforms that in turn support the development of improved real-time earthquake analysis methods for significant earthquakes.

The BSL's IT group is active in the development of new software for the collection, archival and real-time analysis of the various geophysical data streams that we collect. In 2009, the new AQMS seismic network software package was rolled out following a multi-year development effort by the BSL in collaboration with other CISN partners. This software provides all the real-time processing components needed by regional seismic networks and is now being rolled-out across the US. The development of real-time GPS processing software is a current area of focus for the lab along with development, testing and implementation of earthquake early warning algorithms that can process data quickly enough to provide alerts to people a few seconds to tens of seconds before shaking is felt.

Archival and distribution of data from the BSL and other regional geophysical networks is performed at the Northern California Earthquake Data Center (NCEDC), operated at the BSL in collaboration with USGS Menlo Park. The data reside on a mass-storage device (current holdings ~80 Tb), and are accessible online (http://www.ncedc.org). In addition to BSL network data, data from the USGS Northern California Seismic Network (NCSN), and other northern California networks, are archived and distributed through the NCEDC. The NCEDC also maintains, archives and distributes various earthquake catalogs.

Finally, the field engineering team is responsible for maintaining our existing ~70 geophysical observatories across Northern California, and designing and installing new sites. Of particular note is the completion in 2011 of the ARRA-funded upgrades. These urgently needed equipment upgrades replaced aging dataloggers at almost all BSL observatories, providing more robust and more rapid transmission of data from the sites to the BSL real-time system. The group is now focused on the design and installation of the new Tremorscope borehole and surface stations just south of Parkfield along the Cholame section of the San Andreas Fault, and on upgrading the HRSN.

All of these operations are supported by an operations and research staff of nine, an IT staff of eight, and an engineering staff of three. Our administrative support group is largely shared with the Department of Earth and Planetary Science and consists of six, with additional support provided by Campus Shared Services. In addition, there are currently three Postdoctoral Scholars and fifteen PhD graduate students associated with the lab, along with eighteen affiliated faculty.

The BSL budget is made up of approximately 50% extramural research support and 50% facility/operations support. The operations/facility support comes from the university, the USGS, the state and several other external sources. Core University funding to our ORU currently provides salary support for one staff scientist (shared by three researchers), one IT staff member, one engineer, 50% of our operations manager, and one administrative assistant. University support represents about one fifth of the total infrastructure support budget. The remaining support comes from extramural grants and contracts, primarily from the USGS, DOE, NSF, and the State of California, through its Office of Emergency Services (CalOES). Currently, grants from the Gordon and Betty Moore Foundation contribute significantly to our operations as do the contributions from the members of our Earthquake Research Affiliates Program.

Acknowledgements

I would like to thank our technical and administrative staff, scientists and students for their efforts throughout the year and their contributions to this annual report. In particular I would like to thank our affiliated faculty, whose research groups are contributing to this report: Professors Roland Bürgmann, Doug Dreger, Raymond Jeanloz, Michael Manga, Burkhard Militzer, Barbara Romanowicz, Chi-Yuen Wang and Rudy Wenk. Individual contributions to activities and report preparation are mentioned in the corresponding sections, except for the appendix sections, which were prepared by Clay Miller.

The BSL Advisory Committee plays an important role providing feedback and guidance on BSL activities and priorities. The committee members are Prof. Steven Glaser (Chair – Civil and Environmental Engineering, UC Berkeley), Prof. Josh Bloom (Astronomy, UC Berkeley), Dr. Thomas Brocher (US Geological Survey), Prof. Michael Manga (Earth and Planetary Science, UC Berkeley), Prof. John Vidale (University of Washington).

I also wish to especially thank the individuals who have regularly contributed to the smooth operation of the BSL facilities: Steve Allen, Mario Aranha, Doug Dreger, John Friday, Peggy Hellweg, Ivan Henson, Ingrid Johanson, Clay Miller, Josh Miller, Pete Lombard, Bob Nadeau, Doug Neuhauser, Charley Paffenbarger, Jenn Strauss, Sarah Snyder, Jennifer Taggart, Taka'aki Taira, Stephen Thompson, Bob Uhrhammer, and Stephane Zuzlewski, and, in the administrative office, Crysthel Catambay, Judith Coyote, Clarissa Foreman, Dawn Geddes, Raluca Iordache and Hanna Knight.

I am particularly grateful to Clay Miller, Jennifer Taggart, Jenn Strauss and Peggy Hellweg for their help in putting together this annual report and bringing it to completion.

The Annual Reports of the Berkeley Seismological Laboratory are available on the web at http://earthquakes.berkeley.edu/annual_report.

Chapter 2

Research Studies

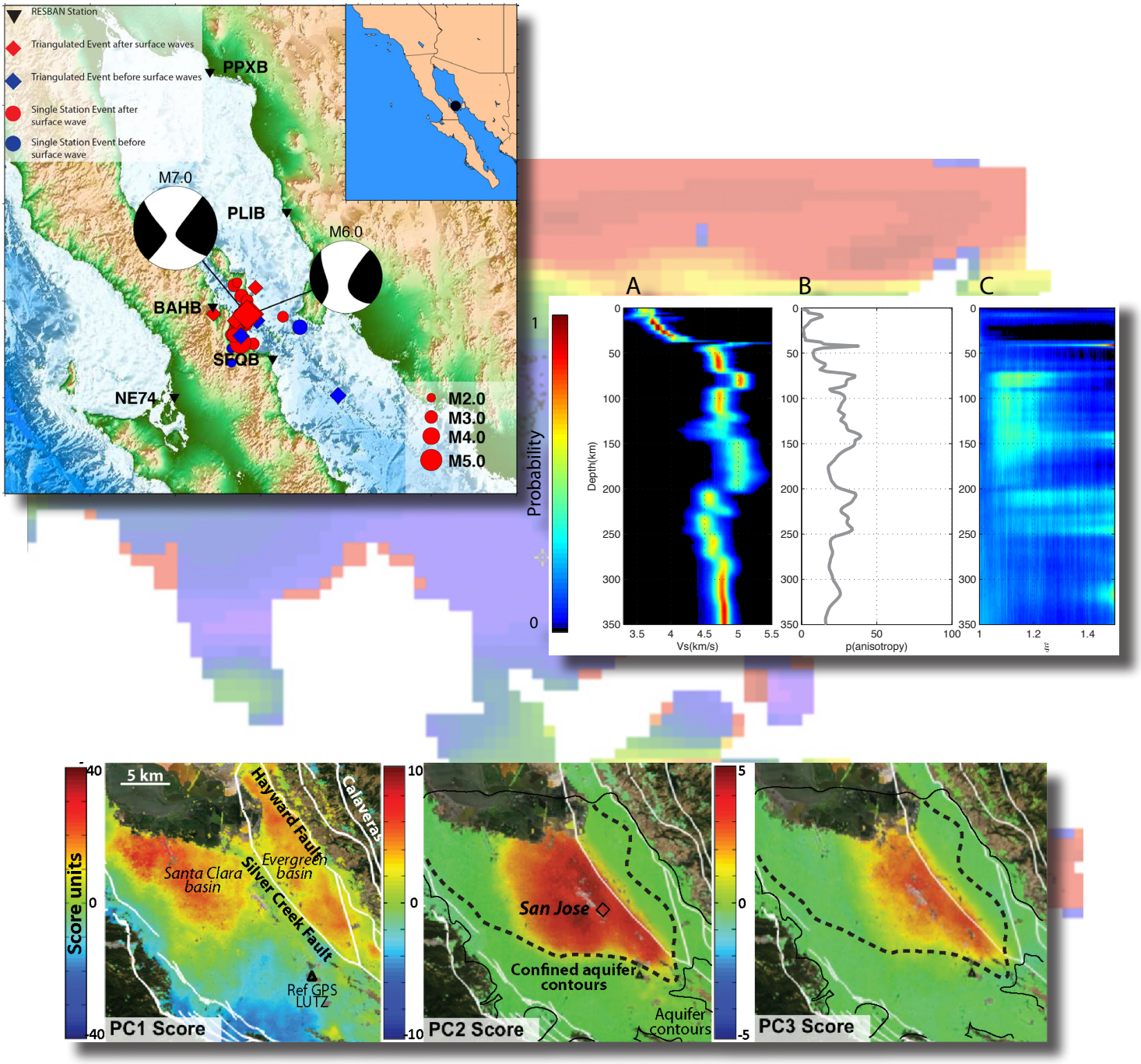

Research Studies:
Mineral Physics

1 *In Situ* Deformation of MgO and $MgSiO_3$ Perovskite: Lower Mantle Implications

Eloisa Zepeda-Alarcon, Pamela M. Kaercher, Hans-Rudolf Wenk

Introduction

Knowledge of deformation of mantle minerals is important for understanding geodynamic implications of seismic data and constraining geophysical modeling. The pursuit to characterize and understand the Earth's interior has been a long standing topic in Earth science. Particularly, there is seismic evidence that there are regions of elastic anisotropy in the mantle (*Panning & Romanowicz*, 2006), and there has been great discussion as to what physical mechanisms are responsible for it (*Mainprice*, 2007). In the upper mantle, seismic anisotropy has been correlated to subduction zones and attributed to the crystallographic preferred orientation (CPO) of olivine as a consequence of the high strains imprinted by subduction (*Long*, 2013). Mineral physics has confirmed the development of CPO in olivine using, for example, a radial diamond anvil cell (rDAC) up to pressures comparable to those of the mantle (*Wenk et al.*, 2004). In the mantle transition zone, seismic anisotropy has been attributed to CPO of wadsleyite (*Kawazoe et. al.*, 2013). The core mantle boundary is a region with strong elastic anisotropy. It has been shown that the observed texture of the mineral phase post-perovskite could explain the measured seismic anisotropy of the region (*Wenk et. al.*, 2011).

There is strong evidence that the bulk composition of the upper and lower mantle are similar, which leads us to believe that the velocity contrast between these two regions is mainly due to the phase transition of olivine $(Mg,Fe)_2SiO_4$ to perovskite $(Mg,Fe)SiO_3$ and ferropericlase (Mg,Fe)O (*McDonough & Sun*, 1995). Studies on $MgSiO_3$ perovskite show that dislocation creep is present at pressures and temperatures of the uppermost lower mantle, implying the possibility of the development of CPO in these conditions (*Cordier et. al.*, 2004). Also, polycrystalline MgO develops noticeable anisotropy at pressures found at the uppermost lower mantle (*Merkel et. al.*, 2002). However if two phases occur together, stronger perovskite and weaker ferropericlase, the deformation behavior is much more complex and this has not been previously investigated in detail.

Here we present two-phase deformation experiments of perovskite and MgO aggregates at pressures of the lower mantle (up to 54 GPa). In these experiments we quantify the amount of CPO developed by certain crystallographic planes. We can then do modeling with the visco plastic self-consistent (VPSC) code to predict what slip system activity could be responsible for the observed CPO. Knowledge of the slip system activity and resulting CPO of the aggregate can inform the interpretation of seismic models as to what flow patterns can be attributed to the measured seismic anisotropy, and also to make predictions of the expected CPO through geodynamic modeling.

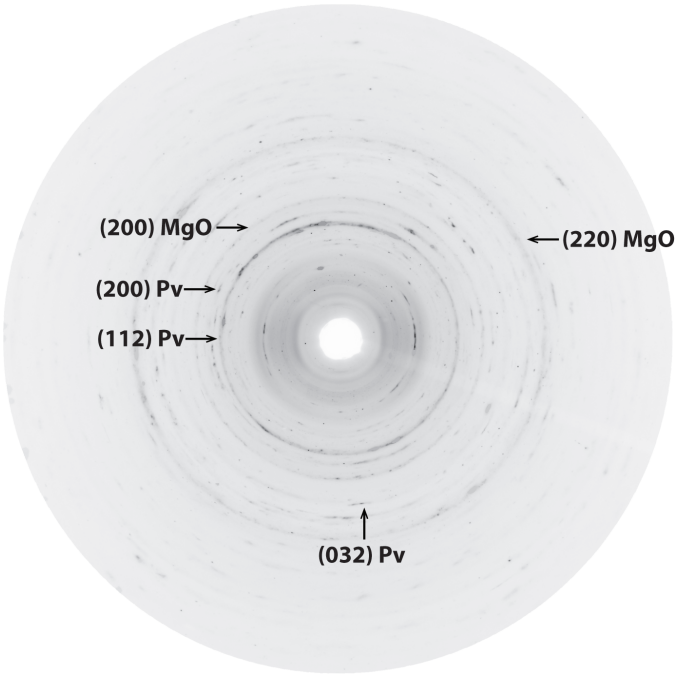

Figure 2.1.1: Raw diffraction image from MAR3450 detector at the Advanced Photon Source of Argonne National Lab. Diffraction of monochromatic X-rays off certain crystallographic plains, *e.g.* (200) of MgO and perovskite (Pv), generate Debye rings shown here.

Experiment and Analysis

To achieve pressures comparable to those of the lower mantle, these experiments were done in a diamond anvil cell in the radial geometry (rDAC) (*Wenk et. al.*, 2006). A mixture of enstatite and MgO was ground to a fine powder and loaded to a boron epoxy gasket on the rDAC. A gas membrane that inflates and pushes on the rDAC increases the pressure in the sample chamber. The enstatite and MgO mixture was brought up to about 30 GPa and then laser heated to induce a phase transformation to perovskite and MgO. This aggregate was then further deformed up to 54 GPa. The CPO developed by the aggregate due to the uniaxial stress imposed by the diamond anvils is assessed using synchrotron radiation to record the full Debye rings (Figure 2.1.1). The pressure is increased *in situ* and diffraction images are recorded at every pressure step. If CPO is present there will be a systematic intensity variation along a single Debye ring. The analysis of this intensity was done using the software MAUD (*Lutterotti & Bortolotti*, 2003), where an orientation distribution is calculated and an inverse pole figure of the compression direction can be plotted.

Results and Discussion

We have found that, in general, the two-phase system develops a weaker CPO than if the two phases are deformed separate-

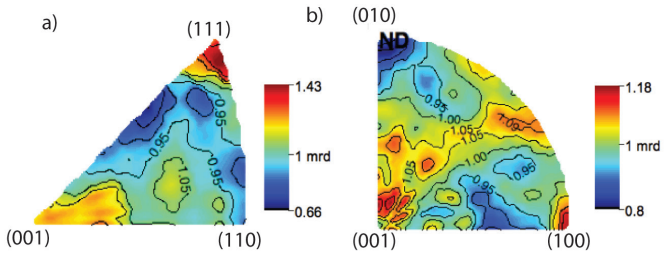

Figure 2.1.2: a) MgO inverse pole figure of the compression direction at 54 GPa. Shows how poles of the (111) crystallographic planes of MgO preferably align in the compression direction. b) Perovskite inverse pole figure of the compression direction at 54 GPa in the same sample chamber as MgO. The (001) and (100) align preferrably in the compression direction. Scale is shown in multiples of random distribution (mrd).

ly (*e.g. Merkel et. al.*, 2002; *Wenk et. al.*, 2004), this could explain why the bulk of the lower mantle is fairly isotropic. The MgO develops texture about 2 times stronger than the perovskite (Figure 2.1.2). Through a Rietveld analysis it was found that MgO preferably aligns poles of the (111) planes parallel to the compression direction and that the perovskite develops a weak (001) and (100) texture in the compression direction (Figure 2a and b). It is important to do these experiments with the two phases together since the hardness contrast between them can change the deformation of the aggregate. Particularly, it is expected that when a soft and a harder phase deform together, the soft phase will absorb deformation and the hard phase will deform very weakly and develop little crystallographic preferred orientation. This is consistent with our results since it is the MgO that has the stronger texture (Figure 2a). Previous rDAC deformation experiments on single-phase polycrystalline MgO found a strong (100) texture at 35.4 GPa (*Merkel et. al.*, 2002). Not only is the texture found in this study much weaker but it is of a different crystallographic plane, implying a different slip system activity. The perovskite texture in Figure 2.1.2b is comparable in orientation but weaker than the one found in a single-phase perovskite powder sample at 43 GPa in *Wenk et. al.*, 2004.

Further work is to model the two-phase system under compression with the VPSC code to see what possible combinations of slip systems and their activities might be responsible for the CPO observed in the experiments. It is also possible to model what the expected shear and compression wave velocities (V_s and V_p) are for the aggregate in different directions.

The study of the deformation of these lower mantle minerals is key in understanding seismic signatures from the mantle transition zone and the core mantle boundary (*e.g. Cottaar et. al.*, 2014), both very important and controversial regions of the mantle.

Acknowledgements

Use of the Advanced Photon Source, an Office of Science User Facility operated for the U.S. DOE Office of Science by Argonne National Laboratory, was supported by the U.S. DOE under Contract No. DE-AC02-06CH11357. E. Z.-A. and P.M.K. were supported in part by the Carnegie/DOE Alliance Center (CDAC) which is part of the Stewardship Science Academic Program of DOE/NNSA, Cooperative Agreement DE-NA0002006. Authors acknowledge support from NSF EAR 1343908.

References

Cordier P., Ungar T., Zsoldos L. and Tichy G., Dislocation creep in $MgSiO_3$ perovskite at conditions of the uppermost mantle, *Letters to Nature*, v. 428, p. 837-840, 2004/

Cottaar S., Li M., McNamara A., Romanowicz B., Wenk H.-R., Synthetic seismic anisotropy models within a slab impinging on the core-mantle boundary,*Geophysical Journal International*, *submitted*, 2014.

Kawazoe T., Ouchi T., Nishihara Y., Nishiyama N. and Fujino K., Seismic anisotropy in the mantle transition zone induced by shear deformation of wadsleyite, *Geophysical Journal International*, v. 216, p. 91-98, 2013.

Long M.D., Constraints on subduction geodynamics from seismic anisotropy, *Reviews of Geophysics*, v. 51, p. 76-112, 2013.

Lutterotti L., Matthies S., Wenk H.-R., Schultz A.S. and Richardson J.W. Jr., Combined texture and structure analysis of deformed limestone from time-of-flight neutron diffraction spectra, *Journal of Applied Physics*, v. 81, no. 2, p. 594-600, 1997.

Mainprice D., Seismic Anisotropy of the Deep Earth from a Mineral and Rock Physics Perspective, *Treatise on Geophysics*, v. 2.16, p. 437-491,2007.

McDonough W.F. and Sun S.-s., The composition of the Earth, *Chemical Geology*, v. 120, p. 223-253, 1995.

Merkel S., Wenk H.-R., Shu J., Shen G., Gillet P., Mao, H-k. and Hemley, R., Deformation of polycrystalline MgO at pressures of the lower mantle, *Journal of Geophysical Research*, v. 107, p. 2271, 2002.

Panning M. and Romanowicz B., A three-dimensional radially anisotropic model of shear velocity in the whole mantle, *Geophysical Journal International*, v. 167, p.361-379, 2006.

Wenk H.-R., Cottaar S., Tomé C.N., McNamara A. and Romanowicz B., Deformation in the lowermost mantle: From polycrystal plasticity to seismic anisotropy, *Earth and Planetary Science Letters*, v. 306, p.33-45, 2011.

Wenk H.-R., Lonardelli I, Merkel S, Miyagi L, Pehl J, Speziale S and Tommaseo CE, Deformation textures produced in diamond anvil experiments, analyzed in radial diffraction geometry, *Journal of Physics: Condensed Matter*, v. 18, p. S933-S947, 2006.

Wenk H.-R., Lonardelli I., Pehl J., Devine J., Prakapenka V., Shen G. and Mao H.-K., In situ observation of texture development in olivine, ringwoodite, magnesiowüestite and silicate perovskite at high pressure, *Earth and Planetary Science Letters*, v. 226, p. 507-519, 2004.

2 The Single Free Energy Surface of Amorphous $CaSiO_3$ from 0 to 44 GPa of Pressure

Zack Geballe, Sarah Arveson, Sergio Speziale and Raymond Jeanloz

Introduction

The study of high-pressure silicate melts is important for Earth Science because their material properties control the thermal, chemical and dynamic history of the earth's crust and mantle. The densities and compressibilities of high-pressure pyroxene-composition ($XY(Si,Al)_2Si_2O_6$) melts are basic properties, but even density is difficult to measure directly. Instead, experimental probes such as Raman and X-ray diffraction have been used to reveal structural changes in high-pressure melts, and molecular dynamics simulations are relied upon to estimate density *(e.g. Funamori et al.,* 2004).

To allow use of other probes of structure and elasticity, amorphous solids, which may be analogous to melts, can be studied. Once quenched to low temperature, they can be more easily probed than the refractory melts, which must be maintained at high temperatures. Yet amorphous materials do not necessarily reflect properties of the melt or even the properties of other amorphous forms of the material.

In the case of amorphous $CaSiO_3$, however, comparisons between various amorphous materials can be made. Similarity in nuclear magnetic resonance (NMR) and refractive index measurements on decompression-amorphized $CaSiO_3$ and the melt-quenched glass suggests their structures are similar: silica tetrahedra linked together in chains that are truncated by cations or linked together in clusters, evidenced by the ^{29}Si NMR spectra, as well as a complete lack of higher-coordinated silicon atoms. Yet no studies have compared compression-amorphized $CaSiO_3$ to other amorphous forms and few data sets address the reversibility of pressure or temperature cycling of amorphous $CaSiO_3$.

Method and Results

We studied amorphous $CaSiO_3$ between 0 to 44 GPa in diamond anvil cells using Brillouin spectroscopy with complementary X-ray diffraction. Two types of samples were studied: glassy $CaSiO_3$ that was quenched from its melt (*Vo-Thahn et al.*, 1996, *Kubicki et al.*, 1992) and a powder of natural wollastonite, the crystalline form of $CaSiO_3$ that is stable at ambient conditions. The density of the glass starting material was measured to be $2.92 \pm 0.02\ g/cm^3$ using a sink-float method. The powder sample was squeezed until it became transparent at ~35 GPa, at which point nearly all X-ray diffraction peaks disappeared from the image-plate detector, showing that most of the sample amorphized, consistent with *Serghiou et al.* (1993). The pressure-amorphized powder was first studied with no pressure medium (*i.e.* sample squeezed between diamonds), and then the sample was transferred to a second diamond cell and surrounded with a methanol-ethanol-water pressure medium. The glass starting material was surrounded in an argon pressure medium. Brillouin spectra were collected in 40° equal-angle

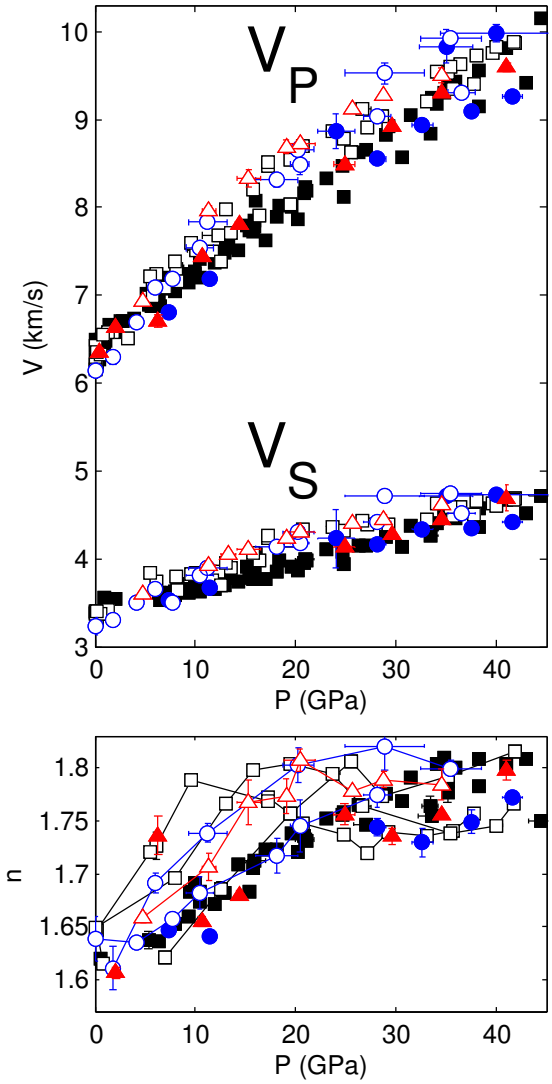

Figure 2.2.1: Longitudinal and shear wave speed (top) and index of refraction (bottom) of amorphous $CaSiO_3$ as a function of pressure during compression (solid symbols) and decompression (open symbols) between 0 and 44 GPa. Colors and shapes indicate starting material: melt-quenched $CaSiO_3$ glass (black squares), non-hydrostatically compressed powder (blue circles), and pressure-amorphized wollastonite in a pressure transmitting medium (red triangles). Error bars on individual data points are from scatter during rotations about the diamond cell axis, in the case that rotations were performed.

forward-scattering in order to measure both longitudinal and transverse sound speeds (V_P and V_S), and in 180° backscattering in order to measure the product of refractive index, n, with V_P. Pressure was measured from the fluorescence line shift of two to four rubies spheres placed near the edge of the gasket hole.

We find that the amorphous forms of $CaSiO_3$ studied here are highly reproducible under high stress conditions. Upon compression and re-compression, acoustic velocities and refractive

indices of all samples agree within the scatter of ~3% (Figure 2.2.1), suggesting that a single energy surface approximates the pressure dependence of all starting materials. Upon decompression, hysteresis is observed (up to 6% in V_P, 8% in V_S, and 5% in n), but it is small is comparison to the hysteresis of other silicate glasses. Moreover, similarly shaped hysteresis curves are observed for all pressure cycles with no systematic difference between the different samples. Finally, the velocities change nearly linearly with pressure, suggesting no kinks in the free energy surface (*i.e.* no first order phase transitions from 0 to 44 GPa). The differences that do exist between compression and decompression data suggest a structural phase transition, but it is likely to be a gradual evolution in order to explain the smoothly varying, reproducible velocity data.

Therefore, these data add evidence that amorphous $CaSiO_3$ is a highly meta-stable glass. Its reproducibility with pressure cycling and its independence of synthesis conditions are shown schematically in Figure 2.2.2. Both amorphous forms of $CaSiO_3$ studied here (melt-quenched and compression-amorphized; paths 1 and 3 in Figure 2.2.2) have indistinguishable refractive index, longitudinal wave speed and shear wave speed between 0 and 44 GPa. Melt-quenched and decompression-amorphized solids (paths 1 and 2 in Figure 2.2.2) also have the same refractive index and ^{29}Si NMR spectrum at ambient pressure and temperature (*Kanzaki et al.,* 1991*; Ringwood and Major,* 1971). Together, this implies that all three forms of amorphous $CaSiO_3$ created in a broad region of pressure-temperature space are structurally similar. And because pressure cycling causes smooth and relatively reversible changes in sound speeds, we connect the low and high pressure amorphous solids by a yellow shaded region to represent the single, smoothly varying free energy curve connecting low to high pressure amorphous $CaSiO_3$.

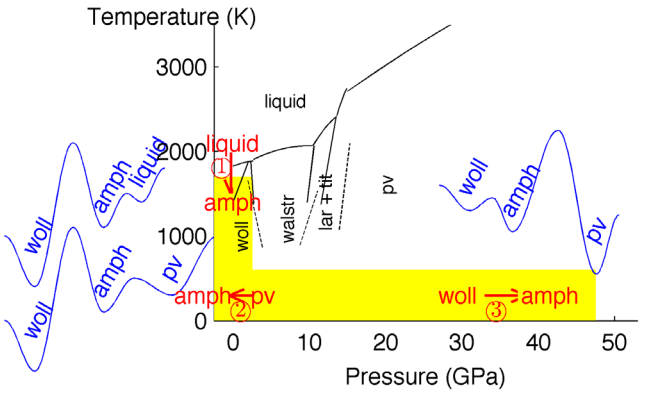

Figure 2.2.2: Pressure-temperature phase diagram of $CaSiO_3$ with schematic of potential wells to explain three observed glass transitions: (1) Melt-quenched glass formation (e.g. *Vo-Thanh et al., 1996; Kubicki et al., 1992; Ringwood and Major 1971*; and the glass used in this study), (2) amorphization by decompression of perovskite (e.g. *Ringwood and Major, 1971; Kanzaki et al., 1991)*, (3) amorphization by compression of wollastonite (*Serghiou and Hammack, 1993;* this study). Black lines mark equilibrium phase boundaries (dashed lines: *Akaogi et al., 2004*; solid curves: *Zerr et al., 1997*). Yellow marks the region in which we conclude a single type of glass is meta-stable. Red arrows mark observed locations of pressure-amorphizations.

Acknowledgements

We thank Pascal Richet, Rus Hemley and Bjorn Myssen for providing us samples of $CaSiO_3$ glass and Tim Teague for providing us with natural crystalline wollastonite.

References

Akaogi, M., et al., High-pressure transitions of diopside and wollastonite: phase equilibria and thermochemistry of $CaMgSi_2O_6$, $CaSiO_3$ and $CaSi_2O_5$-$CaTiSiO_5$ system: *Physics of the Earth and Planetary Interiors,* 143-144, p. 145-156, 2004.

Funamori, N., et al., Exploratory studies of silicate melt structure at high pressures and temperatures by in situ X-ray diffraction: *Journal of Geophysical Research*, 109, p. B03203, 2004.

Kanzaki, M., Stebbins, J. and Xue, X., Characterization of quenched high pressure phases in $CaSiO_3$ system by XRD and ^{29}Si NMR: *Geophysical Research Letters*, 18, p. 463-466, 1991,

Kubicki, J., Hemley, R. and Hofmeister, A., Raman and infrared study of pressure-induced structural changes in $MgSiO_3$, $CaMgSi_2O_6$, and $CaSiO_3$ glasses: *American Mineralogist*, 77, p. 258-269, 1992.

Ringwood, A., and Major., A., Synthesis of majorite and other high pressure garnets and perovskites: *Earth and Planetary Science Letters*, 12, p. 411-418, 1971.

Serghiou, G. and Hammack, W., Pressure-induced amorphization of wollastonite ($CaSiO_3$) at room temperature: *Journal of Chemical Physics*, 98, p. 9830-9834, 1993.

Vo-Thahn, D., Polian, A. and Richet, P., Elastic properties of silicate melts up to 2350 K from Brillouin scattering: *Geophysical Research Letters,* 23, p. 423-426, 1996.

Zerr, A., Serghiou, G. and Boehler, R., Melting of $CaSiO_3$ perovskite to 430 kbar and first in-situ measurements of lower mantle eutectic temperatures, 24, p. 909-912, 1997.

3 A Laboratory Rock-physics Study on How P-wave Properties Change with Respect to Ice Content in Saturated, Unconsolidated Saline Permafrost

Shan Dou, Seiji Nakagawa, Jonathan Ajo-Franklin, Douglas Dreger

Introduction

Saline permafrost is the subset of permafrost that contains dissolved salts in its pore-water. In contrast with its non-saline counterpart, saline permafrost freezes at lower sub-zero temperatures because of freezing-point depression of the dissolved salts. When temperatures drop below the freezing point, dissolved salts are not integrated into ice crystals and thus remain in residual pore-water, a process which prevents further freezing as increased salt concentrations lower the freezing point. Hence, saline permafrost remains only partially frozen unless the eutectic point (~−21°C for NaCl solution) is reached. Because the range of permafrost temperatures found in nature (~−15°C to 0°C) is usually higher than the eutectic point, natural saline permafrost is most likely to be unfrozen or partially frozen, which results in a wide range of possible ice content under various salinity and temperature conditions.

Dissolved salts in saline permafrost primarily originate from marine deposits and/or seawater transgressions, hence, saline permafrost is widespread in subsea and coastal areas of Arctic and Antarctica. Saline permafrost is highly sensitive to thermal disturbances and mechanically weaker than its non-saline counterpart. Hence, temperature increases under a warming climate—even for sub-zero increases—could easily cause saline permafrost to destabilize. The low bearing capacity of saline permafrost has long been the culprit for deforming and damaging a large number of cold-region infrastructure components (*Brouchkov, 2003*). Predictive models of surface deformation and structural stability in a warming climate thus require approaches for estimating and predicting the influence and distribution of saline permafrost.

Seismic methods—including surface seismic and acoustic well-log measurements—are among several available methods for detecting and delineating saline permafrost, owing to the sensitivity of seismic velocities to ground-ice content (the higher the ice content, the higher the velocities). However, even after seismic velocity profiles have been acquired, an interpretation step is necessary to infer ice content from seismic velocities. Because a broad range of ice content can be present in saline permafrost, seismic interpretations are susceptible to errors unless a robust rock-physics relationship is available. However, the mapping between velocities and ice content depends heavily on the assumptions made about ice geometry: for a given velocity value, the estimated ice content could be low when ice is assumed as a cement material to bond sediment grains together, but high when ice is assumed as a pore-filling material without contacting the sediment grains. Therefore, in order to establish an effective rock-physics relationship for saline permafrost, the validity of the plausible assumptions about ice must be examined with the aid of high-quality data that are associated with a broad range of ice content.

To cover a broad range of ground-ice content through field surveys would require unrealistically extensive sampling, further complicated by the complexity of natural permafrost systems. Thus, we prefer using laboratory data that are obtained from simpler sediments under controlled experimental conditions to gain a fundamental understanding of the rock-physics relationship. Although unconsolidated sediments constitute dominant portions of the near-surface saline permafrost, relevant laboratory studies are scarce.

In this study, we investigate how seismic properties change with respect to ice content in unconsolidated saline permafrost. We conducted laboratory ultrasonic P-wave measurements in a transmission geometry using samples consisting of water-saturated 20–30 Ottawa sand (quartz sand; grain size 600–850 μm, D_{50} ~ 720 μm) within a temperature range of 10°C to −30°C and a salinity range of 0.0–2.5 M (0–13 wt%). Due to the wide range of temperatures and salinities, the fine temporal sampling of the automated data acquisition system, as well as the dissolved salts' ability to fine-tune ice content, we obtained high-quality data that provide an unprecedented opportunity for observing how P-wave properties change with respect to ice content in saturated, unconsolidated saline permafrost.

Ultrasonic Pulse-transmission Setup and Data

A pulse-transmission configuration was set up for the ultrasonic measurements of water-saturated unconsolidated sediments upon freezing (Figure 2.3.1).

Based upon the phase diagram of aqueous NaCl solution, we convert the temperatures into the corresponding ice saturation (the volume fraction of ice in the pore space) for each set of the initial (*i.e.*, prior to freezing) pore-water salinity that was experimented with 20–30 sand. Then, we present the data and the

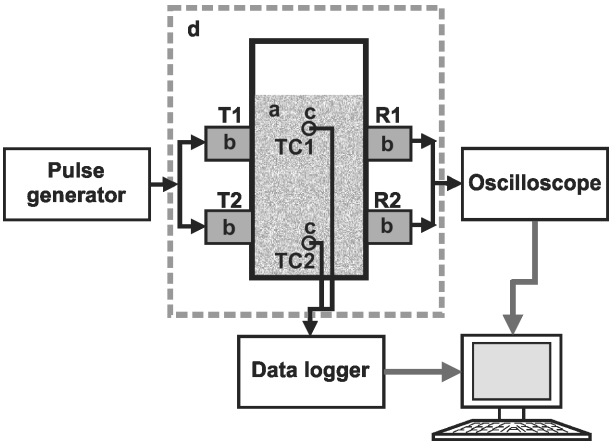

Figure 2.3.1: Column setup of pulse-transmission ultrasonic data acquisition. a) column with sand packs; b) immersion transducers; c) thermocouples (TC1 and TC2); d) bench-top freezer; T, Transmitters; R, Receivers.

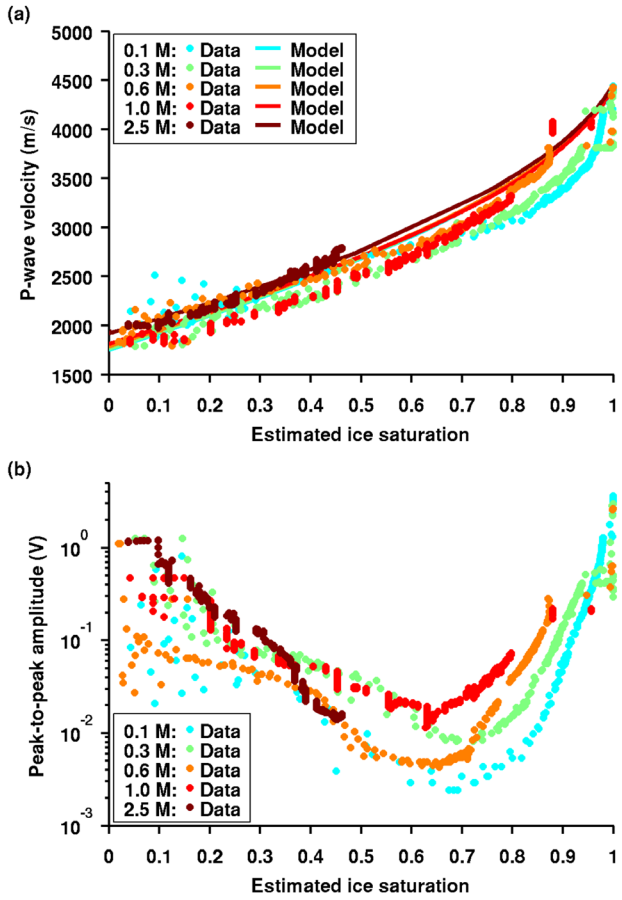

Figure 2.3.2: P-wave properties of saturated 20–30 Ottawa sand as functions of the estimated ice saturation. (a) Comparison of model-predicted and measured P-wave velocities, and (b) measured P-wave amplitudes as a function of ice saturation.

velocity modeling results as functions of ice saturation (Figure 2.3.2): Whereas P-wave velocities increase monotonically with increasing ice content, P-wave amplitudes exhibit skewed "V"-shape trends (decrease and then increase), indicating a positive correlation between attenuation and velocities at low to moderate ice saturations—an unexpected observation that sets partially frozen saline permafrost aside from most geological materials.

Effective-medium Velocity Modeling

Based upon our laboratory data, we have developed an effective-medium velocity model that assumes the coexistence of load-bearing/cement ice and non-load-bearing/non-cement ice before reaching 100% ice saturation (Figure 2.3.3). The good agreement between the model-predicted and the measured P-wave velocities suggests that ice is neither purely cementing nor purely pore-filling in saturated, unconsolidated saline permafrost.

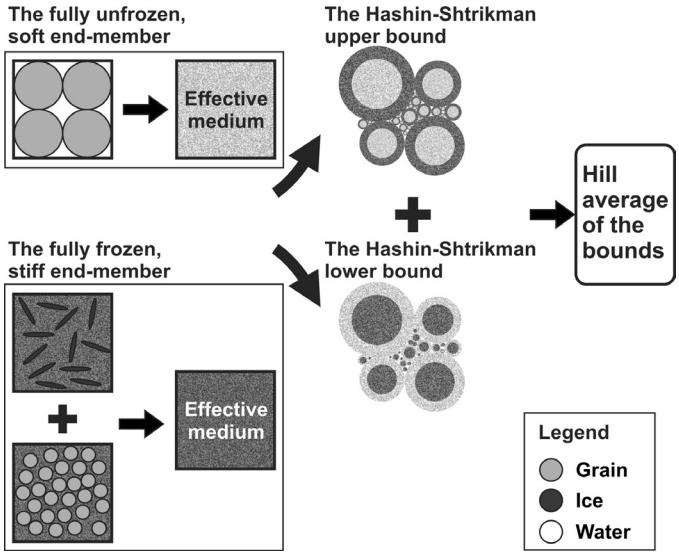

Figure 2.3.3: Intuitive interpretation of the two-end-member mixing effective-medium model.

Acknowledgements

As part of the Next-Generation Ecosystem Experiments (NGEE-Arctic) project sponsored by the Office of Biological and Environmental Research in the DOE Office of Science, this study is supported through contract DEAC0205CH11231 to Lawrence Berkeley National Laboratory and through contract DE-AC05-00OR22725 to Oak Ridge National Laboratory.

References

Brouchkov, A., Frozen saline soils of the Arctic coast: their distribution and engineering properties, *Proceedings of the 8th International Conference on Permafrost*, National Academy of Sciences, p.95-100, 2003.

4 High Temperature Miscibility of Terrestrial Materials: First Principles Calculations for the Early Earth

Sean M. Wahl, Burkhard Militzer

Introduction

Terrestrial planets are, to first order, made up of a metallic iron core and a mantle composed of silicate and oxide minerals. Chondritic meteorites show that these materials initially condensed together from the protoplanetary nebula. Numerous scenarios have been put forward to describe how these reservoirs interacted as they separated to form the core (*Rubie*, 2007). However, these typically assume the major components occur in two immiscible phases as they do at low temperatures. In the case of a hot early history of a growing planet, this assumption is not necessarily correct. At sufficiently high temperatures, entropic effects dominate and any mixture of materials will form a single, homogeneous phase. Late stage giant impacts, such as the hypothesized moon-forming impact, may have heated significant portions of the target to >10,000 K (*Canup*, 2004). It is therefore necessary to consider a high temperature mixture of the 'rocky' and metallic terrestrial components. The presence of such a mixed phase will affect the chemistry of iron-silicate differentiation on the early earth. Here we assess the stability of a mixed rock-metal phase as a mixture of Fe and 'rock' (MgO).

Simulation Methods

We performed density functional theory molecular dynamics (dft-md) simulations for phases in a model reaction between liquid iron, and solid (B1) or liquid magnesium oxide. MgO was selected for the representative rock phase because it has been experimentally determined to be the rocky component that is least soluble in iron (*Ozawa et. al*, 2008). The change in Gibbs free energy of this system per formula unit FeMgO for the model reaction was describe by

$$\Delta G_{mix} = \frac{1}{24} G_{(FeMgO)24} - \frac{1}{32}\left[G_{(MgO)32} + G_{Fe32}\right] \qquad (1.1)$$

We performed the dft simulations using the standard Vienna Ab-initio Simulation Package (VASP package) (*Kresse & Furthmüller*, 1996), but required the addition of the thermodynamic integration technique in order to determine the Gibbs free energy of the phases. This technique involves integration of the free energy over a series of systems with interactions controlled by a hybrid potential. The hybrid potential describes a mixture between the DFT potential and classical potential that has an analytic solution for the Gibbs free energy. This is currently the most accurate means for determining chemical potentials of a reaction using first principles simulations.

Shape of the Solvus

We characterized the shape of the Fe-MgO solvus by performing calculations at five additional intermediate compositions between the Fe and MgO end members. These were performed at 50 GPa for one temperature above the solvus and one below The Gibbs free energies of all simulations at intermediate conditions are consistent with a binary system with a miscibility gap. From these results we construct Fe-MgO phase diagram at 50 GPa, as shown in Figure 2.4.1. The miscibility gap is notably asymmetric, with temperatures decreasing faster towards the Fe-rich end member than the MgO-rich end. This shape is similar to the exsolution gap found experimentally determined for the Fe-FeO system at lower pressures.

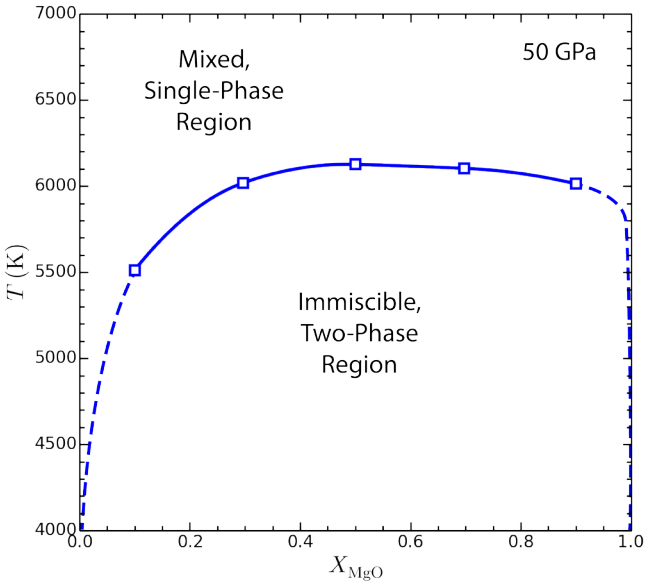

Figure 2.4.1: Solvus phase diagram of the Fe-MgO system at P = 50 GPa. The shape is consistent with X_{MgO} = 0.5 being representative composition for estimating the solvus. The asymmetry at low X_{MgO} has consequences for the solubility of Mg in the early core.

The Fe-rich side of our solvus is consistent with low solubilities found in experiments at 3000 K. From this we predict a >1% MgO saturation limit down to 4200 K, with concentrations steeply decreasing to be below consistent with low concentrations found in experiments at ~3000 K (*Ozawa et al.*, 2008). This suggests that delivery of excess, nominally insoluble, light components to the core would have been substantial for a hot early Earth. This would be followed by exsolution of a Mg-rich material at the top of the cooling core. This process has been suggested as a possible solution to the problem of the earth's core having insufficient energy to generate a magnetic field before nucleation of the inner core (*Stevenson*, 2012).

Solvus Closure Temperature

Figure 2.4.2 summarizes our results, showing all the conditions at which simulations were performed. We find the solvus closure at ambient pressure to be 4090 +/- 20 K. While there is little experimental work on this exact system, this is superficially consistent with the 'accidental' discovery of the Fe-silicate

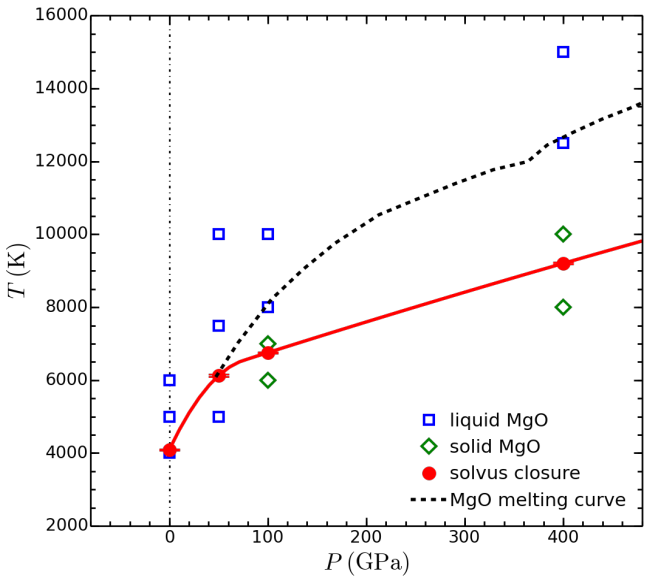

Figure 2.4.2: Pressure dependence of the solvus closure. The P-T condition of all thermodynamic integration calculations on the Fe-MgO system. Blue markers denote conditions where MgO was treated as a liquid. Green markers denote conditions where MgO was treated as a solid (B1). Red circles show the solvus closure temperature inferred from simulations as the point where a 1:1 mixture prefers a homogenous solution. The dashed, black line shows the MgO melting temperature from *Boates and Bonev,* 2013.

solvus by *Walker*, 1993. We find that the solvus temperature increases with pressure to 6020 +/-30 K at 50 GPa, but its slope decreases at lower mantle and core pressures. At core-mantle boundary pressures, the solvus closure temperature would be ~7000 K.

This pressure dependence of solvus closure determines the depth at which phases separate from the fully mixed state. Its slope with respect to pressure is less steep than the calculated isentropes of the mixed FeMgO phase. For a homogeneous, liquid layer of the planet, isentropes approximate adiabatic temperature profiles of the interior of the planet at different point in its evolution. As a result, separation begins in the exterior of the planet and proceeds inwards as the planet cools. Since iron separating in the outer portion of the planet is denser than the rocky phase, it would sink until it reached a depth where it dissolves into the mixed phase again. This may promote compositional stratification, and possibly multi-layer convection between an upper iron-poor and deeper iron-rich layer.

Acknowledgements

This work was supported by NASA and the NSF. Computational resources were provided in part by the NASA Advanced Supercomputing Division.

References

Boates, B. and Bonev, S. A., Demixing Instability in Dense Molten $MgSiO_3$ and the Phase Diagram of MgO, *Phys. Rev. Lett.* 110, 13, 135504, 2013.

Canup, R. M., 2004, Dynamics of Lunar Formation, *Annu. Rev. Astron. Astrophys.* 42, 1, 441-75, 2004.

Kresse, G. and J. Furthmuller, 1996, Efficient iterative schemes for ab initio total energy calculations using a plane-wave basis set,Phys. Rev. B-Cond. Mat.,54,16,11169-86, 1996.

Ozawa, H., Hirose, K. Mitome, M., Bando, Y., Sata, N. and Ohishi, Y., Chemical equilibrium between ferropericlase and molten iron to 134 GPa and implications for iron content at the bottom of the mantle, *Geophys. Res. Lett*., 35, 5, L05308, 2008.

Rubie, D. C., Nimmo, F., and Melosh, H. J., Formation of Earths core, *Treatise Geophys*. 9, 51-90, 2007.

Stevenson, D., How to keep a Dynamo Running in spite of High Thermal Conductivity, *AGU Fall Meet. Abstr., 2012.*

Walker, D., Norby, L. and Jones, J. H.,Superheating effects on metal-silicate partitioning of siderophile elements, *Science* 262, 5141, 1858-61, 1993.

Research Studies:
Earth Structure

5 Whole-mantle Spectral-Element Waveform Tomography: SEMUCB-WM1

Scott French and Barbara Romanowicz

Introduction

Over the past year, we have developed the first-ever model of whole-mantle radially anisotropic shear velocity obtained using the spectral element method (SEM: e.g. Capdeville et al., 2003) for waveform forward modeling. This work was motivated by the earlier success of the SEM-based "hybrid" waveform inversion approach in upper mantle and transition zone imaging (*Lekic and Romanowicz*, 2011; *French et al.*, 2013). Here, we briefly describe our efforts in achieving this result, while also presenting some details of the model, known as SEMUCB-WM1. A full discussion of model construction, as well as a detailed discussion of model structure and associated uncertainties appears in a manuscript recently submitted for publication (*French and Romanowicz*, 2014, *submitted to GJI*).

Dataset

Our inversion dataset contains fundamental and overtone mode surface-wave and body-wave waveforms. Surface-wave data are filtered at 400–60 s period, while body waves are filtered in two passbands: 300–36 s or 32 s. The 32 s filter is used after the model has converged at 36 s. In addition to modifying the passband of our body-wave dataset during the inversion, we also enlarge our datasets: initially using the same 203 events as in SEMum (*Lekic and Romanowicz*, 2011), and later adding 70 new events to improve coverage of the lower mantle. Data are processed using a waveform windowing scheme (*Li and Romanowicz*, 1996). Windows are selected based on similarity to SEM synthetics computed in the most recent model iteration. Data is reprocessed at each inversion iteration, thus allowing more data in as the model improves.

We supplement our waveform data with group-velocity dispersion maps at 25–150 s period (M. Ritzwoller, *pers. comm.* 2009). These data are used to calibrate our smooth crustal model and ensure its consistency with the underlying mantle structure (see *French et al.* 2013). Together with the mode-coupled SEM of *Capdeville et al.* (2003), the smooth crustal layer improves the time stability of the SEM. Better time stability allows larger time steps to be used, thereby reducing the overall cost of SEM simulations.

Inversion

Our inversion for whole-mantle structure proceeds in three iterations: each uses both the surface and body-wave datasets, while only the second and third iterations included the enlarged (273 event) set and only the third iteration uses the shorter 32 s body-wave filter passband. Our starting model combines SEMum2 (*French et al.*, 2013) down to 800 km with SAW24B16 (*Mégnin and Romanowicz*, 2000) below. We use the generalized least-squares formalism of *Tarantola and Valette* (1982), yielding a quickly converging Gauss-Newton scheme for optimizing the tomographic model (and thus reducing the number of SEM simulations required). We include *a priori* information in our inversion to constrain the permissible length scales of model structure (see *Lekic and Romanowicz*, 2011). By the end of the inversion, our dataset contains >447,000 waveform windows, fitting the surface-wave data nearly as well as in the earlier SEMum2 model, while showing body-wave variance reduction above 50%. The SEM simulations for our inversion, excluding sensitivity kernel and parallel linear algebra calculations, represent nearly 3M CPU hours of computation.

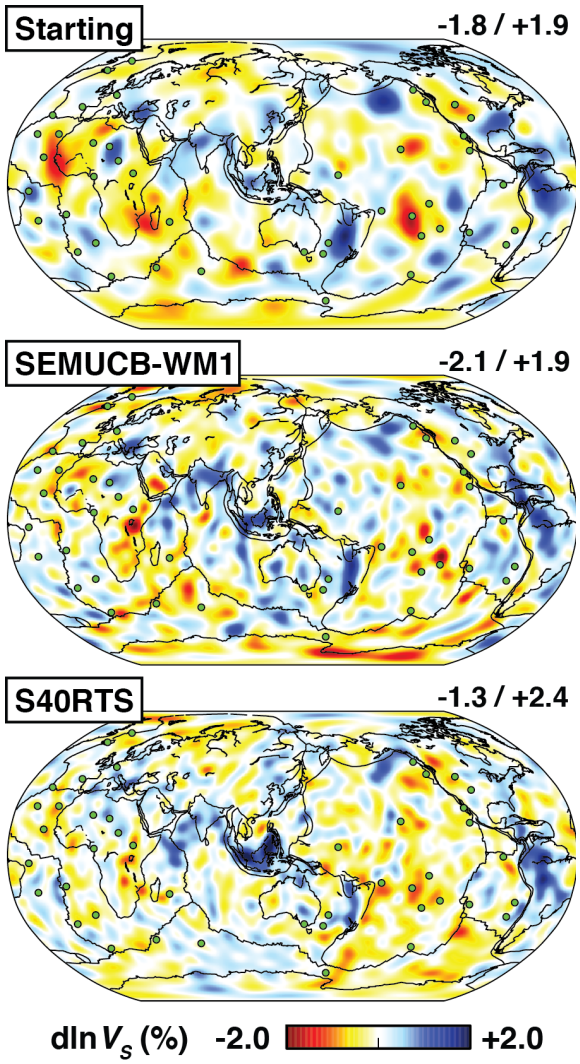

Figure 2.5.1: Comparison between starting and final-iteration models (top and middle panels, respectively) at 1000 km, as well as model S40RTS of *Ritsema et al.* (2011) (bottom panel). At this depth, the starting model is SAW24B16 of *Mégnin and Romanowicz* (2000). Inset values: maximum peak-to-peak variation in each model.

Model Structure and Discussion

As upper-mantle structure remains very close to SEMum2, we here focus on the lower mantle. In Figure 1, we show iso-

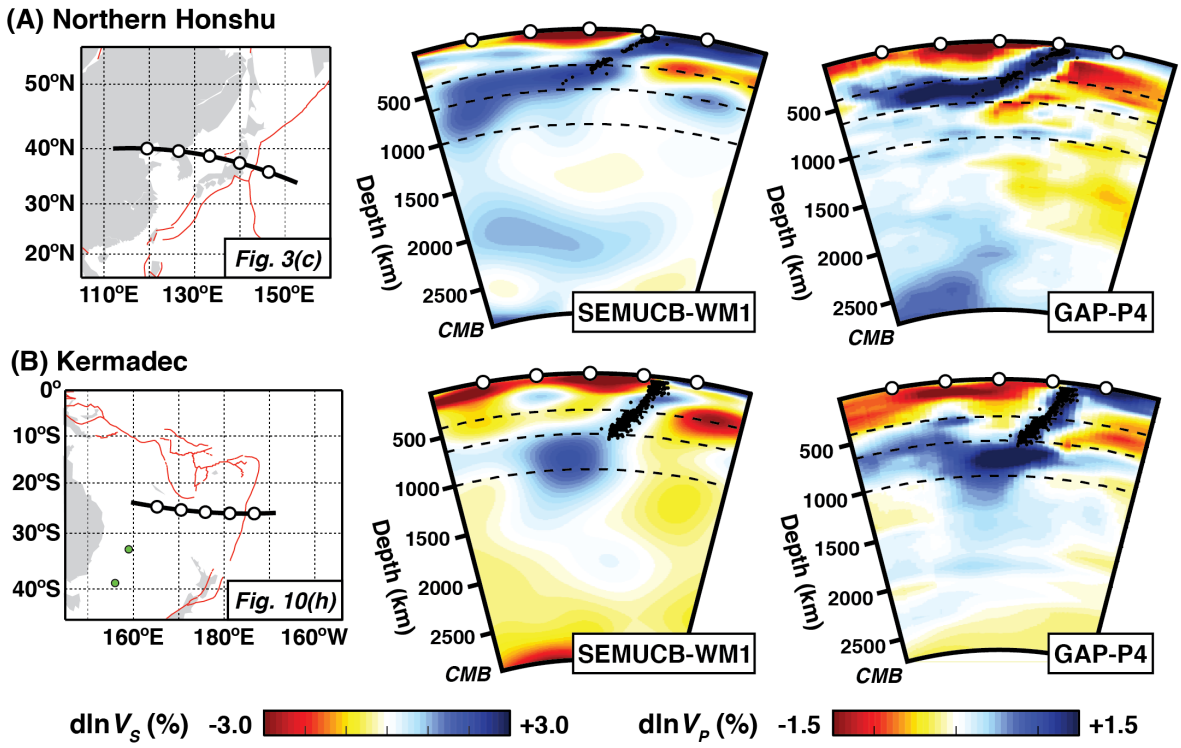

Figure 2.5.2: Whole-mantle cross-sections through subduction zones, comparing SEMUCB-WM1 V_S and V_P from GAP-P4 (*Obayashi et al.*, 2013). Map panels indicate lines of section (inset figure numbers reference the same lines of section in *Fukao and Obayashi* (2013)). Black circles on sections: deep earthquakes. Dashed lines: 410, 650, and 1000 km depth (top to bottom). Note the different V_S and V_P saturation levels.

tropic V_S variations at 1000 km depth in three models: our staring and final-iteration models, as well as S40RTS (*Ritsema et al.*, 2011). We find that structure has sharpened significantly from our starting model, including more concentrated fast anomalies, interpreted as subducted slabs, and distinct narrow slow anomalies near many major hotspots (e.g. South Pacific Superswell, Iceland). While SEMUCB-WM1 and S40RTS are broadly consistent at this depth, they clearly differ in detail; particularly in these features associated with hotspots. We will return to lower-mantle low-velocity structure in greater detail in a future publication. In Figure 2, we compare subduction-zone cross-sections through SEMUCB-WM1 V_S structure and the V_P model GAP-P4, used by *Fukao and Obayashi* (2013) to survey global slab behavior. We find excellent agreement in both the lateral distribution of high-velocity anomalies (and correlation with deep seismicity), as well as apparent slab-stagnation depth. We also see fairly good agreement in upper-mantle/transition-zone slow anomalies. These independent observations give us further confidence that the newly developed lower-mantle structure of our model is robust.

Acknowledgements

We acknowledge support from the National Science Foundation (grant EAR-0738284). SWF acknowledges support from an NSF Graduate Research Fellowship. Computations were performed at the National Energy Research Scientific Computing Center, supported by the Department of Energy Office of Science (Contract No. DE-AC02-05CH11231).

References

Capdeville, Y., Chaljub, E., Vilotte, J.-P., Montagner, J.-P., Coupling the spectral element method with a modal solution for elastic wave propagation in global earth models, *Geophys. J. Int.*, 152, 34–67, 2003.

French, S., Lekic, V., Romanowicz, B., Waveform Tomography Reveals Channeled Flow at the Base of the Oceanic Asthenosphere, *Science*, 342, 227–230, 2013.

Fukao, Y., Obayashi, M., Subducted slabs stagnant above, penetrating through, and trapped below the 660 km discontinuity, *J. Geophys. Res.*, 118(11), 5920–5938, 2013.

Lekic, V., Romanowicz, B., Inferring upper-mantle structure by full waveform tomography with the spectral element method, *Geophys. J. Int.*, 185, 799–831, 2011.

Li, X., Romanowicz, B., Global mantle shear velocity model developed using nonlinear asymptotic coupling theory, *J. Geophys. Res.*, 101, 245–22, 1996.

Mégnin, C., Romanowicz, B., The three-dimensional shear velocity structure of the mantle from the inversion of body, surface and higher-mode waveforms, *Geophys. J. Int.*, 143, 709–728, 2000.

Obayashi, M., Yoshimitsu, J., Nolet, G., Fukao, Y., Shiobara, H., Sugioka, H., Miyamachi, H., Gao, Y., Finite frequency whole mantle p wave tomography: Improvement of subducted slab images, *Geophys. Res. Lett.*, 40(21), 5652–5657, 2013.

Ritsema, J., Deuss, A., van Heijst, H., Woodhouse, J., S40RTS: a degree-40 shear-velocity model for the mantle from new Rayleigh wave dispersion, teleseismic traveltime and normal-mode splitting function measurements, *Geophys. J. Int.*, 184, 1223–1236, 2011.

Tarantola, A., Valette, B., Generalized Nonlinear Inverse Problems Solved Using the Least Squares Criterion, *Rev. Geophys.*, 20, 219–232, 1982.

6 Body Wave Tomography of the Juan de Fuca plate

William B. Hawley and Richard Allen

Introduction

The Juan de Fuca plate is a small oceanic plate that is being subducted underneath the northwestern corner of the contiguous United States. This is the only part of the country other than Alaska that contains an active subduction zone. The Cascadia Initiative (CI) is a four-year-long deployment of 70 ocean bottom seismometer (OBS) stations that covers the Juan de Fuca plate from the western side of the mid-ocean ridge that creates the plate to the Cascadia trench. This is an ideal location for a regional-scale OBS array because the plate is small enough to be covered by an array of seismometers, yet large enough to help understand large-scale oceanic plates and their relationship to the mantle below. In this contribution, we present a preliminary teleseismic P-wave velocity model of the region using the CI stations, as well as stations on shore, including those from the Transportable Array, the Berkeley Digital Seismic Network, the Cascade Chain Volcano Monitoring (run by Cascades Volcano Observatory and USGS), and the University of Washington, among others.

Noise Analysis

Seismic stations on the ocean floor provide a new and valuable scientific resource, even when used to augment the data that we have from land-based stations. The noise characteristics of the two types of stations, however, can be very different. For OBS stations, the noise is generally derived from wind and waves, both by direct forcing at longer periods and by coupling to elastic waves in the earth at shorter periods (*Webb*, 1998).

In order to filter out this noise, we analyzed the P-wave arrival signal in a number of bands, including bands that are often used in purely land based studies, and bands that have been published as being suitable for observing teleseismic body waves (*e.g., Lewis and Dorman*, 1998). Much of the intermediate frequency range—about 0.5 to 2 Hz, those frequencies that produce the best teleseismic arrivals on land-based stations—is dominated by noise in the ocean stations. In order to cross correlate the arrivals, we needed to be able to pick the arrival at each station in the same frequency band. In looking for the best band, therefore, we placed priority on obtaining data from the OBS stations, while still ensuring we obtained reliable data from the land-based stations.

With this in mind, we determined that using the relatively low-frequency and narrow passband from 0.08 to 0.11 Hz (about 9 to 12.5 s period) resulted in the clearest body wave arrivals for the OBS stations.

Methods

For this analysis, we use stations from the 7D network (the CI OBS stations), as well as some from UC Berkeley, the Transportable Array of USArray, the University of Washington, and the Cascade Chain Volcano Monitoring by USGS and CVO. We used 36 teleseismic ($30^o<\Delta<110^o$) earthquakes with magnitudes ranging from 6.8 to 7.5 for arrivals that were well above the noise, but still relatively simple. We filtered the data from 0.08 to 0.11 Hz, and picked P arrivals out of the filtered data. Arrivals that were not sufficiently above the noise were thrown out.

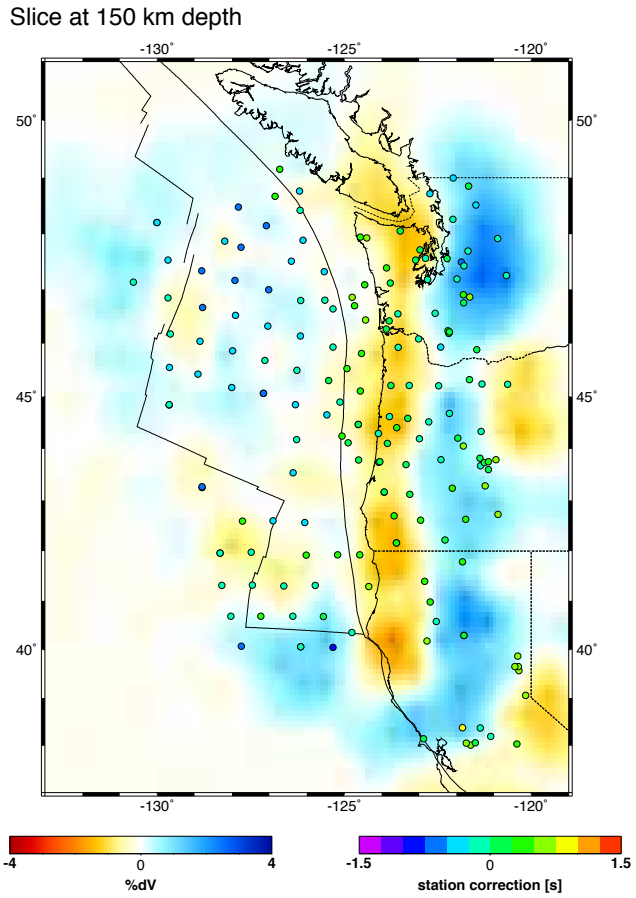

Figure 2.6.1: A horizontal slice at 150 km depth from our model. The three tectonic plates are labeled, deliniated by the thin black lines. The background color shows the relative P-wave velocity as a percent deviation from the average of the model, as shown by the left color bar. The colored dots are stations; the color represents the station correction applied to each station, as shown by the right color bar.

After applying the filter, we use the multi-channel cross correlation method (*VanDecar and Crosson*, 1990) to measure the arrival times for each of the 10,340 station-event pairs. Because the period of the waves is about 10 seconds, visually picking an arrival a fraction of a wavelength early or late would incur an error of multiple seconds. Cross correlation minimizes this error. Station-event pairs with cross-correlations coefficients that were not sufficiently high were discarded. The minimum acceptable coefficient varied for each event, but it was generally around 0.9.

We use this data to perform an inversion. For each station-event pair, we use finite-frequency kernels to determine the sensitivity matrix, and we then solve for the compressional

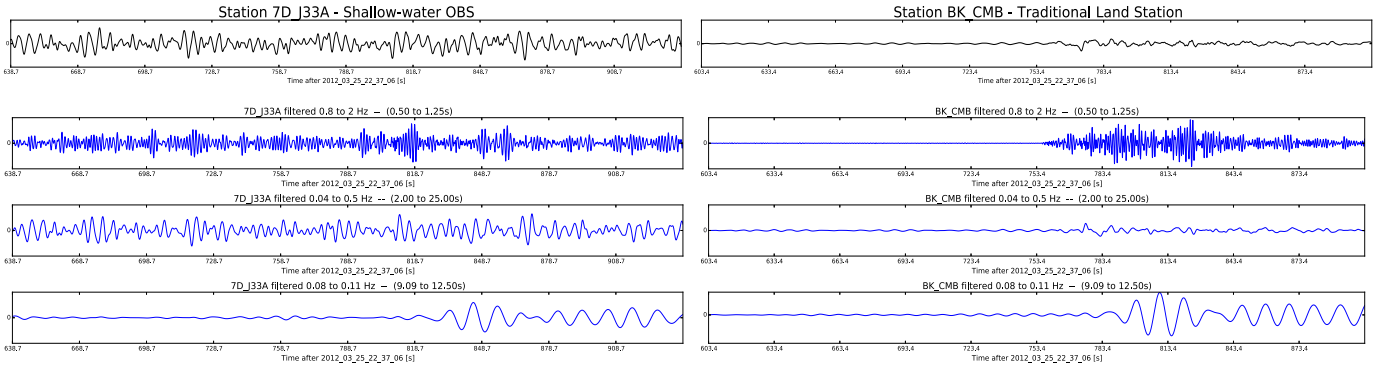

Figure 2.6.2: Seismograms from two different environments showing a recording of the same earthquake, a M7.1 in the Chilean trench. Each seismogram is centered on the IASP91-predicted P arrival. The left column is a noisy OBS station in shallow water; the right column is a traditional land-based station in the Berkeley network. The top row shows a raw seismogram, the second row shows the result of applying a bandpass filter of 0.8 to 2 Hz, the third shows the result of a 0.04 to 0.5 Hz filter, and the bottom row shows the 0.08 to 0.11 Hz filter we used in this study. Note that for the OBS, the P arrival is only visible in the final filter.

wave velocity using an iterative least-squares algorithm (*Dahlen et al.*, 2000; *Hung et al.*, 2000). Included in the process of the least-squares inversion is allowance for a station correction at each station. This is meant to account for under-sampled regions in the upper lithosphere and crust that could contribute to delays in the inversion.

Discussion

Figure 1 shows two important features: first, a high velocity region that runs from the northern to southern boundaries of our model through west-central Oregon and Washington and into California; and second, a strong low-velocity region just to the west of the high-velocity region.

The high-velocity region that spans the north-south extent of our model and appears between about 120°W and 122°W is the subducting Juan de Fuca plate. Within this slab, we see two regions of weaker high-velocity, one between 45°N and 46°N, the other between 41°N and 42°N. There is additionally a fairly strong low velocity region to the east of the more northerly of these 'gaps.'

We also see variations in strength in the low-velocity region directly to the west of the slab; note that south of about 44°N the strong regions in the slab correspond to *weak* regions in the low-velocity region and vice versa, while north of 44°N the strong regions in the slab correspond to *strong* regions in the low-velocity region and vice versa. While it is not evident in Figure 2.6.1, the low-velocity region to the west of the slab is not local to a specific depth; the region remains directly beneath the slab down to the bottom of our model. Because it is not localized, and because it is underneath as opposed to above the slab, we do not interpret this as melting oceanic lithosphere, but a process that is dynamic and particular to the area. We are investigating this feature further.

Acknowledgements

We would like to thank the Ocean Bottom Seismograph Instrument Pool (OBSIP) Management Office (OMO) staff for help in managing and understanding the OBS data. IRIS and the Cascadia Initiative Expedition Team provided the data for this work.

References

Dahlen, F.A., S.-H. Hung, and G. Nolet, Fréchet kernels for finite-frequency traveltimes–I. Theory, *Geophysical Journal International*, 141: 157-174, 2000.

Hung, S.-H., F.A. Dahlen, and G. Nolet, Fréchet kernels for finite-frequency traveltimes–II. Examples, *Geophysical Journal International*, 141: 175-203, 2000

Lewis, B.T.R. and L.M.Dorman, Recording Teleseisms on the Seafloor; an example from the Juan de Fuca Plate, *Bulletin of the Seismological Society of America*, 88, 1, p.107-116, 1998.

VanDecar, J.C. and R.S. Crosson, Determination of teleseismic relative phase arrival times using multi-channel cross-correlation and least-squares, *Bulletin of the Seismological Society of America*, 80, 1, 150-169, 1990.

Webb, S.C., Broadband Seismology and Noise under the Ocean, *Reviews of Geophysics*, 36, 1, p.105-142, 1998.

7 Further Constraints on Lateral Variations of Structure at the Base of the Pacific LLSVP Using Shear Diffracted Waves

Meng Cai and Barbara Romanowicz

Introduction

Large Low Shear Velocity Provinces (LLSVPs) are regions of reduced shear wave velocity in the lowermost ~500-1000 km of the mantle, which are located antipodally beneath the central Pacific and Africa and rooted in D". Their lateral boundaries are sharp as evidenced by the observation of complex local waveforms in seismic phases, and their density may be larger than in the surrounding structures. Ultra Low Velocity Zones (ULVZs) appear to correlate with edges of the Pacific LLSVPs as well as the locations of hotspots. The ULVZs are constrained by modeling to be several hundred kilometers in diameter and tens of kilometers in thickness. *Cottaar and Romanowicz* (2012) identified an intriguingly large ULVZ structure (called the preferred model) at the core-mantle boundary, at the northern border of the Pacific LLSVP and in the vicinity of Hawaii. Since this work was published, several recent earthquakes in different locations have illuminated this unusually large ULVZ structure and revealed quite similar waveform complexities. Owing to the strong sensitivity of the seismic data to the structure, we can model a simplified 3D ULVZ, providing further constraints on the geometry and location. The results of this study are aimed at confirming and better characterizing this unusual structure, as a first step towards searching for other possible structures of this type in the vicinity of the Pacific LLSVP.

Method and Data

Most recent seismological investigations of the lowermost mantle have used global datasets to analyze the travel time shift and amplitude variation of different seismic phases. We are using numerical forward modeling of the shear diffracted (Sdiff) phase observed at broadband stations from the USArray and other permanent networks in North America for large deep earthquakes (depth>200 km and $6<M_w<7$) in the western Pacific region at distances of 80°-130°. In this study, we used the April 17th, 2014 event (depth 208.6 km, M_w 6.9) to illustrate the affect of the ULVZ in north-central Pacific on the Sdiff waveforms.

The modeling approach is to consider the variations with azimuth and epicentral distance of Sdiff travel time residuals computed with respect to the reference 1D Preliminary Reference Earth Model (PREM, *Dziewonski and Anderson,* 1981). We also compute corresponding waveforms for 3D synthetics using the Coupled Spectral Element Method (CSEM, *Capdeville et al.,* 2003) to further interpret the waveforms of the main phase and post-cursor. This method is computationally effective for the study of D" with full 3D spectral element solution in a layer of limited thickness above the core-mantle boundary, coupled with 1D normal mode solution in the rest of the mantle and in the core.

We find that the focal mechanism provided by Centroid Moment Tensor (CMT) catalog for this event may not be optimal in that it does not accurately predict the observed amplitude ratios between the main phase and the depth phase, so modifying the focal mechanism may be necessary before we attribute amplitude variations as a function of azimuth to the structure in the D" region. This requires analyzing records from different

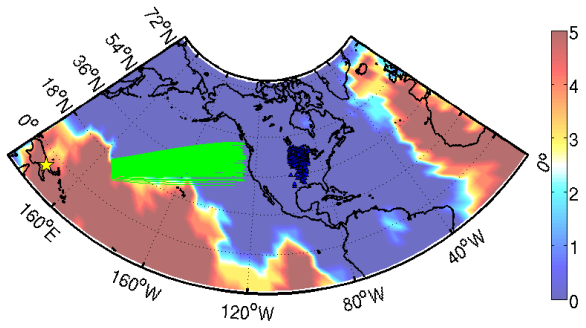

Figure 2.7.1: The location of the event is indicated by a yellow star and the stations are indicated by blue triangles, the great circle paths are indicated by green lines from entrance to exit points of a lowermost mantle layer about 300 km thick from core-mantle boundary. Background is cluster analysis result of five tomographic models (*Lekic et al.,* 2012*).* The numbers on the right indicate how many of the models agree that a particular location has shear velocity lower than average.

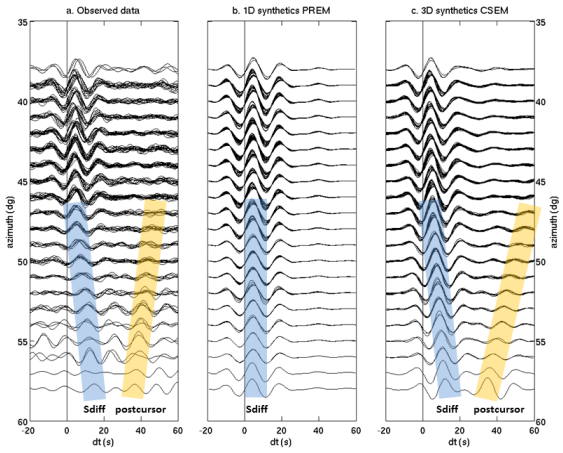

Figure 2.7.2: The comparison of tangential velocity waveforms from (a) observed data, (b) 1D PREM and (c) 3D CSEM at distances between 110° and 120°. The traces have been band-pass filtered between 10-20 s. The main Sdiff (blue) and post-cursor (yellow) are highlighted in (a) and (c) for the data and the waveforms calculated for the preferred model.

locations and azimuths using a grid search method to get the best solution.

Results

Figure 2.7.1 presents the Sdiff paths to 217 available stations from the US transportable array and permanent stations in North America that sample the border of the northern Pacific LLSVP. Based on the CMT data for this event, we computed the 1D synthetics for the PREM model in Figure 2.7.2b and 3D synthetics using CSEM for a model in which we have added a ULVZ as shown in Figure 2.7.2c. The model explains the time shift of the main Sdiff phase well (about 15 s at the most) and also the relative arrival time of the post-cursor with respect to Sdiff (about 40 s at the most), as a function of azimuth. However, the synthetics are not able to reproduce the strong amplitude reduction in the Sdiff phase at certain azimuths between 46° and 60° (Figure 2.7.3a), nor the amplitude reduction in the post-cursor phase (Figure 2.7.3b).

In Figure 2.7.3b, the post-cursor is too weak at azimuths smaller than 48°, so these measurements are only possible for larger azimuths. The synthetics reproduce the trend of increasing amplitude of the post-cursor at large azimuths, but the amplitude is slightly under-estimated compared to observed data. In Figure 2.7.3c, the travel time in 3D synthetics matches the general trend of both the Sdiff and the post-cursor phases with observed data. Some scatter in the travel time of post-cursors between 46°-48° azimuths may be due to the difficulty of measuring the peak of post-cursors, including possible cycle slips.

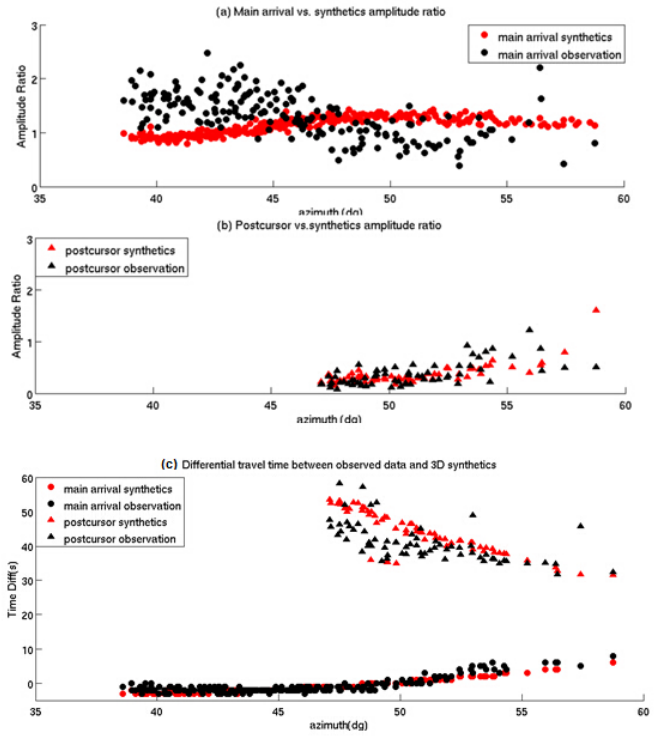

Figure 2.7.3: Amplitude ratio (a, b) and differential travel time (c) comparison between observed data (black) and 3D CSEM synthetics (red) for the main arrival Sdiff (circle) and post-cursor (triangle), measured by cross-correlation with 1D PREM synthetics filtered between 10-20 s.

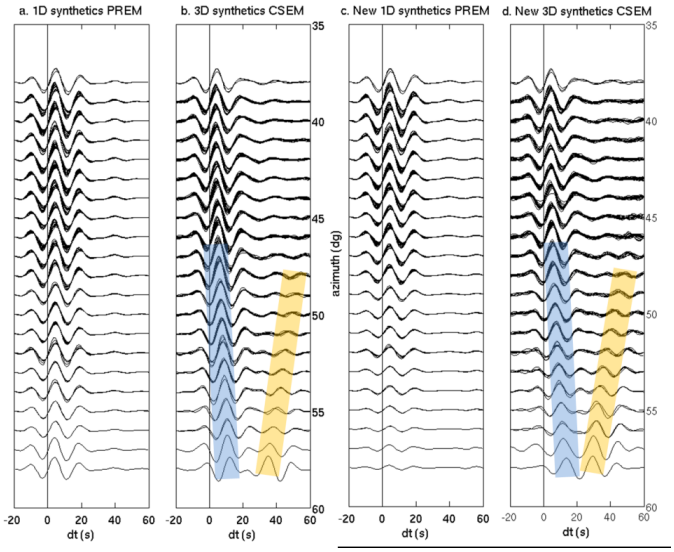

Figure 2.7.4: The comparison of tangential velocity waveforms from (a) original 1D PREM, (b) original 3D CSEM, (c) updated 1D PREM and (d) updated 3D CSEM at the distance between 110° and 120°.

On the other hand, Figure 2.7.4 indicates that after adjusting the focal mechanism, updated 3D synthetics have a clear Sdiff phase amplitude reduction as the azimuth increases, and a clear Sdiff phase amplitude reduction as the azimuth decreases, which can explain the trend in the observed data. This is also the case in 1D synthetics. However, the post-cursor synthetics at the large azimuth now have a slight time shift, which may be due to the uncertain geometry and location of the ULVZ.

Conclusions

The preferred model has been confirmed using the amplitude and travel time variations of the main Sdiff phase and time delayed post-cursor for an event not previously used in *Cottaar and Romanowicz* (2012), but there are still some features in the data that the preferred model cannot explain well. Adjusting the focal mechanism of the earthquake source can help improve the fits for the amplitude variation with azimuth, but may degrade the travel times of the post-cursors. There is potential for further constraining the shape and location of ULVZ by analyzing Sdiff phase data from new events in different locations, which can better cover the study area from all available directions.

References

Capdeville, Y., Romanowicz, B. and Toh, A., Coupling spectral elements and modes in a spectral earth: an extension to the "sandwich" case, *Geophys. J. Int.*, 154, 44-57, 2003.

Cottaar, S. and Romanowicz, B., An unusually large ULVZ at the base of the mantle near Hawaii, *Earth Planet. Sci. Lett.*, 355, 213-222, 2012.

Dziewonski, A.M. and Anderson, D.L., Preliminary reference Earth model, *Physics of the Earth and Planetary Interiors*, 25, 297-356, 1981.

Lekic, V., Cottaar, S., Dziewonski, A.M. and Romanowicz, B., Cluster analysis of global lower mantle tomography: a new class of structure and implications for chemical heterogeneity, *Earth Planet. Sci. Lett.*, 357-358, 68-77, 2012.

8 Full Waveform Seismic Tomography Using Stochastic Methods

Marco Calò, Thomas Bodin, Barbara Romanowicz

Introduction

Seismic tomography is currently evolving towards 3D earth models that satisfy full seismic waveforms at increasingly high frequencies thanks to the advent of powerful numerical methods such as the Spectral Element Method (SEM) and the drastic increase of computational resources. However, the production of such models requires handling complex misfit functions with more than one local minimum. Standard linearized inversion methods have two main drawbacks: 1) they produce models highly dependent on the starting model; 2) they do not provide a means of estimating true model uncertainties. Furthermore, current 3D SEM based models use as input either 1D, or smooth 3D models that include only the major known discontinuities (*e.g.* Moho, 400 km, 660 km) and do not consider the presence of other sharp variations of the velocities with depth such as the Mid-Lithospheric discontinuity (MLD) and the Lithosphere-Astenosphere boundary (LAB). However, these issues can be addressed with stochastic methods that can sample the space of possible solutions efficiently. Such methods are prohibitively challenging computationally in 3D, but increasingly accessible in 1D. In this project, we directly tackle the non-linearity of the inverse problem by using stochastic methods to construct a 3D starting model for SEM based tomography with a good estimate of the depths of the main layering interfaces. The procedure to carry out the starting 3D model is based on three main steps:

1. Regionalization of the study area to define provinces within which lateral variations are considered smooth;

2. Construction of 1D models of Vs and of radial anisotropy (Xi) in each province as well as the corresponding error distribution using a joint inversion approach where high frequency body waves are combined with long period Love and Rayleigh waves by updating a trans-dimensional stochastic inversion method (*Bodin et al.*, 2014).

3. Merging of the models using data-driven smoothing operators.

The patterns observed by applying the 1D stochastic inversion at several stations deployed in the North American continent represent important observations themselves for describing lithospheric structures of the region and are the subject of two papers in preparation.

Regionalization of the NA Continent

We applied k-means cluster analysis to the SEMum global tomography model (*Lekic and Romanowicz*, 2011) in the range depth 50–350 km to separate the North America region in three main provinces (Oceanic, Transition, and Cratonic zone). The mean standard deviation of the velocity profiles in each province is 0.05 km/s and the largest Euclidean norm between the average 1D profile of each region and the 1D models does not exceed 0.15 km/s. These values suggest that each macro region encloses 1D profiles that are very similar in the depth range considered and that a separation of North America in three areas is the minimum order of the cluster analysis that has to be applied to obtain a regional scale separation of the continent.

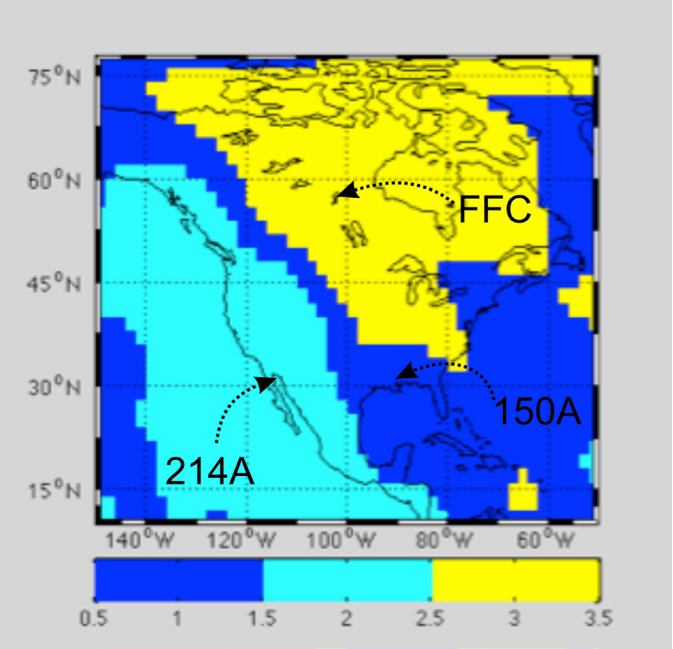

Figure 2.8.1: Separation of the North America continent in three macro-regions using the k-means cluster analysis technique. Each region is marked by a similar Vs profile in the range depth 50–350 km.

Construction of the 1D models

We calculated 1D Vs and radial anisotropy (Xi) profiles and posterior noise estimation at 24 stations deployed in the NA continent using an updated version of the trans-dimensional Markov-chain algorithm (*Bodin et al.*, 2014). In this version we jointly invert three datasets:

1. Rayleigh and Love phase velocity profiles from 25 s to 250 s, extracted from the global model of *Ekstrom et al.*, (2011).

2. Rayleigh and Love group velocity profiles from 16 s to 150 s, extracted from the global model of *Shapiro et al.*, (2002).

3. Averaged seismograms for calculating receiver functions using the cross-convolution method (*Bodin et al.*, 2014).

Synthetic tests reproducing the real data conditions show that both data and inversion methods are suitable to properly estimate posterior errors, absolute velocity values, and sharp discontinuities down to 300 km.

Figure 2.8.2 reports two examples of these tests, one us-

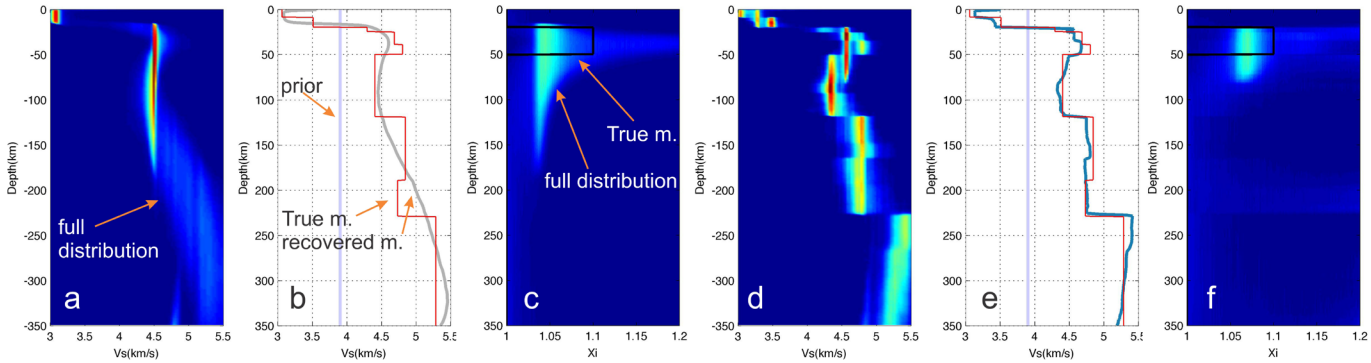

Figure 2.8.2: a,b,c) Test using group and phase velocities of Rayleigh and Love waves calculated in the period range of 16–250 s on a 1D Vs model with a radial anisotropic layer. a) posterior distribution of the Vs model, b) True Vs model, initial distribution of the prior, and recovered model, c) anisotropic layer (in black) and posterior distribution. d,e,f) Test using body wave, and group and phase velocities of Rayleigh and Love waves calculated on a 1D Vs model with a radial anisotropic layer. d) posterior distribution of the Vs model, e) True Vs model, initial distribution of the prior, and recovered model, f) anisotropic layer (in black) and posterior distribution.

ing only the surface wave data (Figure 2.8.2a,b,c) and another one using the complete dataset (Figure 2.8.2d,e,f). With these tests we show that the contribution of the surface waves allows us to constrain the absolute velocity values in depth even when we impose a width centered on a prior model far from the true model used to calculate the dispersion curves. However, a good reconstruction of the discontinuities is obtained only when adding information provided by the body waves (Figure 2.8.2d,e,f). These results show that both data and inversion methods are suitable to properly estimate posterior errors, absolute velocity values, and sharp discontinuities down to 300–350 km. Figure 2.8.3 reports an example of three 1D Vs distributions obtained for three stations (one in each macro-region). The 1D profiles show the presence of several discontinuities at different depths both in the crust and in the upper mantle.

Construction of the 3D Starting Model

The set of 1D radially anisotropic profiles allowed us to construct a 3D starting model for the North American lithosphere. The 1D models have been regrouped in families following the separations in macro-regions carried out with the cluster analysis. For each subregion, the 1D models have been averaged using a weighting function based on the posterior error distributions associated with each profile. Finally we connected the 1D profiles laterally using stochastic smoothing operators, to generate the 3D reference model. We are currently considering different strategies for adjusting the smoothing operators by simulating wave propagation through this model using a regional spectral element code (RegSEM, *Cupillard et al.*, 2012) and confronting the predictions to a set of observed waveforms, summed over a collection of events.

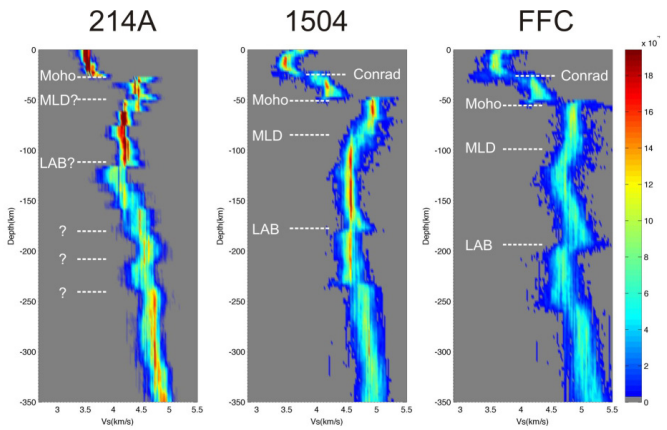

Figure 2.8.3: Examples of 1D Vs profiles calculated at three stations using the experimental data. Each station is located in a macro-region in which the NA continent has been divided (Figure 2.8.1).

Acknowledgements.

This project is funded by the "UC Lab-fee" collaboration program (UCOP grant 12-LR-236345) and is in collaboration with M. Maceira and C. Larmat at Los Alamos National Laboratory.

References

Bodin T., H Yuan, B Romanowicz, Inversion of receiver functions without deconvolution—application to the Indian craton, *Geophys. J. Int*. doi:10.1093/gji/ggt431, 2014.

Cupillard, P., Delavaud, E., Burgos, G., Festa, G., Vilotte, J.-P., Capdeville, Y. and Montagner, J.-P., RegSEM: a versatile code based on the spectral element method to compute seismic wave propagation at the regional scale, *Geophys. J. Int*, 188: 1203–1220. doi: 10.1111/j.1365-246X.2011.05311.x, 2012.

Ekström, G., A global model of Love and Rayleigh surface wave dispersion and anisotropy, 25–250 s, *Geophys. J. Int*, 187: 1668–1686. doi: 10.1111/j.1365-246X.2011.05225.x, 2011.

Lekic, V. and B. Romanowicz, Inferring upper-mantle structure by full waveform tomography with the spectral element method, *Geophys. J. Int*. v.185, no.2, p.799-831, 2011.

Shapiro, N.M. and M.H. Ritzwoller, Monte-Carlo inversion for a global shear velocity model of the crust and upper mantle, *Geophys. J. Int*, v.151, no. 1, p.88-105, 2002.

9 3D Kirchoff Prestack Depth Migration of Receiver Function

Cheng Cheng, Thomas Bodin, Richard Allen

Introduction

Time domain P receiver function, as a source removing and receiver side isolating technique, has been widely used to study the earth's interior structure in the past decade in global seismology imaging. After the deconvolution of large seismic array data, it characterizes the receiver side P-to-S conversions present within the coda of teleseismic P essentially. In order to extract the tectonic information out of this travel time ensemble, many methods have been introduced to post process the receiver function data. For example, the least-squares optimization and Mote Carlo inversion as in 1-D inversion, joint inversion with surface wave, common conversion point (CCP) stacking. Among all these methods, CCP and the later post-stack depth mapping is widely used for determining the geographic depth of the earth discontinuity. The basic idea for CCP depth mapping is that it implements the ray tracing and moveout correction for the incoming teleseismic plane wave based on a 1D earth reference model and it assumes a flat layer. This works well in mapping the reflectivity of relatively flat discontinuities, such as the Moho depth, the LAB depth etc., but it encounters difficulty when there are large heterogeneities and dipping layers, such as the subduction plate in the upper mantle. The uncertainty goes to both the CCP procedure and the later migration procedure, which can be as large as 20% in the 35 degree case (*Rondenay,* 2009). Here we introduce our solution in this complicated case: a 3D Kirchoff pre-stack depth migration method, with the application to the P receiver function. By implementing our method, both the real earth's 3D heterogeneity and the dipping interface can be accounted for. Also, this method is significant for its reduced computation time compared with the common pre-stack migration methods.

Method

Without doing the flat layer assumption and 1D moveout correction, we do the 3D ray tracing accounting for the 3D heterogeneity of the earth. It is done in the initial 3D model using the Fast Marching Method (FMM). FMM is a numerical method for solving boundary value problems for the travel time Eikonal equation. Typically, the ray tracing problems transfer to solve the evolution of a closed curve as a function of time T with speed F(x) in the normal direction at a point x on the curve using an up-wind finite difference solver. Compared with the traditional shooting method, this curve tracing tool is much faster and more stable, which is fundamental for our migration scheme. Also, our ray tracing is done for each of the three components of P receiver functions, which are P wave from the source to the model grid, P wave from the source to the receiver and converted S wave from the model grid to the receiver. Once the FMM ray tracing procedure is finished, travel times for all the source-grid-receiver pairs have been restored in the three matrices respectively using the Kirchoff migration in the next step.

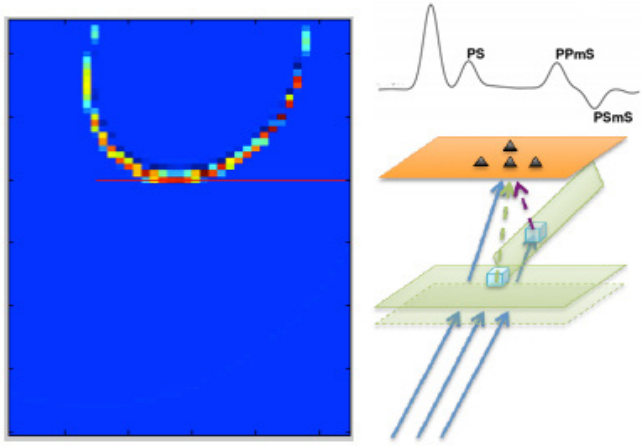

Figure 2.9.1: A diagram showing the principle of the receiver function Kirchoff migration method. The left panel is the result after one migration, the red line is the real position of the discontinuity, the semicircle is the waveform position of the PS receiver function spike after the migration procedure.

Figure 2.9.1 illustrates how Kirchoff migration works in our receiver function case. In the left image panel, the red line indicates the real position of the discontinuity. The semicircle is the migrated results in a 3D velocity model. This result is also called the impulse response of a process and is especially useful since a seismic section can be considered to consist of a series of spikes—the migrated reflectors will occur where the semicircles constructively interfere. Where the amplitude of the spikes on the input time section are distributed along a semicircle on the output migrated depth section is what is called the Kirchoff migration. Destructive interference will cancel out noise. Finally the discontinuity, which is real, comes out after the summation of the amplitudes along the semicircle and placing the summed amplitude at the apex. This form of migration formed the basis of the algorithms and is called diffraction summation, diffraction stack or more generally Kirchoff migration.

Another important process in our prestack migration scheme is the application of two weighting factors. One of which is for the factor of that we only use the radial component of P receiver function and another weighting factor serves for eliminating the off-great-circle energy.

Synthetic testing results

Figure 2.9.2 shows some preliminary synthetic results of our receiver function depth mapping using the prestack Kirchoff migration method, and is also compared with CCP depth mapping results. The first column shows the results of a flat layer. We can see that in this case both methods perform well in imaging the 0 degree discontinuity. Also we notice that even in the 0 degree case, the prestack Kirchoff migration doesn't have the multiples because the multiple energy stacked unconstruc-

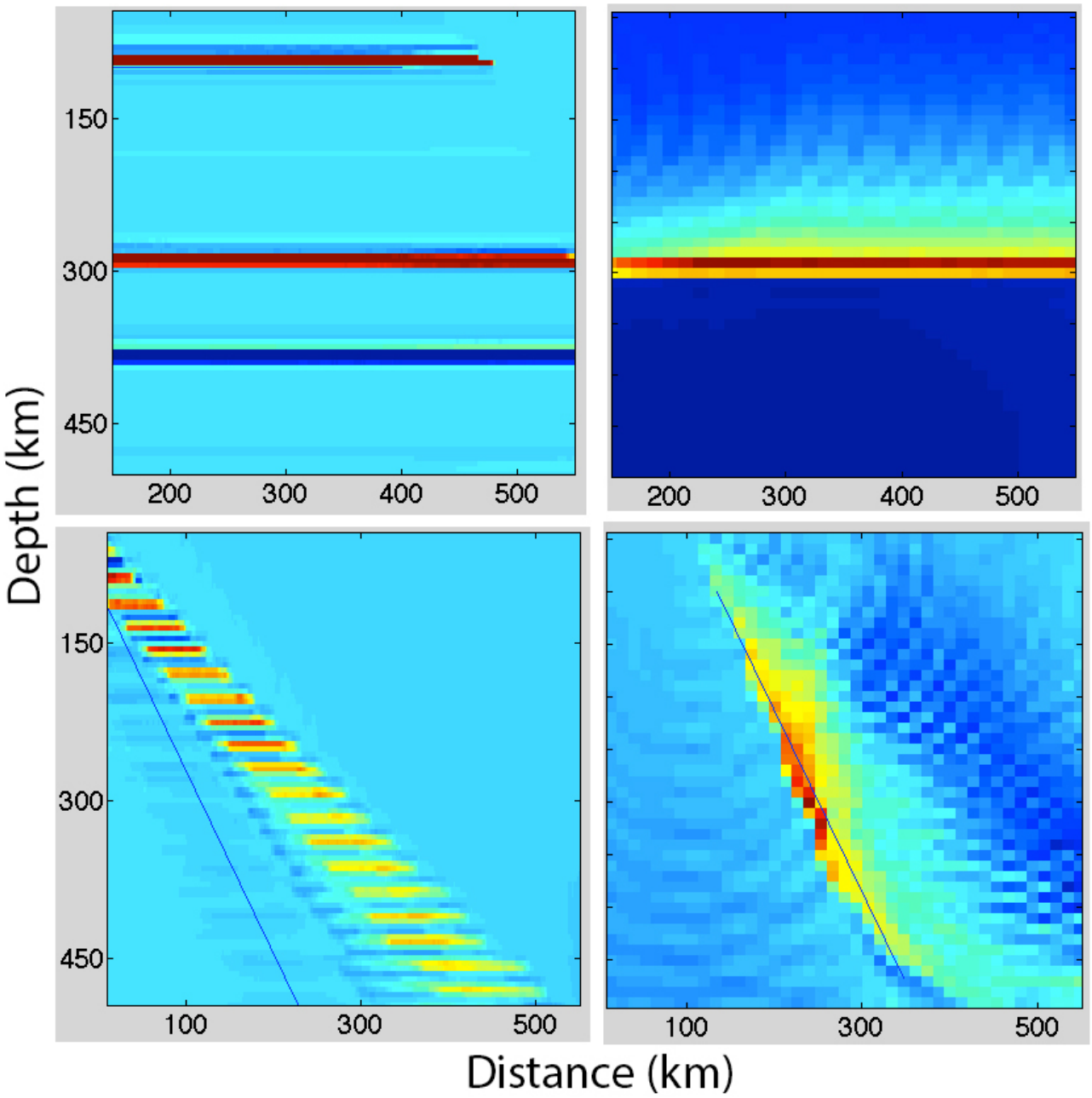

Figure 2.9.2: Comparison between the CCP depth mapping and 3D prestack Kirchoff migration of receiver function. Images in the left column are generated by CCP and the ones in the right are generated by prestack. The discontinuity in top two images are at 30 km with a 0 degree dipping layer and the one in the bottom two images has a 60 degree dipping layer.

tively and has been canceled out. The second column shows the 60 degree dipping layer case, the 3D Kirchoff migration performs much better in imaging the position and the dipping angle. The CCP depth mapping has underestimated the dipping angle, also the discontinuity is displayed as a wide band, which is not true. For comparison, the 3D FMM Kirchoff prestack migration has imaged the dipping layer at the right 60 degree angle and the right position.

In conclusion, from the preliminary testing results, our 3D prestack Kirchoff migration of receiver functions has accounted for the 3D heterogeneity of the earth model and doesn't make the 1D flat layer assumption. It has good performance in imaging big angle dipping layers and has potential applications for subduction zone imaging.

References

Rondenay, S., Upper mantle imaging with array recordings of converted and scattered teleseismic waves, *Surv. Geophys.*, 30, 377-405, 2009.

10 Joint Inversion of Receiver Functions and SKS Data: An Application to the Canadian Craton

Julie Leiva, Thomas Bodin, Barbara Romanowicz

Introduction

In order to improve layered structure models of the upper mantle beneath individual seismic stations, a new method involving a two step joint inversion of core refracted shear wave (SKS) splitting and receiver function (RF) data is currently being explored. This combination of seismic data results in a more robust structure model of the Canadian craton, and produces a probabilistic shear velocity (Vs) model acquired from RF data that incorporates azimuthal anisotropy from SKS splitting measurements. Our main focus involves resolving structure to a depth of up to 350 km beneath each seismic station, with an emphasis on layering around the lithosphere-asthenosphere boundary (LAB) and within the lithosphere itself. Knowledge of the structure around the LAB in cratonic regions will help improve the understanding of the formation of cratons and continents.

Methodology

Our inversion process utilizes a transdimensional Bayesian method that incorporates a Markov Chain Monte Carlo (MCMC) scheme to create probabilistic models, where the degree of layering, anisotropic strength and anisotropic direction are treated as unknowns.

Initially, our methodology involved a joint inversion of RF, surface wave dispersion (SWD) and SKS data that produced models of shear velocity and anisotropic parameters (strength and fast axis direction) in a single step. However, this proved to be a computationally expensive technique; the computation time was heavily improved by separating the process into two separate steps where the Vs model was first obtained by inverting RF and SWD data, and then performing a subsequent inversion for anisotropy. The latter step uses the acquired Vs model as a heavily constrained reference model, effectively limiting the second part of the inversion to solve for anisotropic parameters.

A joint inversion of RF, SWD and SKS data has proven to be advantageous; by combining different sets of data that are sensitive to sharp changes in shear velocity and anisotropy, we are able resolve finer structure with depth and distinguish both isotropic and anisotropic boundaries. Receiver functions are used to detect interfaces where seismic conversions occur (Ps and Sp), and thus expose sharp velocity changes which are necessary in constructing Vs models. SKS splitting data account for azimuthal anisotropic effects integrated over the mantle on the receiver side. Seismic anisotropy in the upper mantle is a product of past and present tectonic and mantle processes and their resultant deformation, and thus provides additional structural information. However, since SKS data relies on integration over the entire upper mantle, depth resolution for SKS data is poor. SWD data are included to improve resolution in the upper 250 km, where the LAB and the focus of our research are contained.

Results and Future Work

The full two step process has been applied to synthetic data, and the full joint inversion was able to be applied in a single step due to the relatively low computational cost. The final results of Vs, strength of anisotropy, and fast axis direction by layer are shown in Figure 2.10.1. This inversion combined three Ps RF traces and seven SKS traces, as well as SWD with periods of up to 250s. The true structural model contains five isotropic and two anisotropic layers, with anisotropic strength equal to 4% and 6%, and the fast axis direction 45° and 60°, respectively. Figure 2.10.1 shows well resolved layering, shear velocities, and anisotropic parameters.

The first step of the inversion process has been applied to the permanent seismic station YKW3 from the Canadian National Seismograph Network (CN). YKW3 is located in Yellowknife, Northwest Territories and at the northern edge of the craton and provides archived seismic data through Incorporated Research Institutions of Seismology (IRIS) from as early as 1994. Results from the first step of the inversion process are shown in Figure 2.10.2, where RF and SWD data were inverted to find the Vs model. In this case, one Ps RF trace and nine SKS traces were used, as well as SWD with periods of up to 150 s. The resultant Vs model is currently being modified to use as a reference model in the second step of the joint inversion for real data.

Future work involves finishing the second part of the inversion for data from YKW3. Steps will be taken to improve computation time for real data and to further enhance our methods prior to applying this technique to other CN stations within the Canadian craton. Subsequent work can then be done in other cratonic regions across the world in order to better understand craton and continent formation on a global scale.

Acknowledgements

This work is supported by the Lab fees Research Program, grant number 12-LR-236345.

References

Bodin, T., Sambridge, M., Tkalčić, H., Arroucau, P., Gallagher, K., and N. Rawlinson, Transdimensional inversion of receiver functions and surface wave dispersion, *J. Geophys. Res,* 117, B02301, 2012.

Bodin, T., Yuan, H., and B. Romanowicz, Inversion of Receiver Functions without Deconvolution, *Geophys. J. Int., 196,* 1025-1033, 2014.

Romanowicz, B., and H. Yuan, On the interpretation of SKS splitting measurements in the presence of several layers of anisotropy, *Geophys. J. Int., 188,* 3, 1129-1140, 2012.

Yuan, H. and B. Romanowicz, Lithospheric layering in the North American Craton, *Nature, 466,* 7310, 1063-1068, 2010.

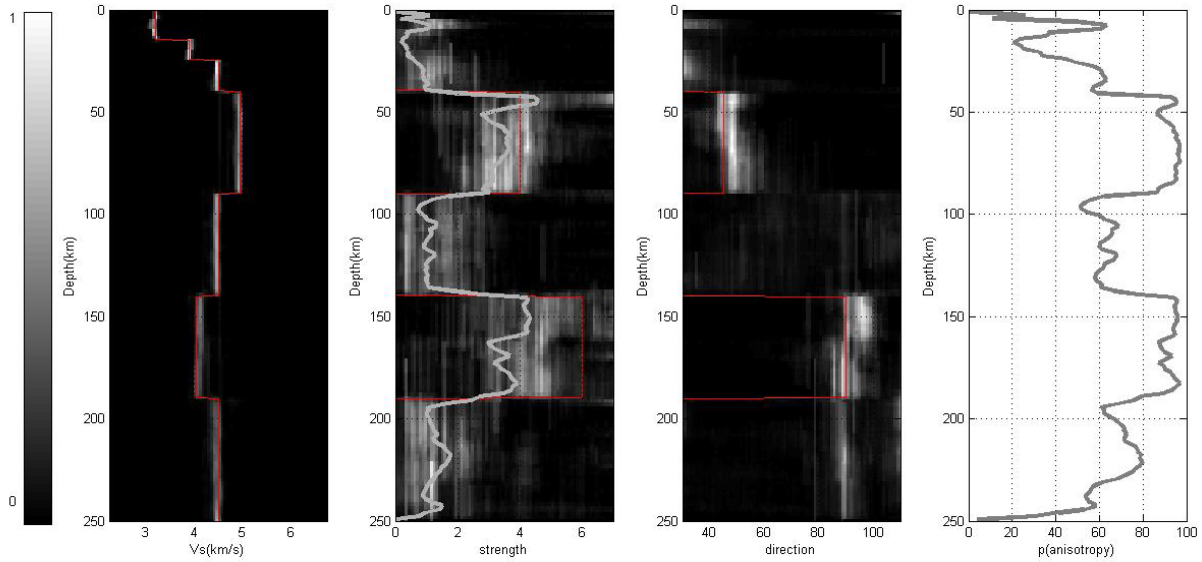

Figure 2.10.1: Results of synthetic data for the full joint inversion, where red lines indicate the true models. From left to right: a) a probabilistic solution for a shear velocity structure model down to 250 km; b) strength of anistropy with depth, where the white line indicates the mean of the data; c) fast axis direction with depth; d) the probability of anisotropy within each layer. Note that the Vs model was allowed to be inverted for in this step, due to the relatively low computational cost.

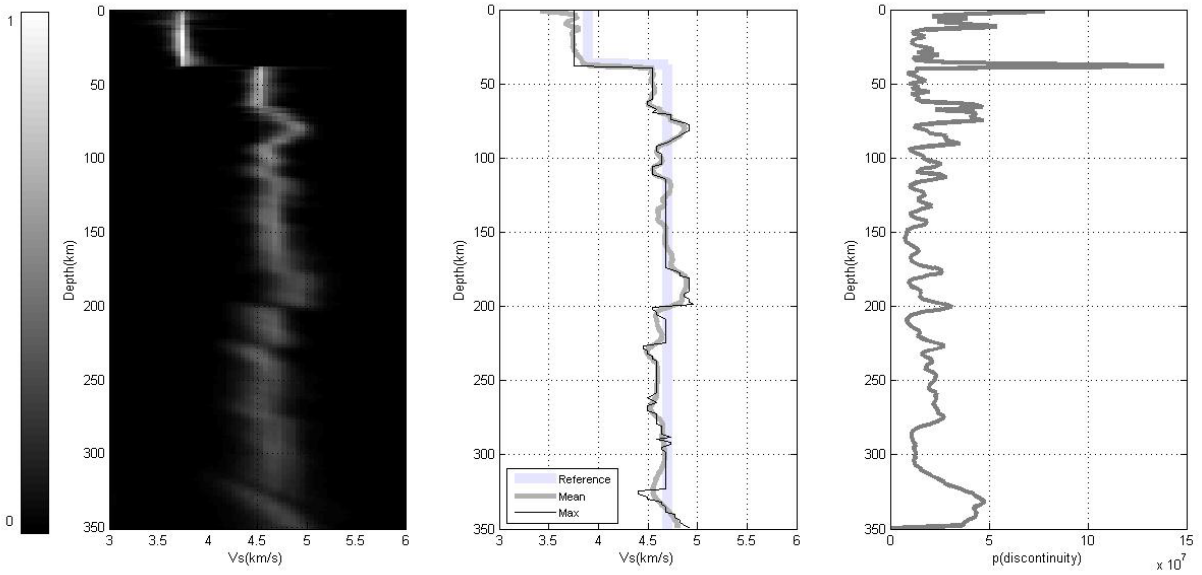

Figure 2.10.2: Results from the first step of the two step process for real data from station YKW3. From left to right: a) a probabilistic solution of the shear velocity structure model down to 350 km beneath the station, where white coloration indicates higher probability; b) a comparison of the single layer reference model to the average and maximum models; and c) the probability of the existence of a discontinuity.

11 High Resolution Upper Mantle Discontinuity Images Across the Pacific Ocean from *SS* Precursors Using the Local Slant Stack Filters

Zhao Zheng, Sergi Ventosa, Barbara Romanowicz

Introduction

The upper mantle discontinuities (primarily the 410 and the 660) place important constraints on the temperature, composition and dynamics of the earth's mantle. To image these discontinuities, one effective data type is the *SS* precursors (*Shearer*, 1991), which are shear waves reflected off the bottom of the discontinuities (Figure 2.11.1). A major advantage of the *SS* precursors, compared to other data types such as receiver functions or triplications, is that they provide coverage for the vast oceanic areas where few seismic deployments are available.

In recent years, with the improvement in the resolution of global mantle tomography (e.g. *French et al.*, 2013), there has been an increasing demand for higher resolution images of mantle discontinuities as well, in order to examine possible correlations between the two. However, several challenges have limited the spatial resolution of the discontinuity images retrieved from the *SS* precursors. First of all, the precursors are weak in amplitude (typically 5-10% of the *SS* main phase), often at or below noise level. Stacking is therefore necessary. In the past, common-midpoint (CMP) stacking over large geographic bins (radius of 10° or 5°) has been common (for a review, see *Deuss*, 2009), which limits the resolution. Secondly, *SS* precursors suffer from interference from other phases, such as the postcursors to S_{diff} (or *S* at shorter distances) and the precursors to *ScSScS*. To circumvent this issue, several past studies have limited the epicentral distance of data selection to the "safe ranges", for example, 95-115° and 140-145°, although theoretically *SS* precursors exist over the entire range of 80-160°. This has reduced the amount of available data by a significant fraction and may have led to loss of resolution.

Recent deployment of the dense US Transportable Array (TA) has provided unprecedented opportunities to achieve higher resolution for *SS* precursor studies. To overcome the above-mentioned limitations, here we employ a new tool called the Local Slant-Stack Filters (LSSF), which seeks to maximize

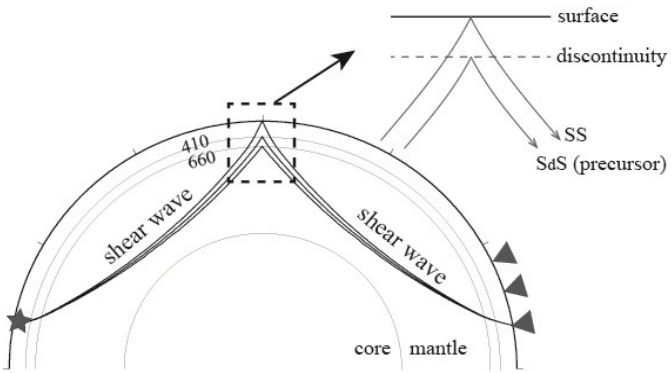

Figure 2.11.1: The ray paths of SS and its precursors. The SS precursors are reflected shear waves off the bottom side of the discontinuities (e.g. the 410 and the 660) in the Earth's upper mantle.

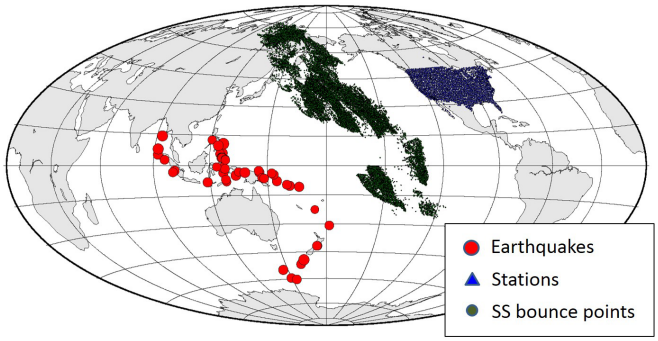

Figure 2.11.2: A map showing the *SS* precursor dataset used in this study.

spatial resolution by exploiting the advantage of a dense array. We present images of the 410 and 660 topography for a vast area across the Pacific Ocean, and compare them to a recent high resolution global upper mantle shear wave tomography model, *SEMum2* (*French et al.*, 2013).

Data and Method

We collect a dataset of *SS* precursors from 47 high quality events in the southwestern rim of the Pacific Ocean recorded by the TA between 01/2004 and 12/2013, with the following criteria: $6.0 \le M_w \le 7.8$, depth ≤ 75 km, $80° \le \Delta \le 160°$, which are consistent with previous *SS* precursor studies. The *SS* bounce points sampling area is shown in Figure 2.11.2. We look at the transverse component displacement seismograms filtered in 15–75 s, and apply various quality control procedures.

We then apply the LSSF filters to clean up these *SS* precursor record sections. Briefly, the LSSF sweeps across time and space in a record section, and conducts a slowness decomposition (slant stacking) in the vicinity of each point; then in the slowness domain, filters are designed to extract signals with a target slowness (or slowness range) and remove other signals with undesired slownesses as well as random noise. Readers are referred to *Ventosa et al.* (2012), *Zheng et al.* (2013) and *Zheng* (2014) for details. After the record sections are cleaned up, differential travel times between a precursor and the *SS* main phase are measured from each single trace, and then converted to the discontinuity depth at that bounce point. All the depth measurements are then combined to produce a map of discontinuity topography for the entire study region.

Results

Figure 2.11.3 shows a map of the 410 discontinuity depth. Overall the 410 does not show large topography. Several small-scale warm anomalies are seen in the central and south Pacific (labeled *A*, *B* and *C* in Figure 2.11.3a), with variable size and strength. Interestingly, the locations of these anomalies coin-

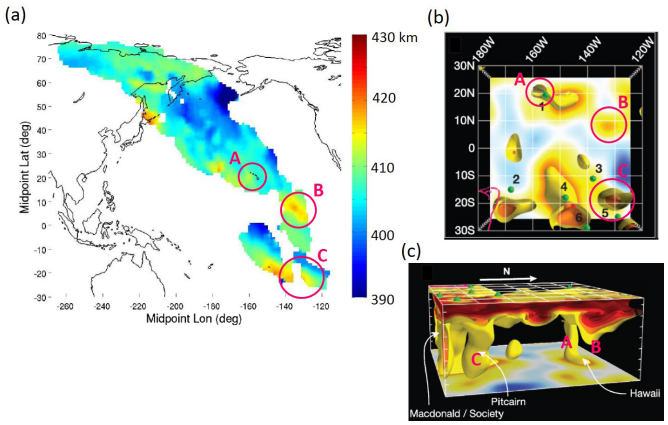

Figure 2.11.3: (a) A map of the 410 discontinuity topography for the study region. Warm colors represent longer *SS*-$S_{410}S$ differential travel time, or an apparently deeper 410, suggesting a warm anomaly if explained by temperature effect alone on olivine phase transformation. Cold colors respresent the contrary. (b) Top view and (c) side view of the tomography model *SEMum2* (*French et al.*, 2013). Low shear velocity anomalies (V_s reduction >2%) are shown in yellow.

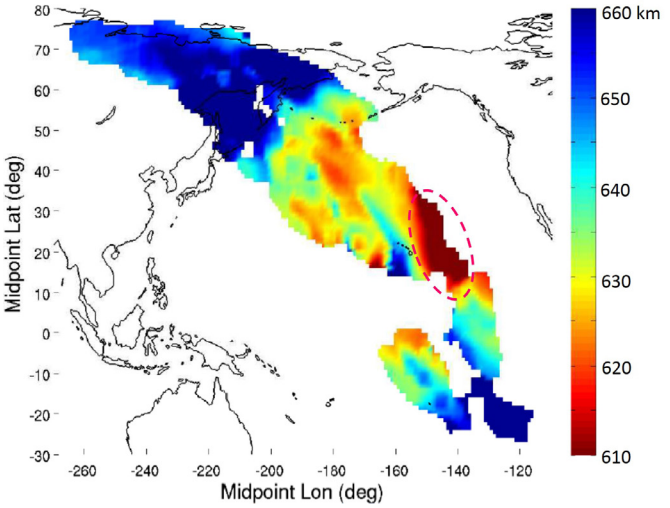

Figure 2.11.4: A map of the 660 discontinuity topography for the study region. The dashed oval outlines an anomalous area east of Hawaii, which shows significantly shorter *SS*-$S_{660}S$ differential travel times.

cide with a few low velocity columns penetrating the 410 discontinuity revealed by the tomography model *SEMum2* (Figure 2.11.3b and c). These low velocity columns can be explained as uprising hot mantle materials, which would have a "warm" signature on the 410 topography. It is remarkable that not only the locations, but also the horizontal extent and the magnitude of these three anomalies are in good agreement between the two maps.

Figure 2.11.4 shows the 660 discontinuity topography. Overall the 660 has larger topography than the 410. It is depressed in the subduction zones (colder) at the northwestern rim of the Pacific and uplifted in the oceanic regions (warmer), as previously observed. One striking feature is an area of extremely warm color to the east of Hawaii. This area is sampled by three events in the dataset, and they all give consistent results. Cross sections of the whole mantle tomography model *SEM_UCBwm* (*French* and *Romanowicz*, 2014) plotted along and perpendicular to the *SS* ray path (*Zheng*, 2014) indicate that ray path of the $S_{660}S$ precursor grazes the eastern boundary of a prominent quasi vertical low velocity anomaly for a fairly long distance, whereas the paths of the $S_{400}S$ precursor and the *SS* phase travel through a high velocity anomaly above the low velocity body. This would predict a significantly longer *SS*-$S_{660}S$ and a normal *SS*-$S_{410}S$ differential travel time, or when converted from time to depth, an apparently normal 410 and a significantly shallower 660, which agrees very well with the discontinuity images here.

Conclusions

We present high resolution topography images of the 410 and 660 discontinuities for a vast region across the Pacific Ocean measured from *SS* precursors. The high density US Transportable Array data combined with a new processing technique, namely the Local Slant Stack Filters (LSSF), have allowed for higher spatial resolution than previous studies. Sensible correlations are observed between several fine-scale heterogeneities in our discontinuity images and corresponding anomalies in the mantle tomography model *SEMum2*.

Acknowledgements

This study was supported by NSF EAR #0738284 and ERC Advanced Grant "WAVETOMO". Data are downloaded from IRIS.

References

Deuss, A., Global observations of mantle discontinuities using SS and PP precursors, *Surv. Geophys. 30*, 301-326, 2009.

French, S., V. Lekic, & B. Romanowicz, Waveform tomography reveals channeled flow at the base of the oceanic asthenosphere, *Science*, *342*(6155), 227-230, 2013.

French S. & B. Romanowicz, Whole-mantle radially anisotropic shear-velocity structure from spectral-element waveform tomography, *Geophys. J. Int.* (submitted), 2014.

Shearer, P.M., Constraints on upper mantle discontinuities from observations of long-period reflected and converted phases, *J. Geophys. Res., 96*, 18147-18182, 1991.

Zheng Z., S. Ventosa, & B. Romanowicz, The application of the Local Slant-Stack Filters (LSSF) for high resolution upper mantle discontinuity imaging, *BSL Annual Report*, 2013.

Zheng Z., Refining Constraints on Seismic Discontinuities and Elastic Structure in the Earth's Upper Mantle, *PhD thesis*, UC Berkeley, California, 2014.

12 Separating Intrinsic and Extrinsic Anisotropy

Thomas Bodin, Yann Capdeville, Barbara Romanowicz

Introduction

It can be proven that if one had an unlimited number of sources, receivers, and an unlimited frequency band, one would be able to entirely describe an elastic medium from the displacement of elastic waves propagating through it, and observed at its surface. However, in seismology there are a number of elements that limit the ability to image structure. Firstly, the seismic records are limited both in time and frequency, and the number of sources and receivers are limited. There are also a number of observational and theoretical errors that propagate into the recovered images.

In recent years, advances in numerical methods such as the spectral element method have allowed us to model more accurately the entire seismic wave-field. Numerically computed seismograms automatically contain the full seismic wavefield, including all body and surface wave phases as well as scattered waves generated by lateral variations of the model Earth properties. The accuracy of the numerical solutions and the exploitation of complete waveform information result in tomographic images that are both more realistic and better resolved (*French et al.*, 2013).

However, computational time increases proportionally to the fourth power of frequency, and limits the frequency range of waveforms to relatively long periods (typically longer than 40 or 50 s for global scale images). Hence the geological interpretation of global tomographic models is limited, mainly due to two reasons:

1. Because the frequency range of global inversions remains limited, and because features smaller than the shortest wavelength cannot be mapped, the constructed images are smooth and do not contain discontinuities that are crucial to understand the structure and evolution of the earth.

2. The relations that link the true earth to the effective (and unrealistic) earth that is seen by long period waves are strongly non-linear and their inverse is highly non-unique. For example, it is difficult to quantitatively interpret the level of imaged anisotropy in tomographic models, as it may be the effect of either real local anisotropy or unmapped velocity gradients such as layering.

Down-scaling Smooth Models

As we have seen, a tomographic inversion of long period waves can only retrieve at best a smooth effective model (and less in the case of an incomplete data coverage). This smooth equivalent earth fits the long period data. However, It is not a simple spatial average of the true earth, but the result of highly non-linear "up-scaling" relations (*Capdeville et al.,* 2010). We propose a novel approach to interpret tomographic images in terms of geological structures (discontinuities). We call this inverse problem the inverse homogenization: for a given smooth 1D profile extracted from a tomographic model, what are the possible fine scale (*i.e.,* layered) models that are equivalent to this smooth 1D profile, *i.e.,* that provide a similar data fit .

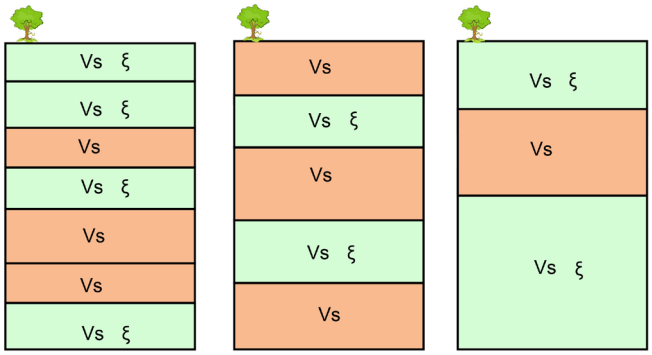

Figure 2.12.1: Adaptive parameterization used for the inverse homogenization. The number of layers as well as the number of parameter in each layer (one for isotropic layers, and two for anisotropic layers) are unknown in the inversion. This is illustrated here with three different models with different parameterizations. The parameterization is itself an unknown to be inverted for during the inversion scheme. Of course, data can always be better fitted as one includes more parameters in the model, but within a Bayesian formulation, preference will be given to simple models that explain observations with the least number of model parameters.

Although there is an infinite number of layered models that are equivalent to a smooth tomographic profile, these models share common features, and Bayesian statistics can be used to appraise this ensemble. In particular, a probabilistic approach allows us to quantify the trade-off between anisotropy and heterogeneity. Indeed, a smooth anisotropic model can either be explained by a large number of isotropic layers or by a few anisotropic layers. To break this trade-off, and distinguish between real anisotropy and small-scale layering, higher frequency data sensitive to discontinuities, such as receiver functions, can be used to constrain the location of horizontal discontinuities.

As shown in Figure 2.12.1, we describe our layered models with a transdimensional parameterization (*Bodin et al.,* 2014), where the number of layers, as well as the number of parameters per layer are free variables, *i.e.,* unknown parameters In this way, the number of layers will be variable in the ensemble solution, as well as the number of parameters in each layer: 1 for isotropic layers (V_S) and 2 for anisotropic layers (V_S and ξ).

A Probabilistic Seismic Model Under the North-American Craton

We construct a 1D probabilistic seismic profile under North-West Canada, by combining in a joint Bayesian inversion a full-waveform radially anisotropic tomographic profile (SEMum2, *French et al.*, 2013) with receiver functions.

The goal here is to investigate the structure and history of the North American craton. At the same time, we explore whether lithospheric layering as seen by scattered body waves (receiver functions) is compatible with the radial anisotropy imaged

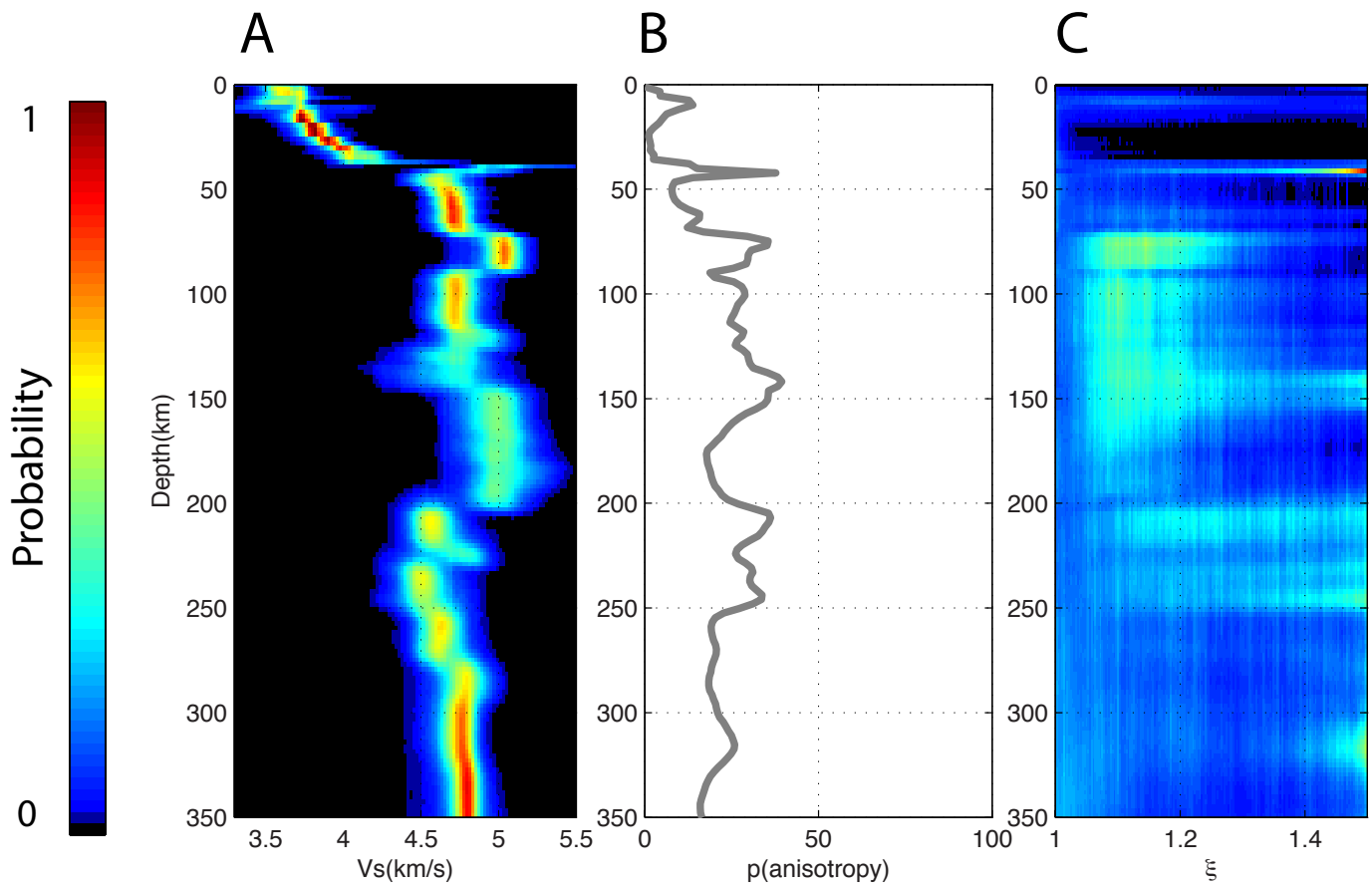

Figure 2.12.2: Left Probability distribution for Vs. Middle: probability of having an anisotropic layer. Right: probability for ξ .

from global tomography.

The solution is given by an ensemble of 1D models with variable number of layers, thicknesses, and elastic parameters. Figure 2.12.2A shows the marginal distribution for S-wave velocities as a function of depth, simply constructed from the density plot of the ensemble of models in the solution. Here a number of expected lithospheric discontinuities have been imaged, such as the mid-lithospheric discontinuity at 90 km and a sharp lithosphere-asthenosphere boundary at 200 km.

Since here we are interested in the relative contribution of layering to the observed anisotropy in SEMum2, we can look at the probability at each depth to have intrinsic anisotropy. For each model, each layer is either isotropic or anisotropic. Therefore, at each depth, one can count the ratio of isotropic to anisotropic layers in the ensemble of models. When no information is brought by the data (prior distribution), the probability to have anisotropy is 50%. However here, the probability is lower and around 20% across much of the depth profile. This implies that intrinsic anisotropy is not required to fit the smooth tomographic profile. In other words, the discontinuities required to fit the converted body waves may be enough to explain the anisotropy in the tomographic model. We view this as an important result, indicating that radial anisotropy (at least under cratons) should not be directly interpreted in tomographic models.

The third panel in Figure 2.12.2C shows the probability distribution for ξ at each depth. Note that, for a given depth, around 80% of models are isotropic with $\xi = 1$, and this distribution only represents the level of anisotropy in the 20% remaining models.

Acknowledgements

This project was supported by the French-Berkeley Fund (FBF). Thomas Bodin wishes to acknowledge support from the Miller Institute. Computational resources were also provided by the Institutional Computing program of LANL.

References

Bodin T., H Yuan, B Romanowicz, Inversion of receiver functions without deconvolution—application to the Indian craton- Geophys. J. Int. doi:10.1093/gji/ggt431, 2014.

Capdeville Y., Guillot, L., and Marigo, J., 1-d non periodic homogenization for the seismic wave equation. Geophys. J. Int. 181 (2), 897-910, 2010.

French, S., Lekic, V., & Romanowicz, B., Waveform tomography reveals channeled ow at the base of the oceanic asthenosphere, Science, 342(6155), 227-230, 2013.

Research Studies:
Rheology and Fault Mechanics

13 Probing the Lithospheric Rheology Across the Eastern Margin of the Tibetan Plateau

Mong-Han Huang, Roland Bürgmann, Andrew M. Freed (Dept. of Earth, Atmospheric, and Planetary Sciences, Purdue University, IN)

Introduction

The fundamental geological structure, geodynamics, and rheology of the Tibetan Plateau have been debated for decades. Two end-member models have been proposed: (1) the deformation of Tibet is broadly distributed and associated with ductile flow in the mantle and middle or lower crust, (2) the Tibetan Plateau formed during interactions between rigid lithospheric blocks with localized deformation along major faults. The nature and distribution of continental deformation is governed by the varying rheology of rocks and faults in the lithosphere. Insights into lithospheric rheology can be gained from observations of postseismic deformation, which represent the response of the Earth's interior to coseismic stress changes. Here we use up to 2 years of interferometric synthetic aperture radar (InSAR) and GPS measurements to investigate postseismic displacements following the 2008 M_w7.9 Wenchuan earthquake in eastern Tibet and probe the differences in rheological properties across the edge of the Plateau. We find that near-field displacements can be explained by shallow afterslip on the Beichuan Fault (BCF), which is anti-correlated with the coseismic slip distribution. Far-field displacements cannot be explained with a homogeneous rheology, but instead require a viscoelastic lower crust (from 45–60 km depth) beneath Tibet and a relatively strong Sichuan block. The inferred strong contrast in lithospheric rheologies between the Tibetan Plateau and the Sichuan Basin is consistent with models of ductile lower crustal flow that predict maximum topographic gradients across the Plateau margins where viscosity differences are greatest.

Postseismic Deformation

A number of processes contribute to postseismic deformation. Afterslip is the continuous slip of the fault after the mainshock and is often found to occur downdip of the fault rupture zone. We use a dislocation model in a layered Earth structure to investigate the afterslip distribution by inverting the geodetic data. We modify the fault geometry proposed by *Shen et al.* (2009) and extend the fault depth to 65 km depth for afterslip at the downdip extension (Figure 2.13.1a). The afterslip occurs on both shallow and deep parts of the BCF that represent the fit to the near- and far-field displacements.

We use a 3D finite element model (*Huang et al.*, 2014) to construct a regional rheologic model composed of an elastic Tibet upper crust and Sichuan crust, a viscoelastic Tibet lower crust, and a viscoelastic upper mantle. We use the bi-viscous Burger's rheology to represent the transient and steady state periods of the postseismic deformation. The Burger's rheology is composed of a Maxwell fluid connected in series with a Kelvin solid to represent the steady state and transient viscosities. The best-fitting model involves a low-viscosity lower crust in Tibet between 45 and 60 km in depth.

Constraining Tibet's Lithospheric Rheology

A Maxwell fluid with a constant viscosity fails to explain the postseismic displacement rate changes, and shows the need for a model in which the effective viscosity increases with time. The change of effective viscosity implies either transient rheology or stress-dependent power-law rheology or both. In this study, we try to distinguish the main mechanism that contributes to the postseismic displacements and the contrasting rheology between Tibet and Sichuan, and thus adopt a simple bi-viscous Burgers rheology. As the viscoelastic relaxation model can explain most of the early postseismic transients in the middle field, we can rule out afterslip as being the major cause of the initial rapid displacements. The best-fitting model predicts a transient viscosity (ηK) of 1017.9 Pa s and a steady-state viscosity (ηM) of 1018 Pa s, whereas the Sichuan Basin block has a high-viscosity upper mantle (> 1020 Pa s) underlying an elastic 35 km-thick crust

Models of Tibetan lower crustal channel flow predict that the Plateau margins are steepest where the viscosity of the surrounding blocks are highest, and thus impede and divert the flow (*Clark et al.*, 2005). These models predict the strongest viscosity contrasts with the Sichuan and Tarim Basin blocks (η = 1016–18 Pa s in a 15–20 km thick lower crustal layer versus ~1020–21 Pa s in adjacent crust), where topographic gradients are greatest. Our preferred viscosity structure deduced from the postseismic deformation transients across the Longmen Shan is consistent with such contrasting lithospheric rheology and deformation between eastern Tibet and the Sichuan Basin.

Acknowledgements

We thank D. Dreger, Z. Shen, I. Ryder, and F. Pollitz for discussions and constructive suggestions. This work is support by the National Science Foundation grant (EAR-1014880).

References

Clark, K. M., Bush, J. W. M., and Royden, L. H. Dynamic topography produced by lower crustal flow against rheological strength heterogeneities bordering the Tibetan Plateau. *Geophys. J. Int.*, 162, 575-590, 2005.

Huang, M.-H, Bürgmann, R., and Freed, A. M. Probing the lithospheric rheology across the eastern margin of the Tibetan Plateau. *Earth Planet Sci. Lett.*, 396, 88-96, 2014.

Shen, Z.K., J. Sun, P. Zhang, Y. Wan, M. Wang, R. Bürgmann, Y. Zeng, W. Gan, H. Hiao, and Q. Wang, Slip maxima at fault junctions and rupturing of bariers during the 2008 Wenchuan earthquake, *Nat. Geosci.*, 2, 718-724, 2009.

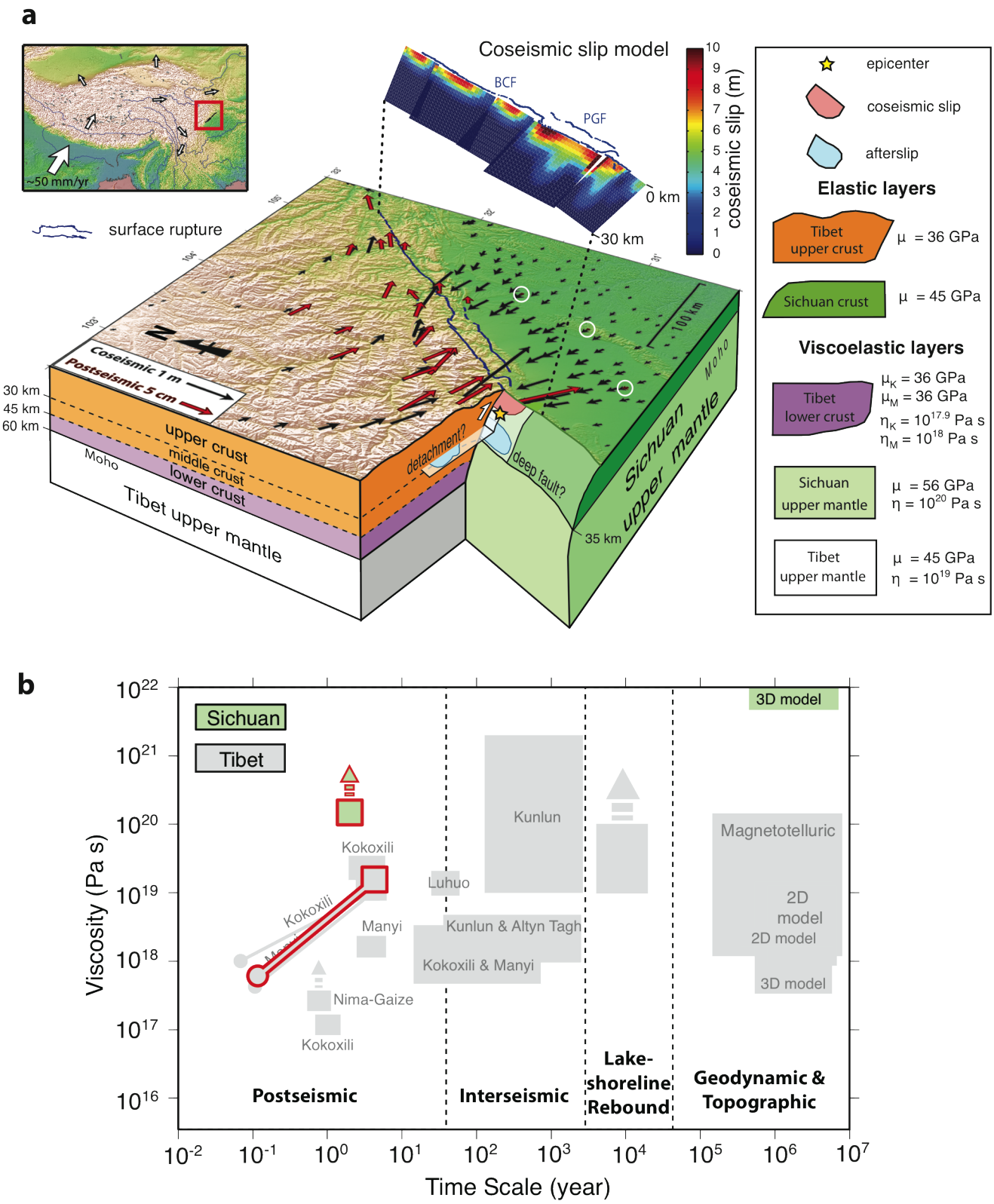

Figure 2.13.1: (a) Three-dimensional representation of eastern Tibet. The upper left map shows the Tibetan Plateau. The black and red arrows in the 3D block diagram are the co- and estimated first year postseismic GPS measurements. The detachment and deep faults are based on *Shen et al.* (2009). The coseismic slip is based on *Huang et al.* (2014). (b) Viscosity estimates of Tibet's lower crust for different time scales. The rectangles represent the range of viscosity of the lower crust estimated using constraints for different time scales. The circles represent the initial effective viscosity of a Burgers-type rheology. The arrows above the rectangles indicate that the estimated viscosity represents a lower bound. The estimated value for the Sichuan block (green square) is for the mantle below 35 km depth.

14 Post 1989 M_w 6.9 Loma Prieta Earthquake Viscous Relaxation Revealed from GPS and InSAR Data

Mong-Han Huang, Roland Bürgmann, Ingrid Johanson, Fred Pollitz (U.S. Geological Survey)

Introduction

The 1989 M_w 6.9 Loma Prieta earthquake provided the first opportunity to probe the crustal and upper mantle rheology in the San Francisco Bay Area since the 1906 M_w 7.9 San Francisco earthquake. Here we use geodetic observations including GPS and InSAR to characterize the 1989 M_w 6.9 Loma Prieta earthquake postseismic displacement from 1989.8 to 2013. Pre-earthquake deformation rates are constrained by nearly 20 years of USGS trilateration measurements and removed from the postseismic measurements prior to the analysis. We observe 1–4 mm/yr GPS horizontal displacement toward the Loma Prieta epicenter, and ~2 mm/yr land subsidence in Almaden, Ca between 1992 and 2002 followed by ~1 mm/yr uplift until 2013. Insights into lithospheric rheology can be gained from observations of postseismic deformation, which represent the response of the earth's interior to coseismic stress changes. We model the viscoelastic relaxation by assuming a viscoelastic 11 km-thick lower crust below a 19 km-thick elastic upper crust, underlain by a viscoelastic upper mantle. The best fitting model is composed of an elastic upper crust, a viscous lower crust ($\eta = 10^{19}$ Pa s), and a bi-viscous upper mantle ($\eta_M = 10^{18}$ Pa s; $\eta_K = 10^{17}$ Pa s), which is consistent with rheologic studies in southern California and models of the post-1906 relaxation. Repeating earthquake activities following the Loma Prieta event seem to correlate with surface displacement, both driven by the viscoelastic relaxation from the upper mantle

The Postseismic Deformation

We mainly use GPS data collected by *Segall et al.* (2000) for the early period (1989.8–1998), and later period (1994–2013) data are obtained from USGS measurements (http://earthquake.usgs.gov/monitoring/gps) (*Savage and Svarc*, 2010). Figure 2.14.1a shows the GPS observed first 5 years, 5–10 years, and 10–15 years postseismic deformation, after removing secular interseismic motion. For the first 5 years, the postseismic displacement (red arrows in Figure 2.14.1a) is generally less than 5 cm near the Loma Prieta earthquake area. The postseismic displacement after the first 5 years is significantly smaller (orange and blue arrows in Figure 2.14.1a). In addition, there is a change of direction in postseismic deformation after the first 5 years. *Segall et al.* (2000) estimated time-dependent afterslip on the fault plane using GPS data collected between 1989.8 and 1998.3. They found that the afterslip dominated the postseismic deformation until 1994, which may explain the change of the direction in postseismic deformation 5 years after the main shock.

Viscoelastic Relaxation

We consider simple elastic coseismic dislocations to calculate the coseismic stress changes and the postseismic relaxation in a layered viscoelastic representation of the earth's lithosphere to evaluate the inferred surface deformation. We assume Earth's upper crust (0–19 km in depth) as elastic, and the lower crust (19–30 km) and upper mantle (below 30 km) are both viscoelastic. We vary the viscosities of the lower crust and upper mantle between 10^{17} and 10^{20} Pa s. The bi-viscous upper mantle with transient (η_K) and steady-state (η_M) viscosities can allow for transient deformation following the Loma Prieta main shock. We calculate the misfit between the GPS time series and the predicted viscoelastic relaxation models to investigate the crustal and upper mantle rheology. Figure 2.14.1b and c show the fitting of predicted viscoelastic relaxation to early and late postseismic periods. We only calculate the misfit between 1994 and 2007 in order to avoid the afterslip driven postseismic deformation between 1989.8 and 1994. The best fitting model (Figure 2.14.1c) predicts a viscosity of the upper mantle that is about 10 times lower than the lower crust.

Our results show evidence that afterslip in the shallower portion of the coseismic fault plane dominates the early (1989.8-1994) Loma Prieta postseismic deformation. The postseismic deformation after 1994 resulted from the viscoelastic relaxation of the upper mantle and lower crust. The predicted upper mantle viscosity is ~10^{18} Pa s (Figure 2.14.1d), which is in good agreement with upper mantle rheology in southern California based on a similar approach.

Acknowledgements

The authors would like to thank D. Dreger, E. Chaussard, R. Turner, and J. Suppe for discussions and constructive suggestions. All of the USGS GPS campaign data are downloaded from the USGS website. This project is supported by the National Science Foundation grant (EAR-0951430) and NASA (NXX-08AG50G).

References

Pollitz, F., Bürgmann, R., and Segall P. Joint estimation of afterslip rate and postseismic relaxation following the 1989 Loma Prieta earthquake. *J. Geophys. Res.*, *103*, 26975-26992, 1998.

Segall, P, Bürgmann, R., and Matthews, M. Time-dependent triggered afterslip following the 1989 Loma Prieta earthquake. *J. Geophys. Res.*, *105*, 5615-5634, 2000.

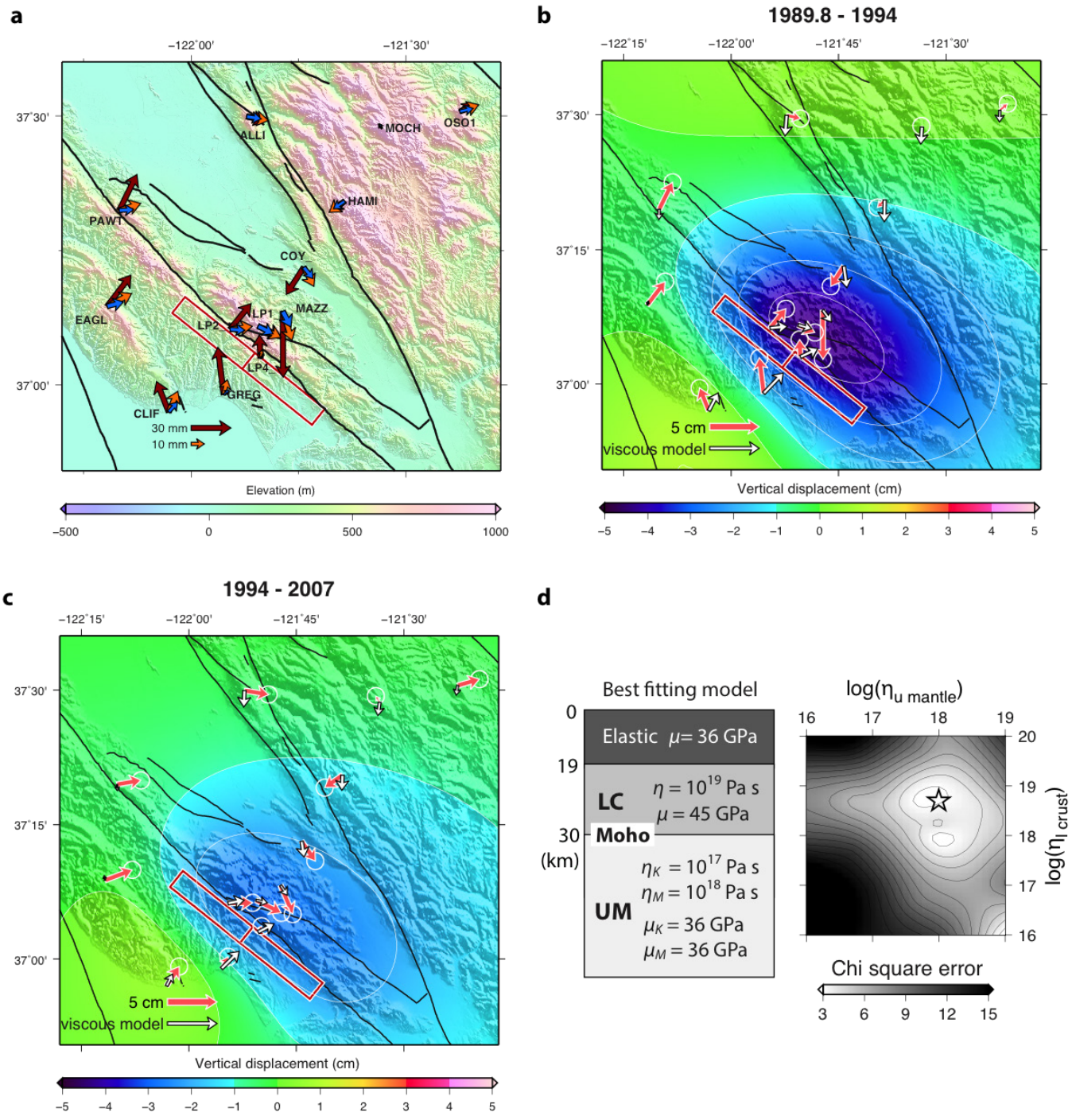

Figure 2.14.1: (a) The arrows show the postseismc deformation of the Loma Prieta earthquake in different periods (red: 1989.8–1994; orange: 1994–1999; blue: 1999–2004), and all of the measurements are relative to the average displacement of stations HAMI, MOCH, and OSO1. The red rectangles are the coseismic fault planes (*Pollitz et al.*, 1998), and the black lines are the fault lines in the Bay Area. Note the change of amplitude and direction of the postseismic displacement in different periods. (b) Predicted viscoelastic relaxation in the first four years (1989.8–1994). The pink arrows are GPS displacement estimated based on the time series downloaded from the USGS website (http://earthquake.usgs.gov/monitoring/gps) and *Segall et al.* (2000), and the white arrows are the viscoelastic model predictions. The background color represents the vertical displacement due to the viscoelastic relaxation. (c) Predicted viscoelastic relaxation between 1994 and 2007. Note the viscoelastic fitting to the later period is better than the early period, hence implying the early period may be dominated by afterslip, which agrees with *Segall et al.* (2000). (d) Left: The model fitting and the rheologic structure based on the best-fitting viscoelastic relaxation model. Right: The chi-square error distribution with different combinations of lower crust and upper mantle viscosities.

15 Upper Mantle Rheology Illuminated from the 2011 Tohoku-Oki Earthquake

Yan Hu, Roland Bürgmann

Introduction

Viscoelastic postseismic deformation of the devastating M_w9.0 Tohoku earthquake has been recorded at more than 1200 continuous Global Positioning System (GPS) and six GPS/Acoustic (GPS/A) stations offshore (Figure 2.15.1). The high quality data in NE Japan provide a unique opportunity for us to better understand the three dimensional (3D) upper mantle rheology and distribution and evolution of the afterslip of the megathrust event.

In this work, we integrate the wealth of geodetic data from NE Japan and modeling experiences developed at other margins to investigate the effects of mantle rheology on postseismic deformation following the 2011 earthquake (*Hu et al.*, 2014).

Finite Element Model

We use a 3D finite element model (FEM) that is able to incorporate the complex slab geometry and tectonic structure in the real Earth. The model shown in Figure 2.15.1 consists of an elastic upper plate, an elastic subducting plate, a viscoelastic continental mantle wedge, and a viscoelastic oceanic upper mantle. Time-dependent, stress-driven afterslip of the fault is simulated by a 2 km-thick weak shear zone attached to the fault. Locked portions of the shear zone are outlined from historic asperities in NE Japan and 5 m coseismic slip contours of the 2011 Earthquake (*Hu et al.*, 2014). Reference rock properties of each tectonic unit are labeled in Figure 2.15.1.

Bi-viscous Burger's rheology (*Bürgmann and Dresen*, 2010) is assumed to represent the viscoelastic behavior of the rheological units. In this work, we assume that the transient Kelvin viscosity is one order of magnitude lower than the steady-state Maxwell viscosity. At shallow depths of the shear zone (≤50 km), the stead-state viscosity is constrained from repeating earthquakes (*Uchida et al.*, 2013) and is 10^{17} Pa s. We vary the viscosity in the deep shear zone (10^{16}–10^{20} Pa s), mantle wedge (10^{18}–10^{21} Pa s) and oceanic mantle (10^{19}–10^{22} Pa s) and construct hundreds of test models. We then calculate the total misfit for each test model for time windows of 6 months, 1 year, 1.5 years and 2 years. The minimal misfit is thus the preferred finite element model of NE Japan.

Model Results

Out test models indicate that the viscosity of the deep shear zone may be traded-off by the mantle wedge viscosity (Figure 2.15.2c). The range in the viscosities of the deep shear zone, mantle wedge and oceanic mantle are 10^{17}–5×10^{18} Pa s, 7×10^{18}–5×10^{19} Pa s, and 5×10^{19}–5×10^{20} Pa s (Figure 2.15.2). In the best-fit model, that is, the model of minimal misfit shown in Figure 2, viscosities of the deep shear zone, mantle wedge and oceanic mantle are 10^{18} Pa s, 10^{19} Pa s, and 10^{20} Pa s, respectively. The best-fit model successfully reproduces the first-order pattern of the GPS observations both on land and offshore (Figure 2.15.3). Cumulative afterslip simulated in the weak shear zone is up to ~3.5 meters two years after the earthquake (Figure 2.15.3a). The equivalent moment magnitude of the afterslip is 8.39.

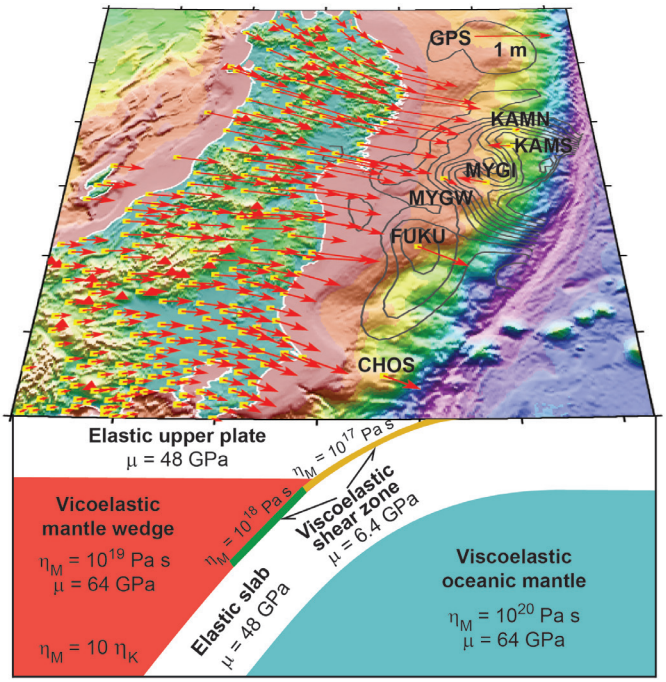

Figure 2.15.1: GPS observations (red arrows) in NE Japan and conceptual representation of the finite element model. μ, η_M, and η_K are shear modulus, steady-state and transient viscosities, respectively. Poisson's ratio is assumed to be 0.25 for the entire domain. Grey contours are coseismic slip distribution (*Iinuma et al.*, 2012).

We also study effects of the following second-order processes on the surface deformation. (1) We study poroelastic rebound in the top 6 km continental and top 16 km oceanic lithosphere (Figure 2.15.4a). (2) The lower crust beneath the arc may be weakened by fluids dehydrated from the subducting slab, and its viscosity is believed to be several orders of magnitude lower than that of the surrounding material (Figure 2.15.4b). (3) We include the elastic Philippine Sea (PHS) slab and a weak shear zone attached to the subducting PHS slab (Figure 2.15.4c). (4) We consider a 200 km-thick weak asthenosphere beneath the oceanic lithosphere (Figure 2.15.4d). Figure 2.15.4 illustrates contributions to the viscoelastic postseismic deformation only due to these second-order processes above.

Acknowledgements

We are thankful for the computing facility provided by Bruce Buffett, and thankful for the publicly available GPS time series of GEONET by GSI. This work was funded by NSF award EAR-1246850 and benefited from support by the Miller Institute for Basic Research in Science.

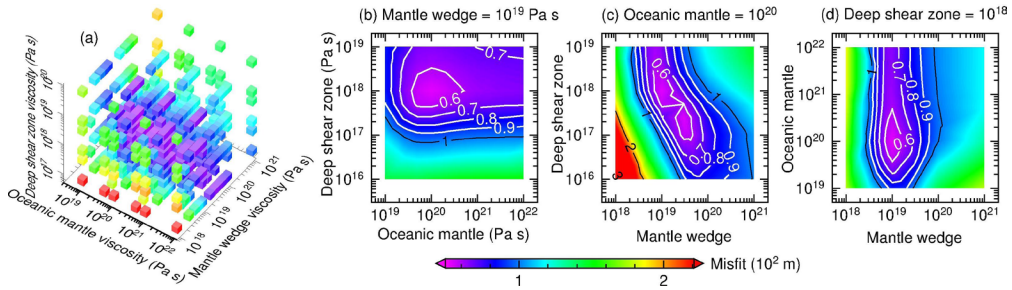

Figure 2.15.2: Systematic tests on the rheology of the deep shear zone, mantle wedge and oceanic mantle. (a) Misfit of the test models in terms of the steady-state viscosity in the rheological units. Each cube represent one test model. (b-d) Trade-off between the viscosities in two rheological units while the viscosity of the third unit is fixed. Color contours are total misfit and are the same as the line contours.

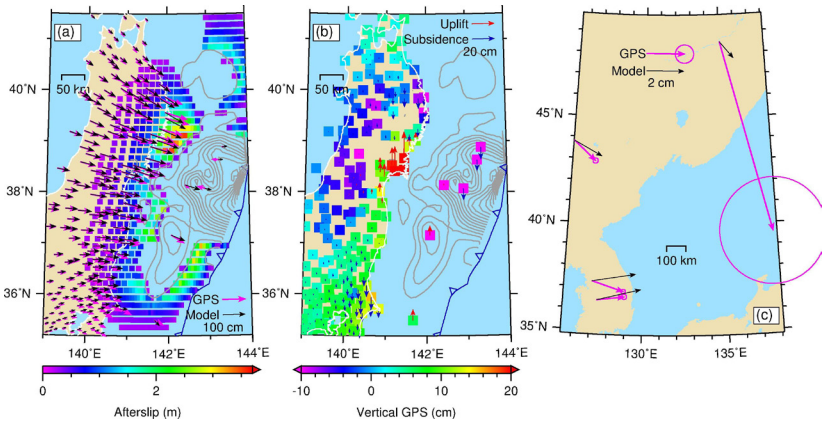

Figure 2.15.3: Comparison of GPS observations with the best-fit model two years after the earthquake. (a) Magenta and black arrows are GPS and model-predicted displacements, respectively. Color contours are afterslip in meters simulated by the weak shear zone. (b) Red and blue arrows are modeled uplift and subsidence, respectively. Color contours are the observed vertical displacements. (c) Similar to (a), very-far-field displacements.

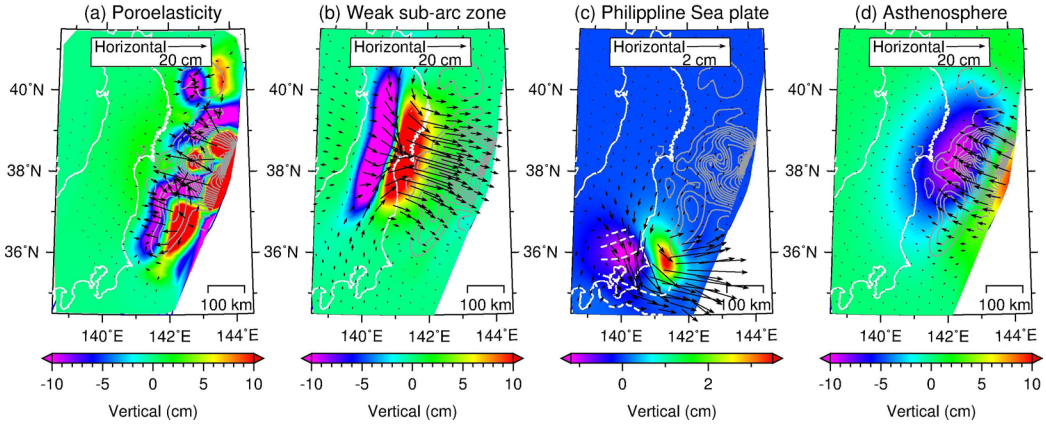

Figure 2.15.4: Surface deformation due to second-order processes, such as poroelastic resbound in the top layer of the lithosphere (a), fluids-weakened zone beneath the arc (b), afterslip in the subducting Philippine Sea slab (c), and weak asthenosphere beneath the oceanic lithosphere (d). Black arrows and color contours are horizontal and vertical displacements two years after the earthquake except in (a), respectively.

References

Bürgmann, R., and G. Dresen, Rheology of the lower crust and upper mantle: Evidence from rock mechanics, geodesy, and field observations, *Annu. Rev. Earth Planet. Sci.*, *36*, 531–567, doi:10.1146/annurev.earth.36.031207.124326, 2008.

Hu, Y., et al., Contributions of poroelastic rebound and a weak volcanic arc to the postseismic deformation of the 2011 Tohoku earthquake, *Earth Planet Science*, under review, 2014.

Iinuma, T., et al., Coseismic slip distribution of the 2011 off the Pacific Coast of Tohoku Earthquake (M9.0) refined by means of seafloor geodetic data, *J. Geophys. Res.*, *117*, B07409, doi:10.1029/2012JB009186, 2012.

Uchida, N., and T. Matsuzawa, Pre- and postseismic slow slip surrounding the 2011 Tohoku-oki earthquake rupture, *Earth Planet. Sci. Lett.*, doi:10.1016/j.epsl.2013.05.021i, 2013.

16 Geodetic Tracking and Characterization of Precipitation-Triggered Slow Moving Landslide Displacements in the Eastern San Francisco Bay Hills, California, USA

Julien Cohen-Waeber, Roland Bürgmann, Nicholas Sitar, Alessandro Ferretti, Chiara Giannico, Marco Bianchi

Introduction

Contemporary geodetic technologies, such as continuous Global Positioning Systems (GPS) and Interferometric Synthetic Aperture Radar (InSAR), allow for remote detection and characterization of ground surface displacements with sub-centimeter precision and accuracy. These technologies are complementary with one another in that GPS allows real time tracking of a finite point while InSAR time series analyses allow widespread surface deformation tracking, though still far from real time.

This project combines GPS and InSAR for the temporal and spatial characterization of landslide deformation. Both methods have shown accelerated surface deformation as an effect of precipitation, though not in relation to recent seismic activity. These observations also suggest intra-slide deformation patterns not previously measurable. Ultimately, both InSAR and GPS studies not only confirm strong correlation and sensitivity to periods of precipitation, but similar kinematic behavior and downslope sliding velocities of around 30 mm/year.

InSAR Time Series Analyses

A review of three independent InSAR time series analyses of landslides in the Berkeley Hills, from separate satellite acquisitions and over different time intervals from 1992–2011 shows remarkable consistency (*Hilley et al.,* 2004*, Quigley et al.,* 2010*, Giannico et al.,* 2011). In each case, surface deformation showed a clear correlation to precipitation, with similar mean downslope velocities (approx. 30 mm/year) and periods of acceleration during each wet season. These studies also suggest observable internal deformation when each slide is divided into groups of coherently moving masses and different sections mobilize separately (*Quigley et al.,* 2010*, Cohen-Waeber et al.,* 2013).

In Figure 2.16.1 (Top), the study of TerraSAR-X data acquisitions from 2009–2011, (*Giannico et al.,* 2011) utilizing the SqueeSARTM algorithm by Tele-Rilevamento Europa (*Ferreti et al.*, 2011), confirms these displacement trends in different parts of the same landslide. In this case, a significantly higher spatial resolution revealed that these slides are in fact moving as bodies of smaller coherent masses. By differencing the average displacements of the top, middle and bottom of the landslides, a pattern of apparent extension then shortening with the progression of precipitation is visible, in what could be called an "accordion effect" (*Cohen-Waeber et al.,* 2013). Figure 2.16.1 (Bottom) illustrates early seasonal acceleration and deceleration of the lower landslide portions in contrast to the upper landslide portions.

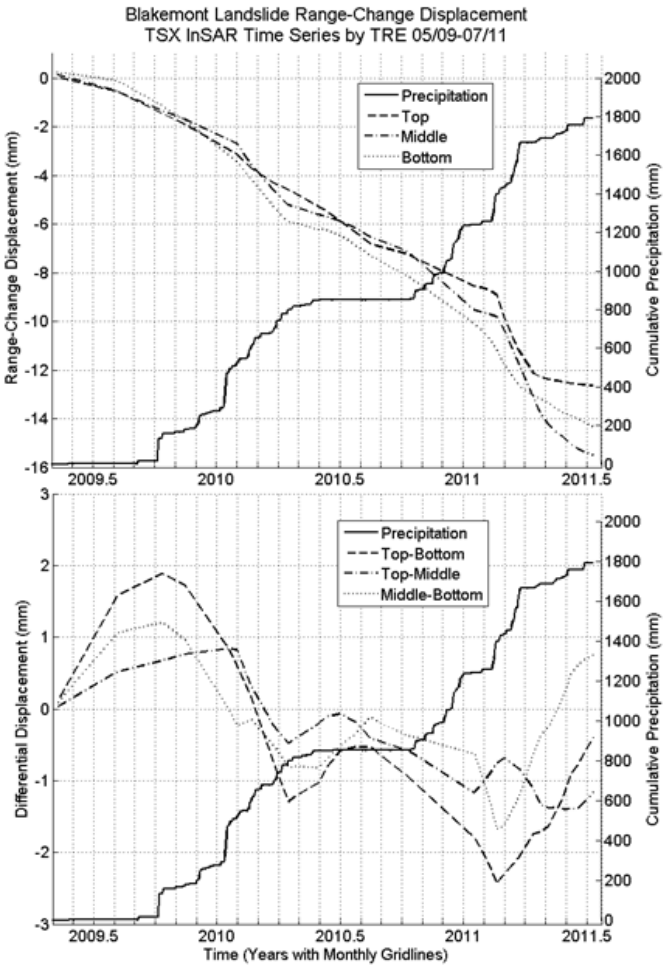

Figure 2.16.1: (TOP) Average downslope range-change displacement and (BOTTOM) differential of average downslope displacements from TRE SqueeSARTM analysis of TerraSAR-X data acquisitions (2009–2011) in areas of Blakemont Landslide, versus cumulative precipitation (right axes).

Continuous GPS Tracking

To fully capture temporal landslide surface displacements, seven continuous GPS stations were installed on Lawrence Berkeley Laboratory (LBL) and Berkeley hills landslides, with data collection rates of 1 Hz for average daily solutions and 20 Hz in case of seismic activity. Each station is anchored on deep seated, reinforced concrete foundations and its measurements differenced from a near-by stable monument to limit non-landslide displacements as tectonic activity, clay activity or atmospheric error.

Through three mild wet seasons (since January 2012), well-defined precipitation-triggered slope movement has been

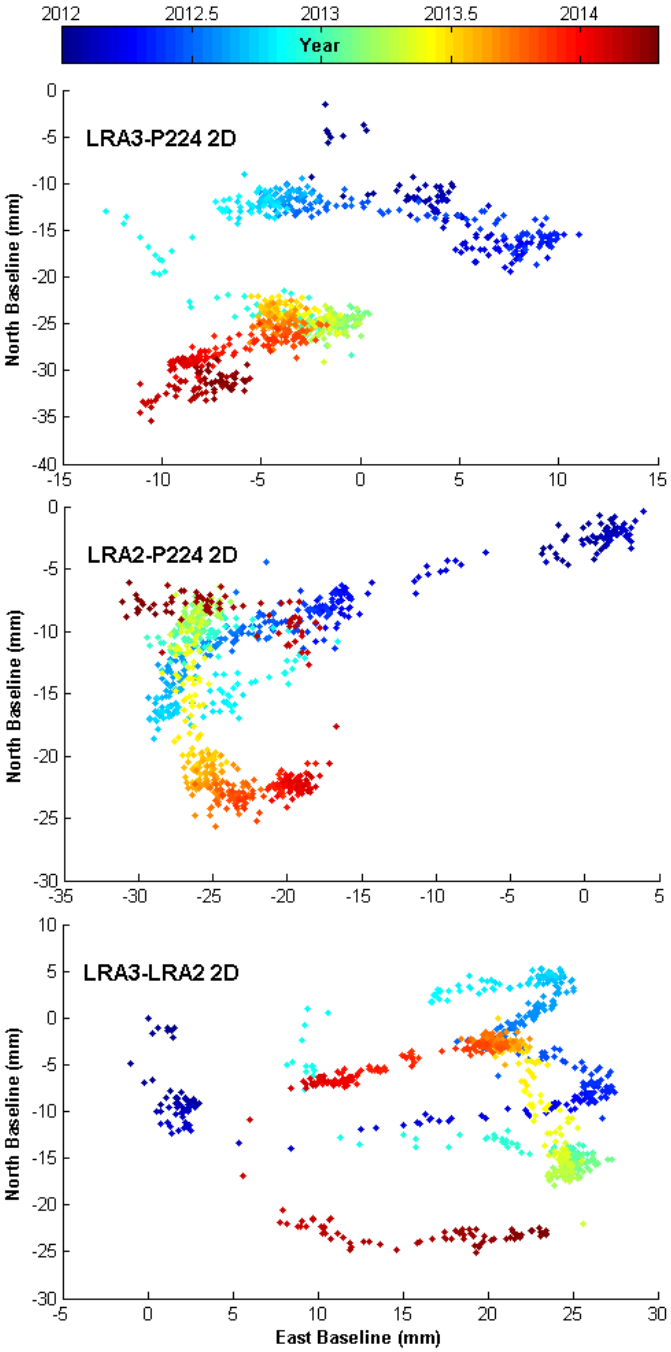

Figure 2.16.2: GPS displacement time series of stations LRA3 (TOP) and LRA2 (MIDDLE) with respect to reference station P224 approximately 5 km to the southeast. Both stations are located on the same landslide and suggest internal differential movement when differenced (BOTTOM).

recorded from daily solutions, as shown through the displacement time series of stations LRA1 and LRA2 (Figure 2.16.2, Top, Middle). While an apparent antenna oscillation can be attributed to seasonal disturbance from surficial clay activity, the stations exhibit overall downslope displacements with similar average velocities as shown through the InSAR analyses. Furthermore, differencing these two stations located on the same landslide captures a sense of internal deformation and suggests the same "accordion effect" (Figure 2.16.2, Bottom).

Preliminary Conclusions

InSAR and GPS have demonstrated here their capability to record and characterize landslide motions that otherwise would not have been observed with such level of detail. While both methods of observation have not yet been compared on one landslide over the same period, they are complementary. Overall, our observations from several studies have yielded similar precipitation triggered down-slope velocities, and comparable internal mechanisms, exhibiting progressive accordion-like downslope failure typical to slow moving flow slides. Ultimately, tracking over longer periods will provide important insight on the triggering mechanisms and internal landslide behaviors described, including yet to be recorded seismically induced landslide motions.

Acknowledgements

We gratefully acknowledge our financial support from the Lawrence Berkeley National Laboratory, Earth Science Division Director's fund.

References

Cohen-Waeber J. et al., GPS Instrumentation and Remote Sensing Study of Slow Moving Landslides in the E. San Francisco Bay Hills, CA, *Proceedings of the 18th Int. Conf. on Soil Mech. and Geotech. Eng.*, Paris, France, 2013.

Ferretti A. et al., A New Algorithm for Processing Interferometric Data-Stacks: SqueeSAR, *IEEE Geoscience and Remote Sensing 49(9)*, 3460-3470, 2011.

Giannico C. and Ferretti A., SqueeSARTM Analysis Area: Berkeley, *Processing Report*, Tele-Rilevamento Europa, Milano, IT, 2011.

Hilley G.E. et al., Dynamics of Slow Moving Landslides From Permanent Scatterer Analysis, *Science 304*, 1952-1955, 2004.

Quigley K. C. et al., Seasonal Acceleration and Structure of Slow Moving Landslides in the Berkeley Hills.,*Proc. of the 3rd Conf. on Earthquake Hazards in the E. San Francisco Bay Area*; edited by Keith Knudsen, CA Geol. Surv. Special Report 219, 169-178, 2010.

17 Temporal Changes in Seismic Velocity with Fluid Injection at The Geysers Geothermal Field, California

Voon Hui Lai, Taka'aki Taira, Douglas Dreger, Mong-Han Huang

Introduction

The effort to increase the production of geothermal power by injection of fluid is often hampered by the concern over the induced seismicity which accompanies the geothermal operations. Changes in seismic wave velocities can act as a proxy to stress changes at a reservoir, providing information about the structural change due to fluid movement or natural tectonic events. Traditional observations from measuring repeating natural and active seismic sources are limited because the seismic sources are episodic. By apply the method of cross-correlating seismic noise between two receivers (*Shapiro and Campillo,* 2004), we are able to retrieve Green's functions which are highly sensitive to velocity changes as the waves are scattered back and forth throughout the medium enhancing the signal of time delays due to a velocity change along their path.

This ambient noise correlation technique has been applied to study temporal variations in crustal properties at several geological settings including the San Andreas Fault at Parkfield, CA and volcanoes (*Brenguier et al.,* 2008a; *Brenguier et al.,* 2008b). In this paper, we use a similar approach to study the temporal seismic variations at the Geysers Geothermal Field, CA, towards understanding the controlling factors of the seismic velocity variations and the mechanics of how stress changes at a geothermal environment.

Location

The Geysers in Northern California is one of the world's largest geothermal fields, with over 350 operating production and injection wells, and is also a very seismically active region.

In early 2012, the Northern California Earthquake Data Center (NCEDC), in collaboration with the Lawrence Berkeley National Laboratory (LBNL), the Berkeley Seismological Laboratory (BSL), and the U.S. Geological Survey (USGS), began to collect continuous data at the Geysers using its BG network consisting of 30 short-period (4.5 Hz) geophones, translating into 435 possible combinations of station pairs with average distance between stations within 5 km (Figure 2.17.1). The dense seismic network at the Geysers provides a unique opportunity to conduct studies on ambient seismic noise monitoring.

Methodology

For the analysis, we use the Rayleigh-dominant time series obtained from the vertical component of the continuous seismic record from March 16, 2012 to December 31, 2013 (656 days). To prepare the data, we remove the instrument response and mean, and apply a whitening procedure to broaden the frequency band of the ambient seismic data in cross-correlation and remove effects from noise sources with specific frequencies. The

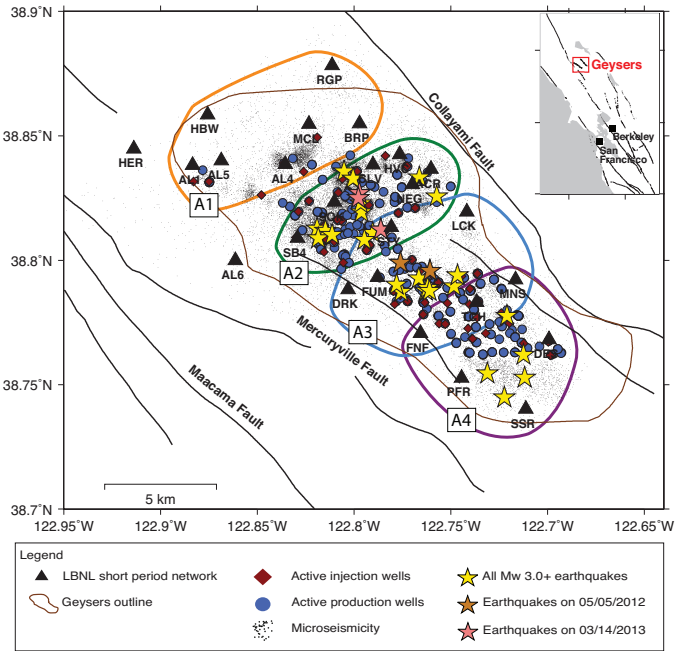

Figure 2.17.1: Map of the Geysers showing locations of the geophones (triangles), active production (diamonds) and injection wells (circles), and *M*3.0+ earthquakes (stars) during the study region. Orange and pink stars mark the location of *M*4.0+ earthquakes and its aftershocks on May 5, 2012 and March 14, 2013. For subsequent analysis, the study region is divided into four smaller areas, each consisting of 6–7 geophones.

frequency range we use for the noise correlation is 0.5–0.9 Hz, which is sensitive to the reservoir depth (less than 3 km).

Before cross-correlation, we divide the records into shorter, overlapping time windows as described in *Seats, Lawrence, and Prieto* (2012). After obtaining the hourly noise correlation functions, we further stack the time series using a time window of 1 day and subsequently 30-days, to be consistent with the temporal resolution of the geothermal operations data, which come in a monthly basis. Lastly, we apply the stretching method described in *Wegler et al.* (2009) to measure the relative seismic velocity shift (dv/v) between each daily Green's function and the reference Green's function.

The expected dv/v value is very small (< 1%) hence stringent data quality control is necessary. First in the preparation stage, data with time gaps due to occasional telemetry dropouts are removed from the analysis. We review the power density spectral plot for each station and reject stations with an unstable noise spectrum around 0.1–0.9 Hz. In the measurement phase, we only accept the dv/v measurement when the daily Green's function and reference Green's function show similarity with a coherence value above 0.8. Finally, we remove Green's functions for pairs of stations in which one of them consistently produces a poor coherence value below 0.5.

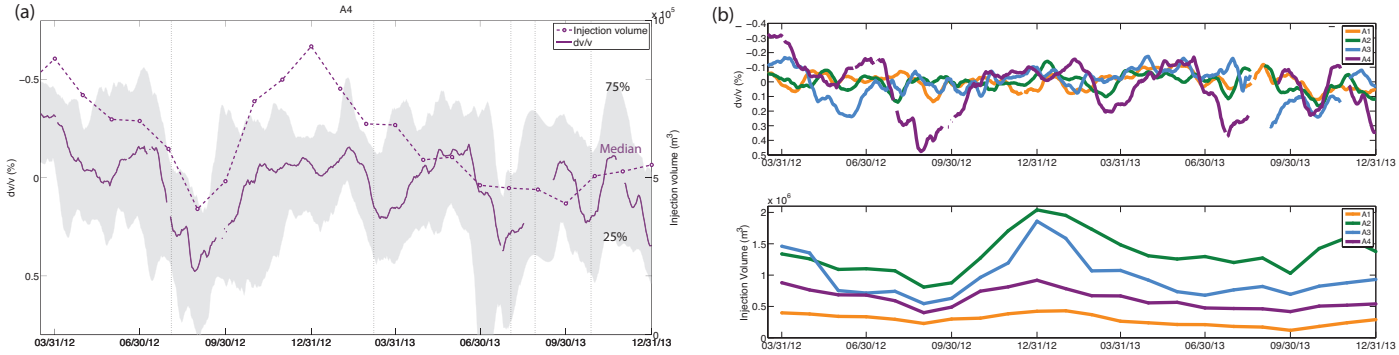

Figure 2.17.2: (a) Graph shows the strong correlation between median dv/v and injection volume over ~21 months at Area 4 (A4). Gray shade shows the interquartile range of the daily dv/v measurement. Dashed lines indicates the onset times of the *M* 3+ eartquakes that occurred at Area 4. Note that the y-axis for dv/v is reversed. (b) This graph shows (top) the dv/v measurement for all areas compared to (bottom) their respective monthly injection volume. The gaps seen in lines are due to data unavailability.

Results

The dv/v value for each area, namely A1, A2, A3 and A4 (see Figure 2.17.1), is estimated by taking the median of all the dv/v values obtained from each station pair within the marked area. Taking the median enhances the signal from a few common sources, which have effects that have spatial extent such as large earthquakes and fluid diffusion. This approach also minimizes the effect from outlier measurements and possible effects from non-homogenous noise sources as the station pairs used span a wide range of azimuths.

Our result shows there is a strong anti-correlation (R = -0.61) between dv/v and fluid injection volume at Area A4 (Figure 2.17.2). The correlation value with injection volume diminishes in order of A4, A3, A2 and A1, from south to north across the reservoir (see Table 2.17.1).

Area	Correlation with Injection Volume	Total Injection volume (m3)	# of M3.0+ Earthquakes
A1	0.1356	6.8E+06	0
A2	-0.1147	3.1E+07	16
A3	-0.3500	2.2E+07	10
A4	-0.6109	1.4E+07	5

Table 1. Table shows overall correlation value of the dv/v measurement with injection volume and the number of M3.0+ earthquakes during the study period for each enclosed area.

Discussion

The strong negative correlation between dv/v and fluid injection volume at Area 4 may be showing the effect of fluid where an increase in injection volume introduces more fluid diffusing throughout the area, which reduces the shear modulus and in turn, the shear velocity.

The varying correlation values across different areas may result from earthquakes, which damage the structure and affect the dv/v measurement. This effect is most pronounced at Area 2 and Area 3 where there were few *M*4.0+ earthquakes during the study period (see Figure 2.17.1).

In addition, Area A4 has a lower injection volume (1.4 x 10^7 m^3) compared to A2 and A3, yet shows the highest correlation between dv/v and injection volume. It seems counterintuitive, as higher injection volume would reduce the shear modulus further. This observation may reflect the heterogeneity of structure across the Geysers, where there are different fluid saturation and permeability for each region, affecting how the injected fluid diffuses throughout the region and changes the shear modulus.

Our result indicates the potential of using ambient noise as independent observational data to retrieve information on temporal seismic velocity changes at geothermal areas. This information can be used to understand the change in the stress field and ultimately, the geomechanical status of the reservoir due to geothermal operations.

Acknowledgements

This work is funded by the National Science Foundation under the award number NSF, EAR-1053211. We also thank Roland Gritto and Avinash Nayak for their insightful discussion. Waveform data, metadata, or data products for this study were accessed through the Northern California Earthquake Data Center (NCEDC), doi:10.7932/NCEDC.

References

Brenguier, F., Campillo, M., Hadziioannou, C., Shapiro, N. M., Nadeau, R. M., & Larose, E., Postseismic relaxation along the San Andreas fault at Parkfield from continuous seismological observations, *Science*, 321(5895), 1478-1481, 2008.

Brenguier, F., Shapiro, N. M., Campillo, M., Ferrazzini, V., Duputel, Z., Coutant, O., & Nercessian, A., Towards forecasting volcanic eruptions using seismic noise, *Nature Geoscience*, 1(2), 126-130, 2008.

Seats, K. J., Lawrence, J. F., & Prieto, G. A., Improved ambient noise correlation functions using Welch's method, *Geophysical Journal International*, 188(2), 513-523, 2012.

Shapiro, N. M., Campillo, M., Stehly, L., & Ritzwoller, M. H., High-resolution surface-wave tomography from ambient seismic noise,*Science*, 307(5715), 1615-1618, 2005.

Wegler, U., Nakahara, H., Sens-Schönfelder, C., Korn, M., & Shiomi, K., Sudden drop of seismic velocity after the 2004 Mw 6.6 mid-Niigata earthquake, Japan, observed with Passive Image Interferometry, *Journal of Geophysical Research: Solid Earth* (1978–2012), 114(B6), 2009.

18 Hydrologic Modulation of Seismicity in Western China 1991–2013

Noah Randolph-Flagg, Jesse Day, Roland Bürgmann, Michael Manga

Introduction

Deep drilling projects and induced seismicity suggest that much of the earth's crust—even deep in continental interiors—is near critically stressed and prone to fail after small (<1 MPa) stress changes (*e.g., Zoback and Harjes,* 1997). It has been suggested that stresses due to hydrologic loading from rain and snow (*e.g., Heki*, 2003), changes in pore fluid pressure (*e.g., Hainzl et al., 2006)*, solid earth tides (*e.g., Knott, 1897)*, and thermally induced stresses due to thermal expansion (*e.g., Hainzl et al., 2013)* may produce stresses sufficient to generate earthquakes. Because many of these stresses are periodic or quasi-periodic, periodicity in seismicity may be widespread and provide insight into how earthquakes nucleate.

Periodic modulation of earthquakes has been observed in the High Himalaya in Nepal (*Bollinger et al*., 2007; *Bettinelli et al*., 2008; *Ader and Avouac*, 2013), the San Andreas fault near Parkfield, CA (*Christiansen et al.*, 2007; *Ben-Zion and Allam*, 2013; *Amos et al.,* 2014), Mt. Hochstaufen in Germany (*Hainzl, 2006; 2013*), mountains in Japan (*Heki*, 2003), and some hydrothermal systems (*Saar and Manga*, 2003; *Christiansen et al.*, 2005; *Braunmiller et al.*, 2013, *Rydelek et al.*, 1988; *Gao et al.*, 2000; *Wilcock*, 2001.) Unlike past studies which focused on seismicity over small areas, we examine apparently similar modulation in seismicity from 1991–2013 throughout an ~100,000 km^2 area including the Tibetan Plateau, Altyn Tagh, Tarim Basin, and Tien Shan. This diversity of tectonic and climatic setting allows us to assess different mechanisms and statistical tests.

Data

We analyze earthquakes between 20° and 60° N and between 105° and 70° E from two catalogs: the Annual Bulletin of Chinese Earthquakes (ABCE) 1991 to 2005 (n=22,513) and the China Earthquake Networks Center Catalog (CENC) 2006 to 2013 (n=5,162.) We also compare background seismicity in the ABCE catalog to repeating earthquakes in the ABCE catalog (n=2,379) as identified by *Schaff and Richards* (2011). Using the Gutenberg-Richter relationship between earthquake occurrence and magnitude we assess catalog completeness for 1991-2005 and 2009–2013 after the 2008 M_w 7.9 Wenchuan earthquake and aftershock sequence. Although both seismic catalogs are incomplete for $M_w < 5$ the catalog completeness does not change seasonally, meaning that the seasonal modulation we observe is not simply due changes in station coverage and, therefore, both catalogs are used in whole.

We use three methods to see if the seasonal modulation is observable in background seismicity or only in foreshocks and aftershocks. First, we compare seismicity to a global catalog of $M_w > 8$ and a local catalog of $M_w > 7$. We also test two declustering methods. The Reasenberg (1985) method identifies the likelihood that earthquakes are related in a spatial-temporal window based on Omori's Law. In contrast the stochastic epidemic-type aftershock sequence (ETAS) declustering method of *Zhuang et al.* (2002) calculates the likelihood that each earthquake is a background event.

Results and Discussion

Seismicity in the Tibetan Plateau and surrounding areas suggests seasonal modulation (Figure 2.18.1). This seasonality is only visible in the shallowest earthquakes (< 5 km) making hydrologic loading, pore fluid pressure changes, and thermal elastic expansion all plausible causes (Figure 2.18.2).

We use three tests to quantify the statistical significance of the seasonal modulation. The most common test, the Schuster test (*Schuster*, 1897), calculates a p-value for one frequency at a time comparing the observed correlation with the likelihood of the correlation appearing wholly by chance. We also use a novel multi-frequential approach (*Dutilleul*, 2001), which finds the frequencies that add together to best fit the time series. This approach could allow us to identify different mechanisms as different frequencies. Finally, we use a simple analysis of variance test (ANOVA), which calculates the statistical difference between the mean seismicity of different seasons. All of these approaches show statistically significant ~12 month periods for both declustered and complete catalogs. The phase of this period varies spatially (Figure 2.18.1b and c) and the amplitude changes significantly year to year.

We show that loading on either side of the Plateau is significant (Figure 2.18.1a) and that seismicity correlates with peak hydrological loading determined from GRACE gravity-change measurements (Figure 2.18.1b and c). If surface loading is the primary mechanism for modulating seismicity, it should suppress thrust and strike-slip faulting and therefore negatively correlate with nearby seismicity. In contrast, if normal faults dominate or if pore fluid pressures rather than loading modulate seismicity, nearby seismicity will positively correlate with GRACE data. In the future we hope to further explore the spatial variation in seasonality and fault type and compare the potential contributions of earth tides, pore fluid pressures, and thermoelastic expansion.

Acknowledgements

The first author has been supported in this research by a Fulbright Research Fellowship in China and an NSF Graduate Research Fellowship. We are grateful to Chris Johnson (BSL) and Prof. Pierre Dutilleul (McGill) for help with statistics.

References

Ader, T., Avouac, J., Detecting periodicities and declustering in earthquake catalogs using the Schuster spectrum, application to Himalayan seismicity, *Earth and Planetary Science Letters*, 908-34, 2013.

Amos, C. B., P. Audet, W. C. Hammond, R. Bürgmann, I. A. Johanson, and G. Blewitt, Contemporary uplift and seismicity in central California driven by groundwater depletion, *Nature*, v. 509, 2014.

Ben-Zion, Y, Allam, A.A. Seasonal Thermoelastic Strain and

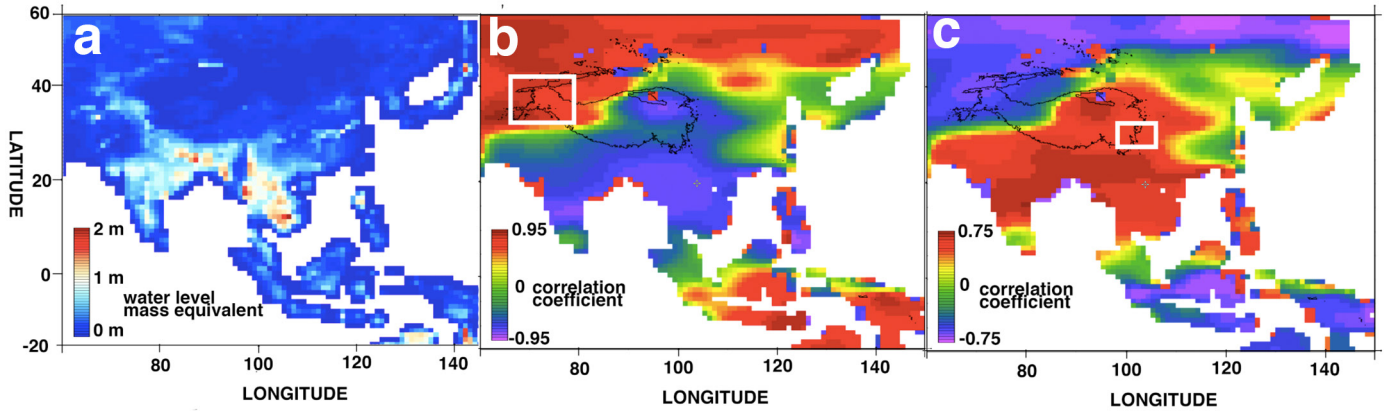

Figure 2.18.1a: Map of average annual change in mass storage in water equivalent thickness from GRACE satellites (http://grace.jpl.nasa.gov/data/). This shows over 1 m of annual loading along the foot of the Himalaya and almost 1 m along the western and northern edge of the Tibetan Plateau; b and c) Map of correlation coefficient comparing the monthly earthquake time series (1991–2005) in the white boxes to monthly GRACE loading data (2002–2013.) b shows the region where peak water storage in the fall corresponds with peak seismicity in the fall while c) shows where peak water storage in the spring corresponds with peak seismicity in the spring.

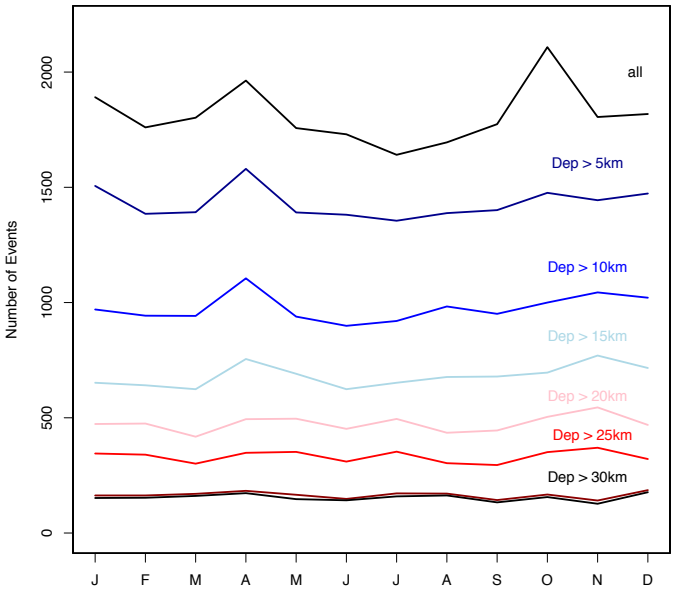

Figure 2.18.2: Cumulative monthly seismicity for different depths. Seaonal modulation is strongest at shallow depths.

Postseismic Effects in Parkfield Borehole Dilatometers, *Earth and Planetary Science Letters.*

Bettinelli, P., Avouac, J.-P., Flouzat, M., Bollinger, L., Ramillien, G., Rajaure, S., Sapkota, S., Seasonal variations of seismicity and geodetic strain in the Himalaya induced by surface hydrology. *Earth and Planetary Science Letters v.* 266, 332, 2008.

Bollinger, L., Perrier, F., Avouac, J.-P., Sapkota, S., Gautam, U., D.R., Tiwari, Seasonal modulation of seismicity in the Himalaya of Nepal. *Geophysical Research Letters v.* 34, 2007.

Braunmiller, J. , Nabelek, J, Trehu, A., A seasonally modulated earthquake swarm near Maupin, Oregon, *Geophys. J. Int., 2014.*

Christiansen, L, Hurwitz, S, Saar, M, Ingebritsen, S, Annual modulation of seismicity along the San Andreas Fault near Parkfield, CA, *Geophysical Research Letters, v.* 34, 2007.

Christiansen, L.B., S. Hurwitz, M.O. Saar, S.E. Ingebritsen, and P.A. Hsieh, Seasonal seismicity at western United States volcanic centers, *Earth Planetary Science Letters,* 240, 307-321, 2005.

Dutilleul, P., Multi-frequential periodogram analysis and the detection of periodic components in time series. *Communications in Statistics-Theory and Methods* v. 30, 2001.

Gao, S.S., Silver, PG, Linde, A.T. Sacks, I.S., Annual modulation of triggered seismicity following the 1992 Landers earthquake in California, *Nature*, 406, 2000.

Hainzl, S., T. Kraft, J. Wassermann, H. Igel, and E. Schmedes, Evidence for rainfall triggered earthquake activity, *GRL.* v 33, 2006.

Hainzl, S., Y. Ben-Zion, C. Cattania, and J. Wassermann, Testing atmospheric and tidal earthquake triggering at Mt. Hochstaufen, Germany, *Journal of Geophysical Res. v.* 118, 2013.

Heki, K., 2003, Snow load and seasonal variation of earthquake occurrence in Japan, *Earth Planet. Sci. Lett.*, 207, 159–164, 2003.

Knott, C., On Lunar Periodicities in Earthquake Frequency. *Proceedings of the Royal Society of London* 60, 457, 1897.

Reasenberg, P., Second-Order Moment of Central California Seismicity, 1969-1982. *Journal. Geophysical Research* v. 90, 1985.

Saar, M.O., and Manga, M., Seismicity induced by seasonal groundwater recharge at Mt. Hood, Oregon, *Earth Plan. Sci. L.,* v 214, 2003.

Schaff, D., and Richards, P., On finding and using repeating seismic events in and near China, *J of Geophysical Research*, v. 116, 2011.

Schuster, A., On Lunar and Solar Periodicities of Earthquakes. *Proceedings of the Royal Society of London* v. 61, 455, 1897.

Zoback, M., Harjes, HP, Injection-induced earthquakes and crustal stress at 9 km depth at the KTB deep drilling site, Germany, *Journal of Geophysical Research*, v. 102, 1997.

19 Comparison of Hydrological Responses to the Wenchuan and Lushan Earthquake

Zheming Shi, Michael Manga, Chi-Yuen Wang

Introduction

Earthquake-induced hydrological changes have been documented for thousands of years. These include: liquefaction, formation of new springs, disappearance of previous active springs, changes in stream and spring discharge, changes in the properties of groundwater such as geochemistry, temperature and changes in the activities of mud volcanoes and geysers (*Manga and Wang*, 2007). Understanding the origin of hydrological response may provide unique insight into the interaction between hydrogeologic and tectonic processes at scales in space and time that may help us understand the long term evolution of groundwater flows. However, instrumental records of these changes have become available only in the last several decades. And many of the previous studies use water level data from wells constructed in unconsolidated sediments (*Roeloffs*, 1998; *Wang*, 2001), only a few studies are based on measurements in hard rocks. Furthermore, identifying the dominant mechanism(s) for observed responses is often difficult because observations are limited to a single earthquake. Comparison of responses to multiple earthquakes with similar focal mechanisms occurring on the same fault zone may thus be useful for testing hypotheses. An ideal case is provided by the occurrence of the large (M_w6.6) Lushan earthquake on April 20, 2013, in Sichuan, China, nearly five years after the devastating M_w7.9 Wenchuan earthquake. The two earthquakes have the same thrust focal mechanism (Figure 2.19.1) and occurred on the same fault (the Longmenshan fault). Both earthquakes caused large hydrological changes. The similarity of focal mechanisms and the abundance of hydrological responses provide an excellent opportunity for testing the proposed mechanisms for hydrological responses. Here, we report the documented co-seismic hydrological changes following the two earthquakes. We then analyze and compare the co-seismic response, which allows us to assess mechanisms responsible for the hydrological changes.

Data and Analysis

Groundwater level and liquefaction data were collected after the two earthquakes in the near- to intermediate-field. In total, 12 groundwater wells were selected, with epicenter distances between 95 to 525 km to the Wenchuan epicenter and 29 to 442 km to the Lushan epicenter (Figure 2.19.1). Water level declined in wells on both sides of the Longmenshan fault (#1, #2, #4) and Huayingshan fault (#6, #7, #8, and #9), which is parallel to the Longmenshan fault. Water levels rose in wells along the strike of the Longmenshan fault, #3, #5, #11 and #12. For the Lushan earthquake, 9 of the 12 wells show co-seismic water level changes. Wells #1, #2 and #12 show no co-seismic changes in water level. Comparing the water level changes for the two earthquakes, only wells #3, #4,#5, #6, and #7 show the same sign of co-seismic changes, while wells #8, #9, and #11 have opposite sign of water level changes. Well #10, which did not respond to the Wenchuan earthquake, showed a rise in water level following the Lushan earthquake. There is no clear relationship with the epicenter distance or the response amplitude, both in the near-field and in the intermediate-field (*Shi et al.*, 2014).

Widespread liquefaction phenomena occurred in the Sichuan basin, covering an area 500 km in length and 200 km in width (Figure 2.19.1). For the Lushan earthquake, on the other hand, liquefaction only occurred near river terraces and alluvial flats along the Shuangshi-Dachuan fault, and the reported liquefaction phenomena occurred within 20 km of the epicenter (reported by Institute of Geology, CEA).The maximum distance from the epicenter of the major liquefaction features for the Wenchuan earthquake is about 210 km, about 10 times greater than the maximum distance of liquefaction for the Lushan earthquake. Using an empirical scaling relation from *Wang* (2007), we find that the minimum seismic energy density to trigger liquefaction in the Wenchuan earthquake is about 1.4 J/m^3, but is 20 times greater (~30 J/m^3) in the Lushan earthquake.

Mechanisms of the Hydrological Responses

Two mechanisms are usually used to explain water level changes in the consolidated rock: (1) Co-seismic static strain; (2) Permeability enhancement. We begin by evaluating the mechanism of co-seismic static strain by comparing the observed water level changes with those predicted by the dislocation model. Only the directions of changes in water level are consistent with the strain field in Wenchuan earthquake, and the predicted magnitudes of co-seismic water level changes are much smaller than was observed in both earthquakes. This indicates that the co-seismic strain model may not be the dominant mechanism causing water level changes both in near- and intermediate-field. However, the mechanism of permeability changes maybe responsible for the water level changes. The mechanism of permeability enhancement predicts a statistically random sign of the water level changes if a sufficiently large number of observations are available (*Wang and Chia*, 2008), consistent with our data. The analyses of tidal response to the Wenchuan earthquake in some near-field wells also show permeability enhancement following the Wenchuan earthquake (*Lai et al.*, 2013). Thus the hypothesis of permeability changes induced by dynamic stress produced by seismic waves may be valid not only in the intermediate-field, but also in the near-field. The maximum distance to liquefaction sites for the Wenchuan earthquake is about 10 times larger than Lushan earthquake, while the minimum seismic energy density required to trigger liquefaction is only 1/20 of that in the latter. This suggests either that the occurrence of liquefaction is more sensitive to low seismic frequencies or that the Wenchuan earthquake changed the sensitivity of unconsolidated materials, and properties had not completely recovered during the five year interval between the two earthquakes.

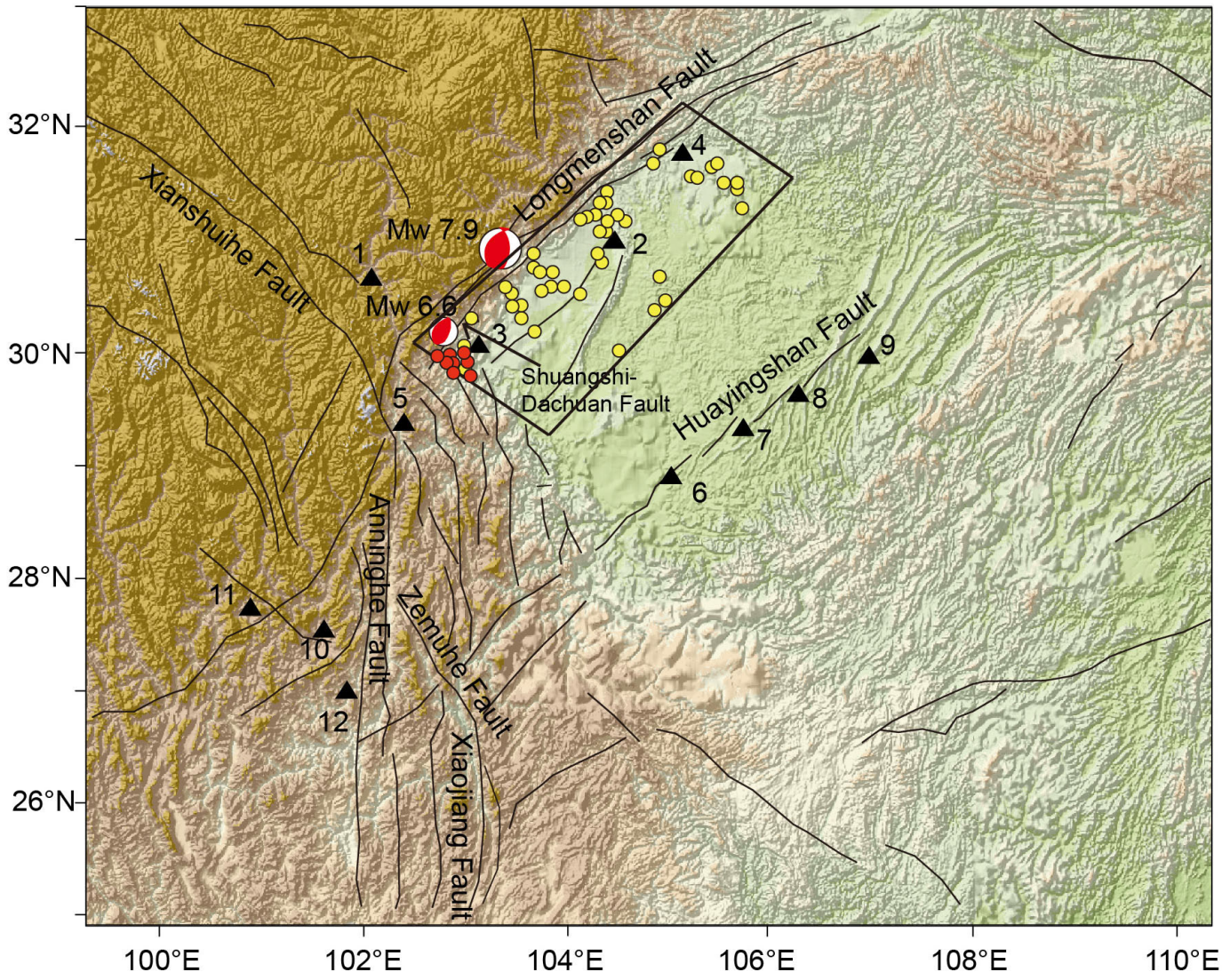

Figure 2.19.1: Geological setting, locations of groundwater monitoring wells (blue triangles) and epicenters of the Wenchuan (M_w 7.9) and the Lushan (M_w 6.6) earthquakes. Beach balls show the low hemisphere projection of the focal mechanism. The red lines represent faults. The yellow and red circles express the liquefaction phenomena that occurred following the Wenchuan and Lushan earthquake, respectively.

Acknowledgements

This research is supported by the US National Science Foundation. Zheming thanks the financial support from the China Scholarship Council.

References

Manga, M., Wang, C-Y., Earthquake hydrology In: Treatise on geophysics (ed. G S). Amsterdam, *Elsevier*, *4*, 293-320, 2007.

Lai, G. J., Ge, H. K., Xue, L., Brodsky, E. E., Huang, F. Q., Wang, W. L., Tidal response variation and recovery following the Wenchuan earthquake from water level data of multiple wells in the near field. *Tectonophysics*, *619-620*, 115-122, 2014.

Roeloffs, E. A., Persistent water level changes in a well near Parkfield, California, due to local and distant earthquake. *Journal of Geophysical Research*, *103*, 868-889, 1998.

Shi, Z. M., Wang, G. C., Wang, C-Y., Manga, M., Liu, C. L. Comparison of hydrological responses to the Wenchuan and Lushan earthquakes. *Earth and Planetary Science Letters*, *391*, 193-200, 2014.

Wang C-Y.,Coseismic hydrologic response of an alluvial fan to the 1999 Chi-Chi earthquake, Taiwan. *Geology*, *29*,831-834.2001.

Wang C-Y.,Liquefaction beyond the Near Field. *Seismological Research Letters*, *78*,512-517, 2007.

Wang C-Y & Chia Y., Mechanism of water level changes during earthquakes: Near field versus intermediate field. *Geophysical Research Letters*, *35*,L12402, 2008.

20 Establishing the Magnitude Threshold of Dynamically Triggered Earthquakes

Christopher W. Johnson and Roland Bürgmann

Introduction

The relationship between stress perturbations and the advancement or suppression of future earthquakes is an ongoing area of research in active tectonics. Studies of earthquake triggering provide insight into the state of stress on a fault and the conditions prior to and during an earthquake nucleation sequence. Static triggering results from the elastic deformation and stress changes due to slip on a fault during an earthquake. In the near-field, a static stress transfer of ~0.1 MPa has been shown to influence regional earthquake activity by promoting or suppressing earthquakes (*Stein*, 1999). In the far-field; *i.e.*, at distances where static stress changes are negligible, studies of dynamic triggering examine the effects of a stress pulse on critically stressed faults and the subsequent change in seismic activity (*Freed*, 2005). Dynamic triggering refers to changes in earthquake activity due to the transient stress perturbation during the passage of seismic waves. Separating the effects of static vs. dynamic stress changes is necessary to advance the understanding of global earthquake interaction (*Felzer and Brodsky*, 2005; *Richards-Dinger et al.*, 2010; *van der Elst and Brodsky*, 2010) and requires investigating seismicity more than 2–3 rupture lengths from the mainshock.

Beyond the traditional aftershock zone, the largest transient stress perturbation from a remote earthquake occurs during the passage of the surface waves. Surface waves are capable of instantly triggering low magnitude earthquakes (M<5), as well as non-volcanic tremor, and sometimes increasing activity in the subsequent days to weeks after the seismic waves have passed (*Hill et al.*, 1993; *Pankow et al.*, 2004). Rarely observed is the immediate triggering of M>5.0 earthquakes beyond the aftershock zone (*Parsons and Velasco*, 2011), which suggests that larger-magnitude events are not susceptible to transient stress changes (*Parsons et al.*, 2012). Recent observations of large magnitude earthquakes (M>8) promoting M>5.5 aftershocks in the far-field has prompted seismologists to continue the investigation into dynamic stresses and the relationship to earthquake nucleation (*Gomberg and Sherrod*, 2014; *Pollitz et al.*, 2012).

In this study we examine global seismicity of M≥5.5 events in the months following the passage of large-amplitude surface waves in regions beyond the aftershock zone. Our goal is to investigate the triggering potential of M≥7.5 and a possible threshold for triggering M>5.5 events. This study develops a systematic method that examines all M>7.5 events in 35 years using the Global Centroid Moment Tensor catalog (http://www.globalcmt.org/) establishing global earthquake rates following the largest events. The techniques of this study allow us to characterize enhanced or suppressed activity following a stress perturbation and to consider the activity related to different fault mechanisms of either mainshocks or trigger candidates.

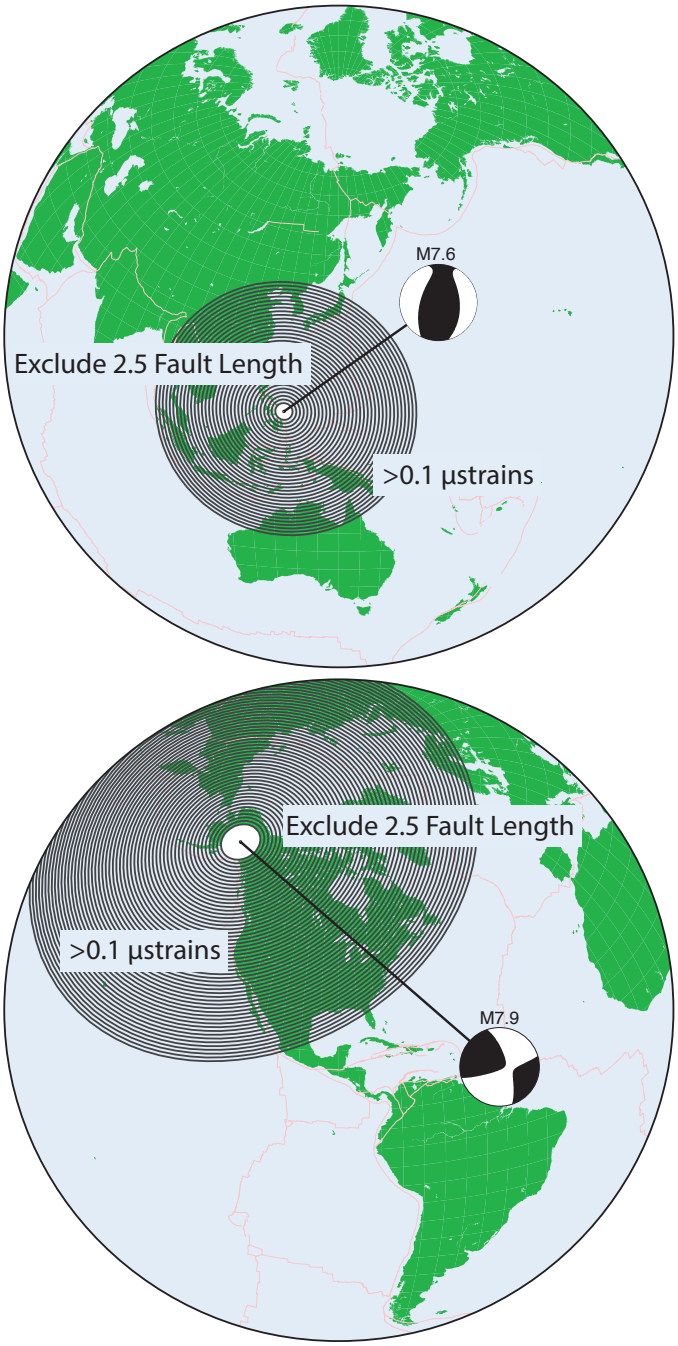

Figure 2.20.1: The region of elevated strain is indicated in the figure for two separate mainshocks. The importance of scaling the magnitudes is shown by the extent of large-amplitude surface waves for two events that cover very different regions of the globe. Shaded regions indicate the area for event selection before and after each mainshock. The exclusion zone is a radial region spanning 2.5 fault lengths from the mainshock and is shown in white. The distal limit is scaled to the magnitude using the estimated seismic wave amplitude relative to the maximum strain threshold. The top figure indicates the region for a M7.6, with an exclusion zone of 230 km and selecting events out to a radial distance of 3600 km. The bottom figure is showing a M7.9, with an exclusion zone of 500 km and selecting all events to a radial distance of 5900km.

Summary

This study incorporates only far-field seismic activity following $M \geq 7.5$ mainshocks using all $M \geq 5.5$ events in the catalog. Our method builds on the results by *Parsons and Velasco* (2011) that indicate no increase in $5 < M < 7$ events following $M \geq 7$ mainshocks beyond 1000 km. We study the triggering potential by separating $M \geq 7.5$ mainshocks by fault mechanism and develop a rate curve using a two-day moving average. The rate curve for each mainshock is then stacked and normalized by the total number of mainshocks. Our method is scaled spatially, using a region of elevated strain that is unique to each mainshock and determined using empirical wave amplitudes (Figure 2.20.1). This allows us to consider only far-field activity occurring in regions that are dynamically strained during the passage of seismic waves. We adopt a threshold of ≥0.1 μstrains that is previously shown to trigger activity in seismically active areas (*Peng et al.*, 2010; *Pollitz et al.*, 2012; *van der Elst and Brodsky*, 2010) to define the region of interest in this study.

The results shown in Figure 2.20.2 represent the stacked rate curves for four $M \geq 8.0$ strike-slip events. This curve excludes the 2012 $M8.6$ east-Indian Ocean event that produced a 10 day increase in global earthquake activity of $M \geq 5.5$ events (*Pollitz et al.*, 2012). We remove the event, which is also the largest strike-slip event on record, in order to establish the triggering potential of other large-magnitude strike-slip earthquakes. A rate increase above the 95% confidence interval is observed following time zero but additional pulses of activity are present at other points in time. Using this approach, we are continuing to examine far-field earthquake activity for different mechanisms and magnitude thresholds. The initial findings indicate that dynamic triggering of $M \geq 5.5$ events is only observed following the very largest; *i.e.*, $M \geq 8.5$, earthquakes on record.

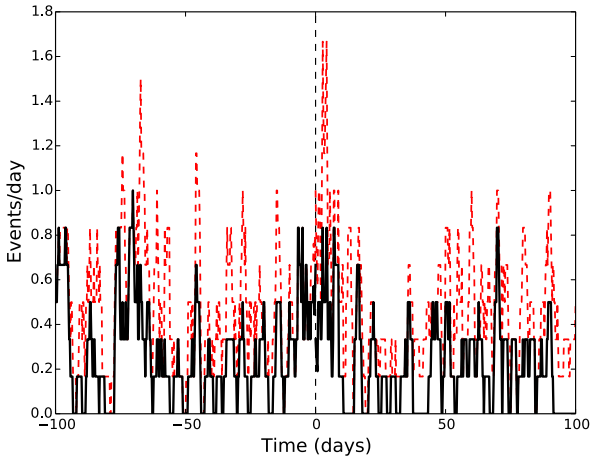

Figure 2.20.2: The rate curve shown is determined using four $M \geq 8.0$ strike-slip earthquakes between 1977–2012 for ±100 days. Time zero is relative to the mainshock origin time and the events per day is normalized by the total number of mainshocks. The red rate curve includes the $M8.6$ 2012 east-Indian Ocean that *Pollitz et al.* (2012) find to excite global activity in the 10 days following the event. The black curve omits the $M8.6$ events and does not indicate a strong pulse of activity after the mainshock. This initial result indicates that triggering of $M \geq 5.5$ events is only observed following the largest evetns on record.

Acknowledgements

This material is based upon work supported by the National Science Foundation Graduate Research Fellowship under Grant No DGE 1106400 for C.W. Johnson.

References

Felzer, K. R., and E. E. Brodsky, Testing the stress shadow hypothesis, *Journal of Geophysical Research*, *110*(B5), 2005.

Freed, A. M., Earthquake Triggering by Static, Dynamic, and Postseismic Stress Transfer, *Annual Review of Earth and Planetary Sciences*, *33*(1), 335-367, 2005.

Gomberg, J., and B. Sherrod, Crustal earthquake triggering by modern great earthquakes on subduction zone thrusts, *Journal of Geophysical Research: Solid Earth*, 2012JB009826, 2014.

Hill, D. P., et al., Seismicity Remotely Triggered by the Magnitude 7.3 Landers, California, Earthquake, *Science*, *260*(5114), 1617-1623, 1993.

Pankow, K. L., W. J. Arabasz, J. C. Pechmann, and S. J. Nava, Triggered Seismicity in Utah from the 3 November 2002 Denali Fault Earthquake, *Bulletin of the Seismological Society of America*, *94*(6B), S332–S347, 2004.

Parsons, T., and A. A. Velasco, Absence of remotely triggered large earthquakes beyond the mainshock region, *Nature Geoscience*, *4*(5), 312-316, 2011.

Parsons, T., J. O. Kaven, A. A. Velasco, and H. Gonzalez-Huizar, Unraveling the apparent magnitude threshold of remote earthquake triggering using full wavefield surface wave simulation, *Geochemistry, Geophysics, Geosystems*, *13*(6), 2012.

Peng, Z., D. P. Hill, D. R. Shelly, and C. Aiken, Remotely triggered microearthquakes and tremor in central California following the 2010Mw8.8 Chile earthquake, *Geophysical Research Letters*, *37*(24), 2010.

Pollitz, F. F., R. S. Stein, V. Sevilgen, and R. Burgmann, The 11 April 2012 east Indian Ocean earthquake triggered large aftershocks worldwide, *Nature*, *490*(7419), 250-253, 2012.

Richards-Dinger, K., R. S. Stein, and S. Toda, Decay of aftershock density with distance does not indicate triggering by dynamic stress, *Nature*, *467*(7315), 583-586, 2010.

Stein, R. S., The role of stress transfer in earthquake occurrence, *Nature*, *402*, 604-609, 1999.

van der Elst, N. J., and E. E. Brodsky, Connecting near-field and far-field earthquake triggering to dynamic strain, *Journal of Geophysical Research*, *115*(B7), 2010.

21 Evidence For a Triggered Foreshock Sequence Prior to the 2012 M7.0 Baja, CA Earthquake

Christopher W. Johnson and Roland Bürgmann

Introduction

The timing of earthquake nucleation processes and the initiation of slip on a fault is an ongoing area of research in active tectonics. Slip occurs on critically stressed faults when the accumulation of elastic stress exceeds the frictional strength. The effect of transient stress perturbations and their correlation with increased seismic activity can be studied through observations of dynamically triggered earthquakes induced by the passage of long-period surface waves (*Brodsky and van der Elst*, 2014). Previous studies conclude that surface waves are capable of instantly triggering low-magnitude earthquakes (M<5), as well as non-volcanic tremor, and sometimes results in increased activity in the subsequent days to weeks after the seismic waves have passed (*Gomberg et al.*, 2004; *Hill et al.*, 1993; *Peng et al.*, 2010). The absence of M>5.0 dynamically triggered earthquakes in these observations appears to suggest that these larger events are not susceptible to transient stress changes (*Parsons et al.*, 2012). This finding would negate a 'normal' Gutenberg-Richter scaling relationship for dynamically triggered earthquakes, if only low magnitude events are triggered by transient stresses.

On April 11, 2012 a complex intraplate seismic sequence occurred in the east Indian Ocean offshore from Sumatra resulting in a M8.6 event that ruptured 500 km on a series of conjugate faults and is the largest strike-slip event recorded with modern instrumentation (*Meng et al.*, 2012). No tsunami or massive destruction occurred but the global rate of large magnitude events (M>5.5) significantly increased for 10-days (*Pollitz et al.*, 2012). The triggered events were located in the regions of highest transient stains during the surface wave train (*Pollitz et al.*, 2012). This study is interested in the local activity preceding and following the M8.6 east-Indian Ocean earthquake near the nucleation site of some of the dynamically triggered M>5.5 earthquakes. This initial study focuses on the M7.0 event that occurred in the Gulf of California, Baja, California, Mexico (BC). The BC earthquake sequence consists of a M6.0 followed nine minutes later by a M7.0 and was preceded by the passage of surface waves from three remote large events. Our goal is to establish a record of activity around the time of the transient stress perturbation.

Data and Methods

The data used for this study are earthquake catalogs and seismic waveforms. The catalog data was obtained from the Servicio Sismológico Nacional de Mexico (SSN). As reported by *Pollitz et al.* (2012), no precursory increase in local activity is observed in the SSN catalog in the months prior to the M7.0 (Figure 2.21.1). To enhance the catalog record we utilize data recorded by a broadband network operated by Centro de Investigación Científica y de Educación Superior de Ensenada (CICESE). We obtained waveform records from April 5–15, 2012 for the analysis. The seismometers chosen are restricted to the stations nearest to the M7.0 event and we focus on the low magnitude events not contained in the catalog. The waveform data was analyzed for unreported earthquakes using a matched filter detection technique during the seven days before the M7.0 (*van der Elst et al.*, 2013). The templates were selected from the aftershocks and by visual inspection of the daily records preceding the M7.0 for unreported events. We observe 94 microseismic events in the period examined (Figure 2.21.2). Due to the limited observations of these small events, we estimate the location using the S-P arrival times and first motions. The magnitude is scale by amplitude and calibrated using aftershocks listed in the SSN catalog.

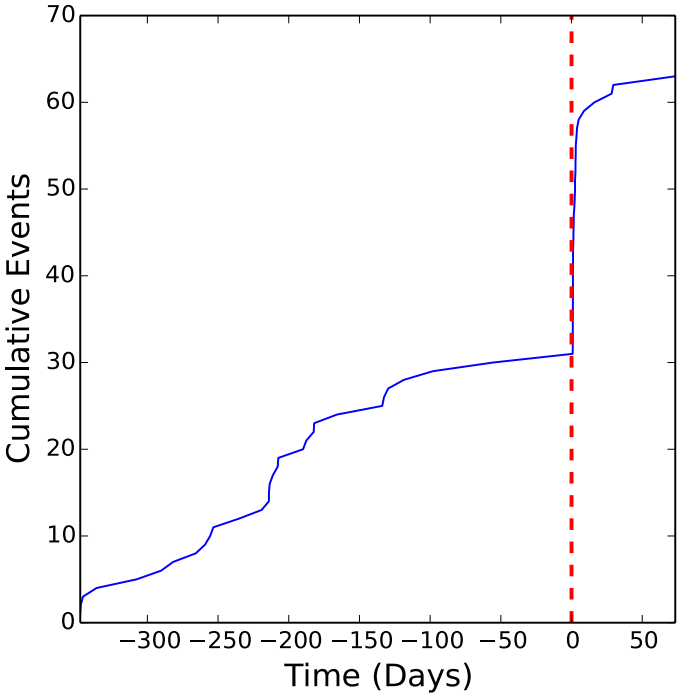

Figure 2.21.1: Gulf of California cumulative seismicity in the surrounding 300 km of the M7.0. Time zero is relative to the arrival of the M8.6 east Indian Ocean surface waves. The region is seismically quite prior to this event.

Summary

This effort did not produce evidence of immediate triggering during the passage of surface waves from the east-Indian Ocean earthquake. The BC analysis does reveal a cascade of microseismic events occurring six hours before the M7.0. The initiation of the foreshock sequence correlates in time with the passage of surface waves from a M6.7 earthquake located 1500 km SE in the Michoacán trench (Figure 2.21.3). The surface waves from the M8.6 east Indian Ocean and the M6.7 Michoácan earthquakes result in a dynamic stress perturbation of ~3 kPa and ~1 kPa, respectively. Stress changes of this order are shown

to excite tremor and microseismic events in geothermal regions and plate boundaries (*Peng et al.*, 2010).

The BC events are located on a transverse fault in a transtensional stress field along the North America—Pacific plate boundary. The initial interpretation is that the *M*6.0 and *M*7.0 earthquakes were dynamically triggered by teleseismic waves. The microseismic events are evident for six hours following the arrival of the Michoacán earthquake surface waves and cascade up to the cataloged foreshocks and the *M*7.0 event. The lack of microseismic activity initiating with the *M*8.6 east-Indian Ocean surface waves does not exclude the importance of this occurrence. The offshore location combined with the distance to the nearest station at ~45 km, with most observations only at the BAHB station, may not fully capture all the seismic activity on the fault. The amplitude and duration of the transient stress may have induced fluid migration or damaged frictional contacts along the fault which may promote eventual failure (*Brodsky*, 2003; *Parsons*, 2005). Additional observation of similar events using will be required to enhance the signal in future studies and resolve the changes in seismic activity prior to the nucleation of a potentially triggered large-magnitude event.

Acknowledgements

We thank R.C. Castro at CICESE for providing the RESBAN network seismic data. The catalog was obtained from SSN. This material is based upon work supported by the National Science Foundation Graduate Research Fellowship under Grant No DGE 1106400 for C.W. Johnson.

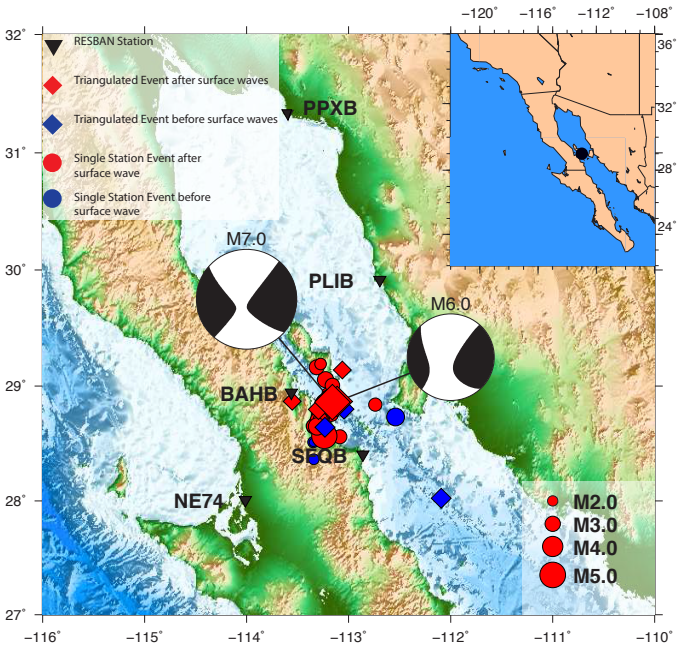

Figure 2.21.2: Map of Gulf of California indicating location of *M*6.0 and *M*7.0 events using http://www.globalcmt.org/ moment tensor solutions. Red and blue markers indicate the location of activity observed at the BAHB station. Additional stations are located >125 km from the area of activity with a low signal to noise ratio that limits observation of small events. Eight events were observed in the five days preceding the east Indian Ocean teleseismic surface waves (see Figure 2.21.3). No activity was observed during the first passage of the teleseismic surface waves.

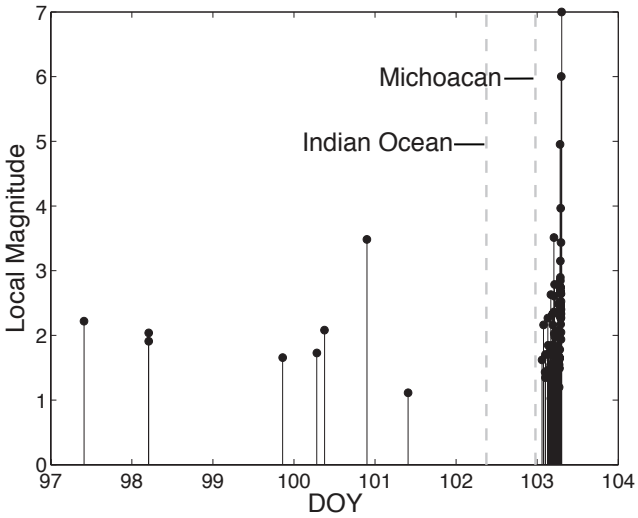

Figure 2.21.3: Local earthquakes with magnitude estimates observed before the *M*7.0 earthquake. The magnitude is calculated using a local magnitude method based on the maximum displacement for each event and calibrated with cataloged aftershocks. Gray lines indicate the surface waves arrival times of the east Indian Ocean (22 hours before *M*7.0) and Michoacán (6 hours before *M*7.0) earthquakes. No increase in activity is observed following the passage of the Indian Ocean surface waves. The increase is observed after the Michoacán, MX event located 1600 km to the southeast

References

Brodsky, E. E., A mechanism for sustained groundwater pressure changes induced by distant earthquakes, *Journal of Geophysical Research*, *108*(B8), 2003.

Brodsky, E. E., and N. J. van der Elst, The Uses of Dynamic Earthquake Triggering, *Annual Review of Earth and Planetary Sciences*, *42*(1), 317-339, 2014.

Gomberg, J., P. Bodin, K. Larson, and H. Dragert, Earthquake nucleation by transient deformations caused by the M=7.9 Denali, Alaska, earthquake, *Nature*, *427*(6975), 621-624, 2004.

Hill, D. P., et al., Seismicity Remotely Triggered by the Magnitude 7.3 Landers, California, Earthquake, *Science*, *260*(5114), 1617-1623, 1993.

Meng, L., J. P. Ampuero, J. Stock, Z. Duputel, Y. Luo, and V. C. Tsai, Earthquake in a maze: compressional rupture branching during the 2012 M(w) 8.6 Sumatra earthquake, *Science*, *337*(6095), 724-726, 2012.

Parsons, T., A hypothesis for delayed dynamic earthquake triggering, *Geophysical Research Letters*, *32*(4), 2005.

Parsons, T., J. O. Kaven, A. A. Velasco, and H. Gonzalez-Huizar, Unraveling the apparent magnitude threshold of remote earthquake triggering using full wavefield surface wave simulation, *Geochemistry, Geophysics, Geosystems*, *13*(6), 2012.

Peng, Z., D. P. Hill, D. R. Shelly, and C. Aiken, Remotely triggered microearthquakes and tremor in central California following the 2010 Mw 8.8 Chile earthquake, *Geophysical Research Letters*, *37*(24), 2010.

Pollitz, F. F., R. S. Stein, V. Sevilgen, and R. Burgmann, The 11 April 2012 east Indian Ocean earthquake triggered large aftershocks worldwide, *Nature*, *490*(7419), 250-253, 2012.

van der Elst, N. J., H. M. Savage, K. M. Keranen, and G. A. Abers, Enhanced remote earthquake triggering at fluid-injection sites in the midwestern United States, *Science*, *341*(6142), 164-167, 2013.

22 Repeating Earthquakes and Inferred Deep Slip on the Calaveras Fault

Robert M. Nadeau and Roland Bürgmann

Introduction

The Calaveras fault in the Eastern San Francisco Bay Area lies near major urban areas in the San Francisco Bay region, including San Jose, Fremont, and the cities of the San Ramon Valley corridor, and it has the potential to cause significant loss of life and property damage. Since 1850, there have been 13 earthquakes of M_L 5 or greater on or near the Calaveras fault. Monitoring of the fault with GPS, creepmeter, gravity, magnetic and seismic data suggests a connection to the Hayward fault with active creep along much of the fault trace. Investigation of the distribution of seismicity along the fault reveals that in regions where $M_L > 5$ earthquakes occur, little seismicity above M_L 1.4 is found and that pre-mainshock and aftershock microseismicity patterns are similar (*Oppenheimer et al.*, 1990). This spatial and temporal variability in creep and seismic behavior of the fault suggest that the situation at depth is significantly more complicated than a single locked/creeping region, leading to a time-dependent hazard for the Bay Area

Geodetic measurements of surface deformation provide information about the nature of elastic strain accumulation near seismogenic faults, their locking depth and slip rates, and variations of those parameters in space and time due to time-dependent processes. However, the inference of these properties on fault zones at depth requires various modeling assumptions that are sometimes not well constrained. A primary objective of this project is to help addresses the seismic potential and natural hazard presented by the Calaveras fault in the Eastern San Francisco Bay Area by providing additional constraints on the spatial and temporal distribution of inferred deep fault slip using repeating earthquakes.

Repeating Quakes on the Calaveras

Owing to their occurrence within the fault zone itself, repeating earthquakes provide more direct information on the geometry and time-variability of creep on faults at depth, and for the more complex situation expected within the deep Calaveras fault zone, the addition of repeating earthquake information should help constrain estimates of deep fault strain accumulation significantly. With this in mind, we compiled a catalog of characteristically repeating earthquakes (CREs) on the Calaveras fault over an ~ 29.5 year period along an ~85 km long fault section with spatio-temporal coverage that includes the hypocenters of the 1984 Morgan Hill M_w6.2 and 2007 Alum Rock M_w5.2 earthquakes (Figure 2.22.1).

Survey of Deep Slip Rate from Repeaters

One interesting feature of the spatial distribution of the repeating sequences is that a fairly large number occur on what *Manaker et al.* (2005) call the Alum Rock seismic trend just SW of the Alum Rock earthquake (ellipse in Figure 2.22.1). A survey view of the repeater inferred slip information for the entire study segment is shown in Figure 2.22.2. Between -10 to 15 km NW, an initially high and decreasing rate of accumulating slip beginning in 1984 corresponds to the post-seismic slip response of the Calaveras to the 1984 Morgan Hill *M*6.2 earthquake (hypocenter at 13 km NW). The Alum Rock trend of repeaters appears as the southwest splay between 20 to 30 km NW in map view. As this study progresses, it will be interesting to see what kind of slip behavior this and other secondary structures have. We will also look at a number of cross-sections of the relocated repeating and non-repeating seismicity stepping along the fault to further illuminate other structural discontinuities and how deep fault slip is partitioned on these structures.

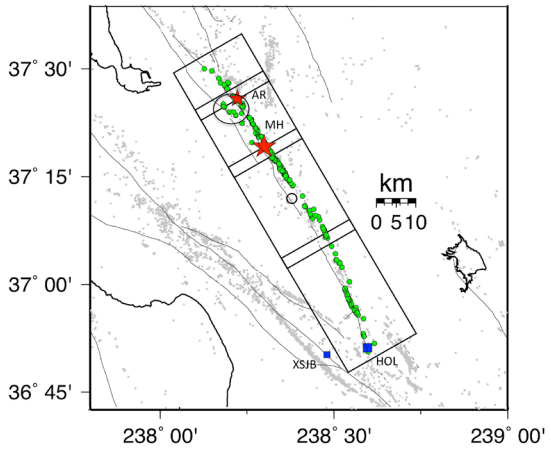

Figure 2.22.1. Locations of 236 repeating earthquake sequences (green/gray circles) identified in the Calaveras fault search area (boxes). 1024 repeated events belonging to these sequences were identifed between January 1, 1984 and May 31, 2013. Locations are based on the Double-Difference Real Time catalog (*Waldhauser and Schaff*, 2008; *Waldhauser*, 2009). Background seismicity > *M*2.0 are also shown (grey points). 2007 Alum Rock M_w5.2 and 1984 Morgan Hill M_w6.2 are stars labeled AR and MH, respectively. Hollister, CA and XSJB creep meter near San Juan Baustista, CA are squares labeled HOL and XSJB, respectively. Location of Alum Rock Seismic trend is indicated by ellipse containing AR location. The small open circle in center of search area corresponds to 0 km NW in Figure 2.22.2.

This information will also be combined with InSAR, GPS and other diverse geodetic datasets to provide improved constraints for a kinematic model of the variability of interseismic creep on the Calaveras fault. The goals of the modeling effort are to better delineate creeping zones on the Calaveras fault and their rates through time, to detect previously unknown transient slip events and to better characterize known events, such as postseismic slip following the 2007 Alum Rock earthquake.

Acknowledgements

Supported by the U.S. Geological Survey through award G13AP00035. Waveform data were provided by the Northern California Seismic System, USGS, Menlo Park by way of the

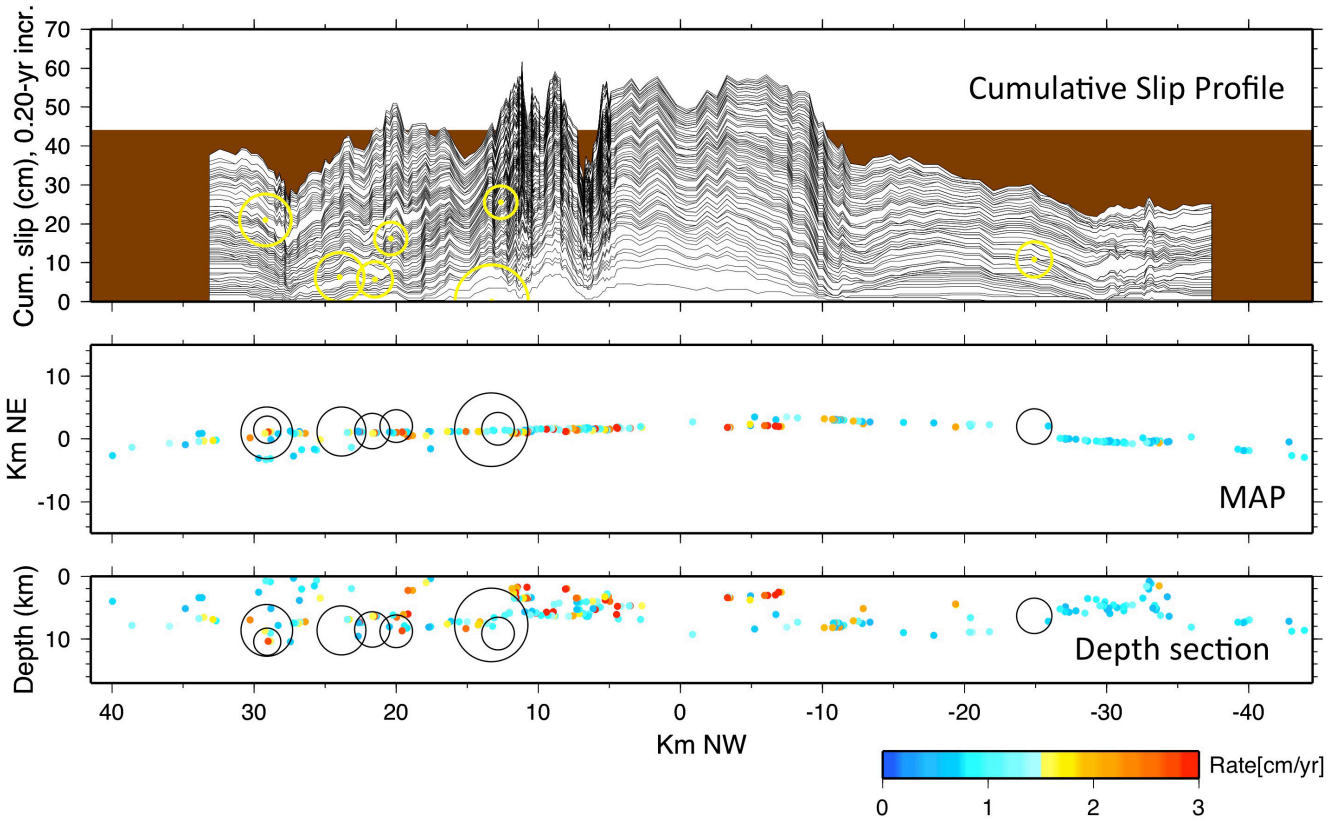

Figure 2.22.2: Top: Along fault, cumulative slip contours taken every 0.2 years since the beginning of 1984, smoothed over 15 sequences and stepped every 1 sequence along strike. The brown color shows the cumulative slip assuming a 1.5 cm/yr rate for the 29.414 year period. The yellow circles are M>4.5 earthquakes plotted at along fault locations and cumulative slip-time. Middle: Along fault locations of REQ sequences colored by average slip rate over the entire study period (scale at bottom). The Large black circles are M>4.5 events corresponding to the yellow circles at top. Bottom: Same as middle but in along fault depth section. The large circles located at 13 km NW in each panel corresponds to the 1984 Morgan Hill M6.2 earthquake hypocenter.

Northern California Earthquake Data Center (NCEDC) at the Berkeley Seismological Laboratory (BSL).

References

Waldhauser, F. and D.P. Schaff, Large-scale relocation of two decades of Northern California seismicity using cross-correlation and double-difference methods, *J. Geophys. Res., 113,* B08311, doi:10.1029/2007JB005479, 2008.

Manaker, D.M., Michael, A.J. and Burgmann, R., Subsurface structure and kinematics of the Calaveras-Hayward fault stepover from three-dimensional V-P and seismicity, San Francisco Bay region, California. *Bull. Seismol. Soc. Am., 95(2),* 446-470, 2005.

Oppenheimer, D.H., Bakun, W.H. and Lindh, A.G. (1990) Slip Partitioning of the Calaveras Fault, California, and Prospects for Future Earthquakes. *J. Geophys. Res, 95(B6),* 8483-8498, 1990.

Waldhauser, F., and D. P. Schaff, Large-scale relocation of two decades of Northern California seismicity using cross-correlation and double-difference methods, *J. Geophys. Res., 113,* B08311, doi:10.1029/2007JB005479, 2008.

Waldhauser, F., Near-real-time double-difference event location using long-term seismic archives, with application to Northern California, *Bull. Seism. Soc. Am., 99,* 2736-2848, doi:10.1785/0120080294, 2009.

23 High-Resolution Imaging of Hayward Fault Microearthquakes

Taka'aki Taira, Douglas S. Dreger, Robert M. Nadeau

Introduction

The connection between the strength of tectonic faults and earthquake rupture is central to studies of the physics of earthquakes. Earthquake stress drop is one of the source parameters for the earthquake rupture process that can be obtained from observed waveforms. The resultant stress drop could reflect the state of stress and the strength of the rocks in which the faulting occurs. To investigate spatial variations of fault strength along the Hayward fault (HF), California, we perform a finite-fault modeling for M 3+ HF earthquakes to obtain the spatial heterogeneity of stress drop within rupture area. We here summarize the slip distributions for the recent two M~3 Orinda earthquakes (Figure 2.23.1). The first Orinda earthquake (OR13-1) with a M_w of 3.0 occurred on October 7, 2013 at a depth of about 7 km. Subsequently, on October 15, the M_w 3.2 Orinda earthquake (OR13-2) occurred ~400 m southeast of the first M_w 3.0 Orinda earthquake. Our finite-fault source modeling reveals that the 2013 M_w 3.2 Orinda earthquake has a complex rupture process.

Hayward Fault Network

We make use of borehole seismograms from the Hayward Fault Network (HFN) to determine the slip models for M 3+ HF earthquakes. The HFN is an array of borehole instrumentation deployed along the HF, with the aim of improving monitoring of spatiotemporal evolution of microseismicity. The HFN was initially deployed with 10 borehole stations in 1995-1996 with a collaborative effort between the Berkeley Seismological Laboratory and U.S. Geological Survey. The 22 borehole stations are currently operational, which provide an unprecedented high-resolution coverage of the earthquake source study for HF earthquakes (Figure 2.23.1).

The stations are typically equipped with three-component

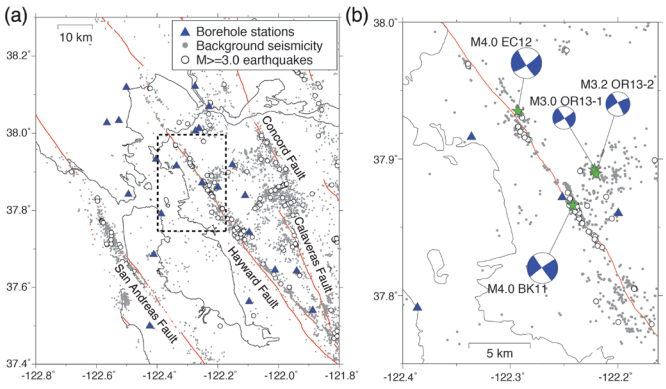

Figure 2.23.1: (a) Map view of HF seismicity in 1990–2013. Blue traiangles are the HFN borehole staions. Gray dots are the locations of background earthquakes from *Waldhaser and Schaff* (2008). Also shown are the locations of M 3+ earhquakes (open ciecles). (b) Enlarged veiw of HF seismicity near Berkeley defined by the dashed-black rectangle shown by Figure 2.23.1a.

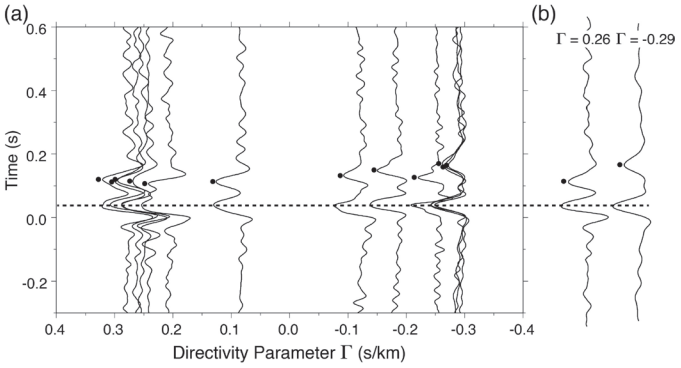

Figure 2.23.2: (a) MRFs for the 2013 M_w 3.2 Orinda earthquake plotted as a function of directivity parameter Γ, assuming rupture azimuth (f_r) at 331°N with phase velocity of 3.4 km/s. A positive value of Γ indicates station azimuth along the rupture direction. Black dots indicate the peaks of the second pulse on indivisual MRFs. (b) Two MRFs from stations at positive and negative Γ illustrate the increase of differential time between the two pulses with Γ.

short-period geophones (the natural frequency is either 2.0 Hz or 4.5 Hz) and accelerometers at a depth of 30–200 m. The seismic data are sampled at up to 500 Hz, although the majority of data used are sampled at 100 Hz. The seismic data has been archived at the Northern California Earthquake Data Center (NCEDC). All waveforms used in this study were extracted from the NCEDC.

Moment Rate Function

We employ an empirical Green's function (eGf) deconvolution approach to extract the moment rate function (MRF) for the two M~3 Orinda earthquakes (*Mori* and *Hartzell*, 1990). We find that the resulting MRFs of the 2013 M_w 3.2 Orinda earthquake display two clear peaks that suggest a radiation complexity in the rupture process. By using waveforms from different eGf events, we confirm that these two peaks on MRFs are not due to a choice of eGf events. To further explore the complexity of the 2013 M_w 3.2 Orinda earthquake, we plot the MRFs with the directivity parameter Γ (e.g., *Ammon et al.*, 2006) based on the equation, $G_i = \cos(f_i - f_r)/c$ where f_i and f_r are the azimuth of the i-th station from the epicenter and the rupture direction, respectively; c is the phase velocity. As shown in Figure 2.23.2, the second pulse appears to shift systematically to later times with an increase of the azimuth (*i.e.*, negative Γ) relative to the direction 331°N (parallel to the strike of HF) with a phase velocity of 3.40 km/s. The linear moveout of the second pulse suggests two distinct subevents involved in the rupture process and the two subevents are aligned along an azimuth of 331°N.

Finite-Fault Inversion

Following *Dreger* (1994), we invert the MRFs to obtain the spatial distribution of fault slip. In the inversion, we define the fault surface as a single 1 km x 1 km plane and divide it into 961

32 x 32 m subfaults. We employ a non-negative least-squares algorithm of *Lawson and Hanson* (1974) and apply a spatial smoothing with a constant smoothing factor.

The slip distribution of the 2013 M_w 3.2 Orinda earthquake shows two distinct subevents (Figure 2.23.3). The first subevent (subevent A) located near the hypocenter of this earthquake (depth of 6.6 km) and the other subevent (subevent B) located about 100 m northwest from the hypocenter at a depth of 6.2 km. The peak slips of the subevents A and B are 4 cm and 2 cm, respectively. With a grid-search approach, we find that a combination of rise time of 0.02 s and rupture velocity of 2.55 km/s provides the maximum variance reduction (96%) for the 2013 M_w 3.2 Orinda earthquake. The static stress drop is determined by using a method introduced by *Ripperger and Mai* (2004). The peak static stress drops for subevents A and B are determined to be 18 MPa and 10 MPa, respectively. Our finite-fault inversion suggests a strong spatial small-scale heterogeneity of the strength of fault within the 2013 M_w 3.2 Orinda earthquake rupture area.

In contrast, the slip distribution of the 2013 M_w 3.0 Orinda earthquake is characterized by failure of a single 0.05 km^2 asperity with a maximum slip of 4 cm (Figure 2.23.4). The high slip area is located immediately down-dip from the hypocenter. The maximum and median stress drops are estimated to be 22 MPa and 8 MPa, respectively. We identify an optimal combination of rise time = 0.015 and rupture velocity = 3.05 km/s for the 2013 M_w 3.0 Orinda earthquake.

Interestingly, our finite-fault inversion shows that the fault rupture also propagated up-dip slip toward the hypocenter of the 2013 M_w 3.2 Orinda earthquake. This result suggests a triggering of the 2013 M_w 3.2 Orinda earthquake by the static stress change imparted by the 2013 M_w 3.0 Orinda earthquake.

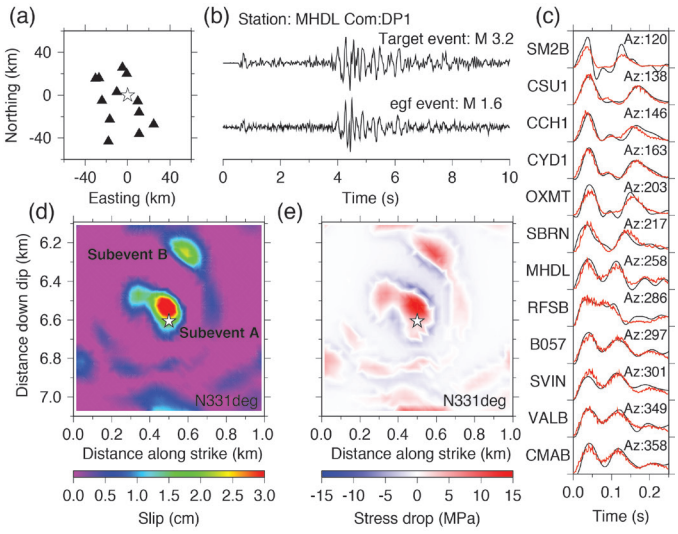

Figure 2.23.3: Finite-fault inversion result for the 2013 M_w 3.2 Orinda earthquake. (a) Map view of the target event (star) and the borehole stations (triangles). (b) Example waveforms for the target and eGf earthquakes. (c) Observed (black lines) and synthetic (red lines) MRFs. (d) Slip and (e) stress drop distributions. The variance reduction obtained for this inversion is 96%.

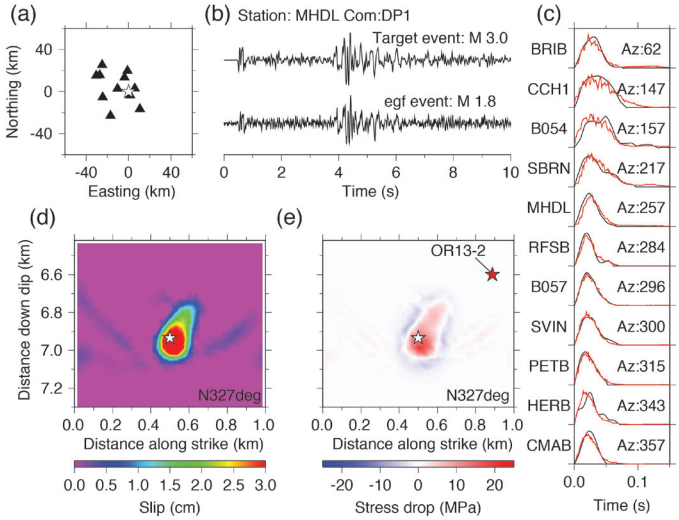

Figure 2.23.4: Same as Figure 2.23.3 except for the 2013 M_w 3.0 Orinda earthquake. Red star in Figure 2.23.4e is the hypocenter of the 2013 M_w 3.2 Orinda earthquake that occurred eight days after the 2013 M_w 3.0 Orinda earthquake. The variance reduction is 96% for this inversion.

Acknowledgements

Waveform data, metadata, and earthquake catalog for this study were accessed through the Northern California Earthquake Data Center. This work is partially supported by the U.S. Geological Survey through award G10AC00093.

References

Ammon, C.J. et al., Rupture process of the 2004 Sumatra-Andaman earthquake, *Science*, 308, doi:10.1126/science.1112260, 2005.

Dreger, D.S., Northridge, California earthquake, *Geophys. Res. Lett.*, 21(24), 2633–2636, doi:10.1029/94GL02661, 1994.

Lawson, C. L., and R. J. Hanson, Solving least squares problems, *Prentice Hall*, Englewood Cliffs, NJ, 1974.

Mori, J., and S. Hartzell, Source inversion of the 1988 Upland, California, earthquake: Determination of a fault plane for a small event, *Bull. Seismol. Soc. Am.*, 80(3), 507–518, 1990.

NCEDC, Northern California Earthquake Data Center, UC Berkeley. Dataset, doi:10.7932/NCEDC, 2014.

Ripperger, J., and P.M. Mai, Fast computation of static stress changes on 2D faults from final slip distributions, *Geophys. Res. Lett.*, 31, L18610, doi:10.1029/2004GL020594, 2004.

Waldhauser, F., and D.P. Schaff, Large-scale relocation of two decades of Northern California seismicity using cross-correlation and double-difference methods, *J. Geophys. Res.*, 113(B8), B08311, doi:10.1029/2007JB005479, 2008.

Research Studies:
Seismic Sources

24 Temporal Variations of Intraslab Earthquake Activity Following the 2011 Tohoku-Oki Earthquake

Brent Delbridge, Roland Bürgmann, Saeko Kita, and Toru Matsuzawa

Introduction

Understanding the mechanics of the subduction of cold oceanic lithosphere is crucial to the theory of plate tectonics and subduction zone seismogenesis. The locked zone between the subducting and overriding plates host the planet's largest earthquakes, including all of the recorded events of moment magnitude 9.0 or larger. These thrust events have been extensively studied, however a significant portion of subduction zone events are intraplate events, which occur within, rather than along the boundary of, the subducting slab. These intraplate earthquakes are frequent and often damaging events that pose a large seismic hazard to large populations along convergent boundaries across the globe. In general, we have a limited understanding of the processes producing these events due to the complexity and heterogeneity of their spatial and temporal distributions.

Most earthquakes deeper than 40 km are located within the subducting plate itself and form two inclined planes of seismicity separated by approximately 35 km, which delineate the plate curvature as it subducts into the surrounding mantle. The presence of these double seismic zones at intermediate depths complicate our understanding of subduction zone seismogenesis and requires an understanding of local sources of stresses. We expect that the large-scale tectonic processes such as slab-pull would create down-dip extensional stresses from the negative buoyancy from the sinking of the cold oceanic lithosphere, however *Hasagawa et al.* (1978) found that beneath Tohoku the earthquake focal mechanisms of the upper plane reflect down-dip compressional stresses, while the lower plane events are associated with down-dip extensional stresses.

In this study we examine the temporal changes of intraplate earthquake activity following the 2011 M_w 9.0 Tohoku-oki earthquake. Due to the large rupture area and displacement of the M_w 9.0 thrust event, we expect that the stress changes within the slab from the coseismic displacement and post-seismic changes in stressing rate due to mantle relaxation and afterslip could be comparable with those from slab pull and bending. Consequently, we examine if the intermediate-depth earthquakes down plate from the locked region reflect the stress change from the slab decoupling and corresponding postseismic processes. Specifically we expect that earthquake activity in the upper plane of the Tohoku region, which is largely down dip compressional, would be promoted, while the earthquake activity in the lower plane, which is largely down-dip extensional would be suppressed, relative to their pre-Tohoku-Oki earthquake levels. Capitalizing on insights into the large-scale and long-term behavior of deformation in subduction zones using models of thin sheets, we quantify the effect of slab bending on subduction zone seismogenesis. We combine laboratory-based rheological models, precise estimates of slab shape from relocated earthquake hypocenters, estimates of the state of stress in the plate from intraplate focal mechanisms, and response to the 2011 Tohoku-Oki earthquake to provide constraints and insights for intraplate subduction zone seismogenesis.

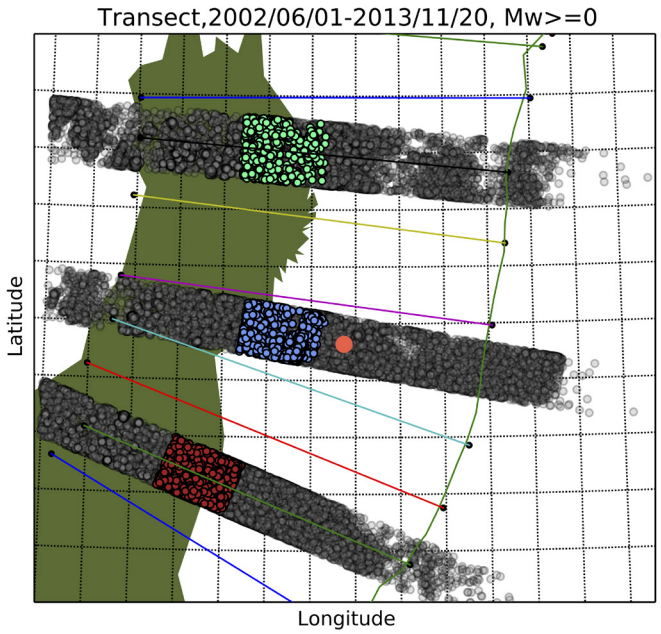

Figure 2.24.1: Map Overview of Study Area. The large orange circle shows the location of the 2011 M_w 9.0 Tohoku-Oki earthquake hypocenter. The green line shows the location of the Japan trench, and the colored circles show the location of events used in this analysis. The grey circles represent the transect hypocenters not included in the temporal analysis.

Tohoku State of Stress

The seminal work of *Isacks and Molnar* (1969) showed that intraplate earthquakes can by used to infer the large-scale stresses within the subducting slab and observed that below 300 km depth events are dominated by down-dip compression, whereas from 70–300 km depth the events are dominated by down-dip extension. These tensional events are thought to reflect the stresses associated with the negative buoyancy of the sinking plate, and the ability of the lithosphere to coherently transmit stresses.

However, the presence of double seismic zones and spatial heterogeneity complicate this simple picture, and require the regional stresses from slab bending and lateral variations to play a large role in the processes producing these events. In addition, observed temporal changes in intraplate earthquake activity associated with the coupling and uncoupling of the subducting lithosphere in the regions of large thrust events suggest that these stresses are comparable to the stresses associated with bending, unbending and slab-pull (*Ammon,* 2008). Further, the depth-dependent nature of the upper plane requires that the equilibrium thermal structure of the slab is also a controlling

factor in subduction zone seismogenesis (*Kita et al.,* 2010).

Previous studies have proposed models that suggest several mechanisms controlling the large-scale stress regimes generated during the subduction process (*Lay et al.,* 1989). The static stress field is associated with the large-scale stresses generated by bending, unbending, thermal equilibrium, and slab pull, with a superimposed dynamic stress field generated by the coupling and uncoupling of the subduction thrust separating the oceanic lithosphere and the overriding continental plate. This model was examined globally by *Lay et al.* (1989), but they were unable to determine with confidence the validity of this model due to insufficient data and the complexity of the intermediate-depth events. However, they were able to conclude qualitatively that intermediate depth events exhibit a strong temporal nature associated with large thrust events, in which the region may undergo a transition from down dip extensional to down-dip compressional stresses.

In order to resolve the contributions of the multiple mechanisms to the state of stress in the subducting slab we will examine the temporal variation of the intermediate earthquake activity in the Tohoku region following the 2011 Tohoku-Oki earthquake. Specifically, we hope to parse out the role of each of the following processes in the generation of the stress regimes inferred from the earthquake focal mechanisms: bending, slab-pull, dynamic coupling and postseismic processes. We utilize earthquake hypocenters from the JMA catalog, which utilizes a dense seismic network completed in 2002 that includes over 1200 stations and records approximately 105 events per year.

We test whether the Tohoku-Oki 9.0 thrust event promoted compressional events and suppressed extensional events at intermediate depths by examining how the relative number of events in the contractional upper plane and extensional lower plane of the Tohoku double seismic zone change before and after the thrust event. It is important to examine the ratio rather than the absolute number of extensional and compressional events due to the overall increase in seismicity following the M_w 9.0 event.

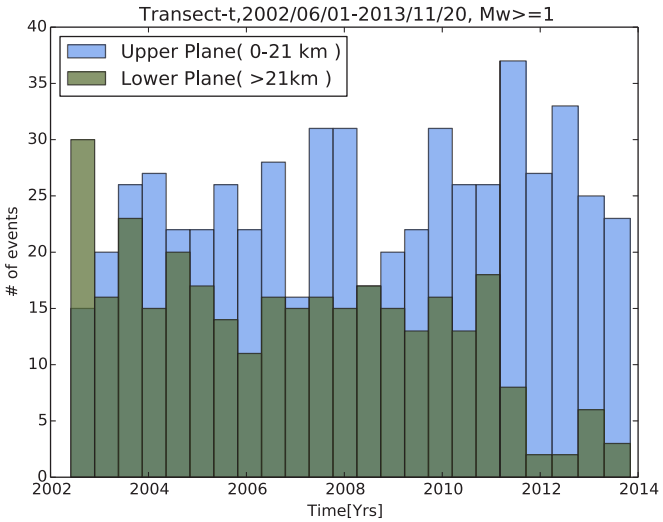

Figure 2.24.2: A histogram showing the earthquake rate in the upper plane (blue) and the lower plane (green) versus time for the Tohoku-Oki study area events show in blue in Figure 2.24.1.

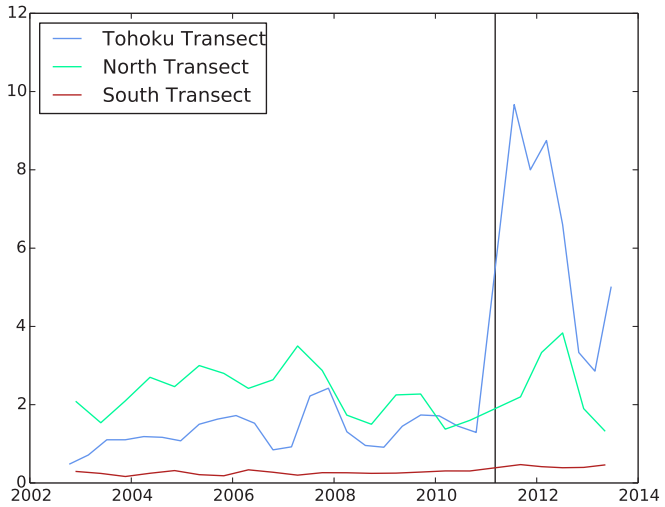

Figure 2.24.3: In order to test for a systematic bias following the Tohoku-Oki Earthquake we plot the activity ratio versus time plots for three regions. The color of the curves corespond to the events shown in Figure 2.24.1.

We find that following the Tohoku-Oki earthquake, the ratio of the number of events in the compressional upper plane to the extensional lower plane increased by a factor of three to five as shown in Figure 2.24.3. The spatial distribution of these events before and after the earthquake show that almost all activity in the extensional lower plane ceases close to the rupture zone, whereas the same region of the compressional upper plane remains seismically active. We conclude that the response of the seismicity at intermediate depths to the compressional stresses from the Tohoku-Oki earthquake are consistent with the conceptual model presented by *Lay et al.* (1989). In future work we hope to quantify and model the stress changes from the Tohoku earthquake and its postseismic relaxation, which will allow us to put absolute constraints on the pre-earthquake stress levels in the subducting slab.

Acknowledgements

This material is based upon work supported by the National Science Foundation Graduate Research Fellowship.

References

Ammon, C. J., Kanamori, H., & Lay, T., A great earthquake doublet and seismic stress transfer cycle in the central Kuril islands. *Nature*, 451(7178), 561-565, 2008.

Hasegawa, A., Umino, N., & Takagi, A., Double-planed structure of the deep seismic zone in the northeastern Japan arc. *Tectonophysics*, 47(1), 43-58, 1978.

Isacks, B., & Molnar, P., Mantle earthquake mechanisms and the sinking of the lithosphere. *Nature*, 223(5211), 1121-1124, 1969.

Kita, S., Okada, T., Hasegawa, A., Nakajima, J., & Matsuzawa, T., Existence of interplane earthquakes and neutral stress boundary between the upper and lower planes of the double seismic zone beneath Tohoku and Hokkaido, northeastern Japan. *Tectonophysics*, 496(1), 68-82, 2010.

Lay, T., Astiz, L., Kanamori, H., & Christensen, D. H., Temporal variation of large intraplate earthquakes in coupled subduction zones. *Physics of the earth and planetary interiors*, 54(3), 258-312, 1989.

25 Moment Tensor Inversion of Seismic Events and Tremor-Tilt Observations Associated with the Sinkhole at Napoleonville Salt Dome, Louisiana

Avinash Nayak and Douglas S. Dreger

Introduction

The formation of a large sinkhole at the Napoleonville salt dome (NSD), Assumption Parish, Louisiana (Figure 2.25.1) in August, 2012 was accompanied by a rich sequence of complex seismic events. Preliminary investigations suggest that the possible collapse of the sidewall of a plugged and abandoned brine cavern, Oxy Geismar 3, might be a potential cause of the sinkhole. It has been hypothesized that the collapse fractured to the surface, creating a disturbed rock zone, which provides a pathway for formation fluids, natural gas and crude oil from deeper strata that are now accumulating in the sinkhole and the surrounding aquifer.

Figure 2.25.1: Google Earth Image (dated March 12, 2013) shows the study region at the western edge of NSD, with 1000 ft and 10,000 ft contours indicated by white lines, locations of the five USGS broadband stations (white triangles), approximate location of the Oxy Geismar 3 cavern (white square), and an average point location of the sinkhole (white balloon).

Moment Tensor Inversion

We investigate source mechanisms of these seismic events, represented by a general point source centroid seismic moment tensor (MT). We use data recorded by a temporary network of broadband seismometers deployed by the U.S. Geological Survey (USGS). Because of uncertainties in hypocenters estimated from travel-times and large number of seismic events, we employ a grid-search approach, GRiD MT (*Kawakatsu*, 1998), which continuously scans the seismic wavefield and performs MT inversions of low frequency displacement waveforms (causal 0.1-0.2 Hz 4-pole Butterworth filter) assuming a discrete 3D grid of point sources. For a given time window of data, the source location and MT solution which give the best Variance Reduction (VR) is inferred to be the true seismic source. Green's functions are computed using frequency-wavenumber integration software FKRPROG using two separate 1D velocity models for the salt dome and the surrounding sediment sequence.

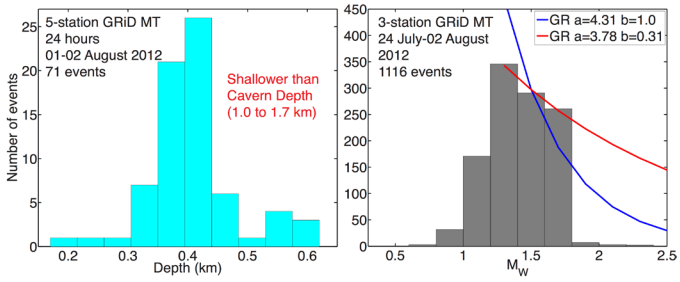

Figure 2.25.2: Source depth and M_W distribution. Red and blue lines are Gutenberg Richter relationships for various 'a' and 'b' values.

Application of GRiD MT to 24 hours of data during August 1–2, 2012 (just before the appearance of the sinkhole) with a 71% VR detection threshold reveals 71 events with magnitudes M_W 0.8 to 1.9. Their locations are well constrained to the western edge of the salt dome, close to the sinkhole, at an approximate depth of ~420 m, which is much shallower than the roof of the cavern at 1.0 km (Figure 2.25.2). The M_W distribution of ~1100 events detected during an extended period of time doesn't follow the Gutenberg Richter relationship and shows distinct absence of larger magnitude events indicating a structural limit on size of the source.

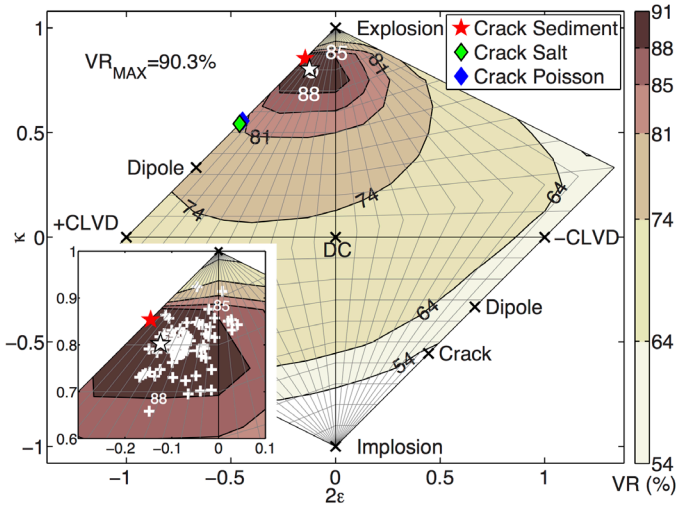

Figure 2.25.3: NSS of event TE1 on the Hudson source-type plot, major theoretical source-types (black crosses), tensile cracks in various media and full MT solution of event TE1 (white star). White circle is the source-type corresponding to the maximum VR recovered by NSS (VR_{MAX}). The inset shows distribution of 71 events of the seismic sequence (white '+' signs) in source-type space.

The MT solutions are comprised of large (66-92%) isotropic volume-increase components, and can be interpreted as a N-NE striking steeply dipping tensile crack in a high Poisson ratio (0.43) medium coupled with a normal-style double couple. For one representative event, TE1, the volume-increase component

is found to be statistically significant using an F-test and stable with respect to: (1) velocity models and stations used, (2) first motion polarities, and (3) uncertainties in GRiD MT location and MT elements. In the network sensitivity solution (NSS) of Figure 2.25.3, MT solutions that produce best fits (>80% VR) are tightly clustered in a region between theoretical explosions and tensile cracks, quite far away from theoretical deviatoric mechanisms and expected closing crack mechanisms, which produce fits only up to 50-75% VR. For further details on MT analysis of this sequence and a complete list of references, readers are referred to Nayak and Dreger (2014).

We believe that the events in this study are caused by high-pressure flow of natural gas or water-gas mixture through voids in the disturbed rock zone or pre-existing zones of weaknesses like fractures or faults at the edge of the salt dome by volumetric expansion or tensile failure mechanisms similar to those observed in geothermal and volcanic environments. This hypothesis is supported by the intense influx of natural gas (primarily methane) into the aquifer over an area of 5 km^2 around the sinkhole from the disturbed rock zone below. As of September 2013, ~16x10^3 Mcf natural gas has been vented or flared out as a remediation measure.

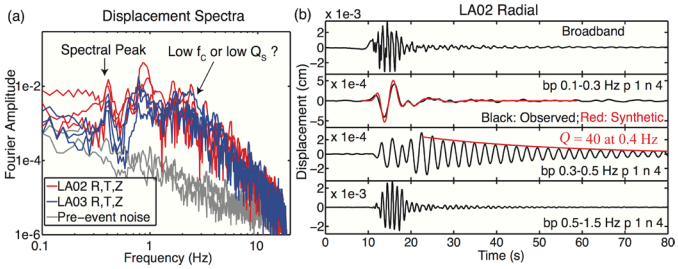

Figure 2.25.4: (a) Spectra at stations LA02 (over sediments) and LA03 (over salt dome); (b) Radial waveforms at LA02 in different frequency bands (see 0.4 Hz oscillatory waveform in third panel).

Tremor-Tilt Observations

We have also observed spectral peaks in data of discrete seismic events and Harmonic Tremor (HT) episodes prior to the appearance of the sinkhole. These seismic signals are usually observed only in volcanic environments and are attributed to oscillatory responses of fluid-filled cavities, gas bubbling and fluid flow through deformable channels. Figure 2.25.4 shows example of three-component spectra of a seismic event with a strong narrowband peak at 0.4 Hz observed at multiple stations. In time domain, it is equivalent to a ~60 s long exponentially decaying sinusoid with a standing wave attenuation factor, Q ~ 40, which is unlikely to be site response due to its long period and duration. The spectra also show a low corner frequency at ~2.0 Hz, which could be due to the slow nature of these events or strong anelastic attenuation in the young sediments.

One of the observed HT episodes is shown in Figure 2.25.5. The fundamental frequency of the HT first increases from ~1.6 Hz to ~2.5 Hz in ~40 s and thereafter stays constant for ~ 80 s. The first overtone frequency and the amplitude envelope follow a similar trend. Low frequency acceleration for the same time period shows a step, which is interpreted to be due to an

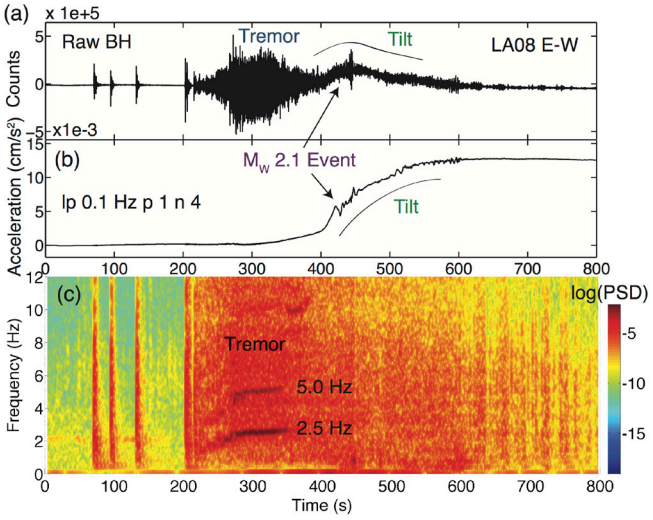

Figure 2.25.5: HT-Tilt episode on August 2, 2012: (a) raw broadband seismogram; (b) low frequency acceleration showing tilt; (c) spectrogram showing HT at 2.5 and 5.0 Hz.

apparent ground tilt of ~ 30.6 μrad. We have found these pseudo-tilt signals to be reliable by examining the horizontal and vertical amplitudes, low frequency SNR and colocated accelerometer waveforms. These observations indicate some common relationship between mechanisms of discrete volumetric events and harmonic tremor, possibly being driven by fluid flow, and surface deformation due to gas escape from the subsurface.

Acknowledgements

We thank William Ellsworth (USGS) for preliminary velocity models, data, mapping resources and helpful discussions. Stephen Horton (CERI, University Of Memphis) is thanked for providing the travel-time catalog of events in this study. We thank Julie Shemeta (MEQ Geo) and Mark Leidig (Weston Geophysical Corp.) for velocity models.

References

Kawakatsu, H., On the realtime monitoring of the long-period seismic wavefield: *Bull. Earthq. Res. Inst.*, 73, 267-274, 1998.

Nayak, A., and Dreger, D.S., Moment tensor inversion of seismic events associated with the sinkhole at Napoleonville Salt Dome, Louisiana: *Bull. Seismol. Soc. Am.*, 104, 4 (*in press*), doi: 10.1785/0120130260, 2014.

26 Preliminary Results of Moment Tensor Analysis at The Geysers Geothermal Field, CA

Sierra Boyd, Voon Hui Lai, and Douglas Dreger

Introduction

The Geysers geothermal field is one of the most seismically active regions in Northern California with shallow microseismicity correlated with geothermal energy operations. More recently there has been an increase in large magnitude, M > 4, events located within the microseismic cloud. Understanding induced seismicity and the physical mechanisms of large magnitude events associated with geothermal energy operations is needed to evaluate seismic hazard associated with reservoir production.

In our ongoing investigation, broadband seismic data from regional networks, inset map Figure 2.26.1, are used to study moment tensors of M > 3 earthquakes throughout the geothermal field. We apply techniques (*Ford et al.,* 2010), to develop a catalog of deviatoric and full moment tensor (FMT) solutions and an assessment of the uncertainty of non-double-couple components of 53 earthquakes at The Geysers from 1992–2014.

Results

Based on the F-test, most of the 53 events may be characterized as deviatoric. However there are 10 events with statistical significance above 80% and 4 above 90%. For these events we have investigated the stability and uncertainty in the long-period full moment tensor inversions using bootstrap, Jackknife and NSS techniques (*Ford et al*., 2010). In cases where events are found to have large positive isotropic components, we find from these sensitivity studies that the results are robust. We have also found cases in which small isotropic components are likely, although based on the waveform data alone and the F-test, they are not resolved. Through the combination of long-period waveforms and first-motions (FM), we are able to obtain stronger constraints on the moment tensor solutions. We are finding that those that best satisfy both data sets are comprised of a large strike-slip double-couple component with a relatively small 10% to 38% volume increase. The results of the constrained full moment tensor (CFMT) analysis of selected events are summarized in Table 2.26.1.

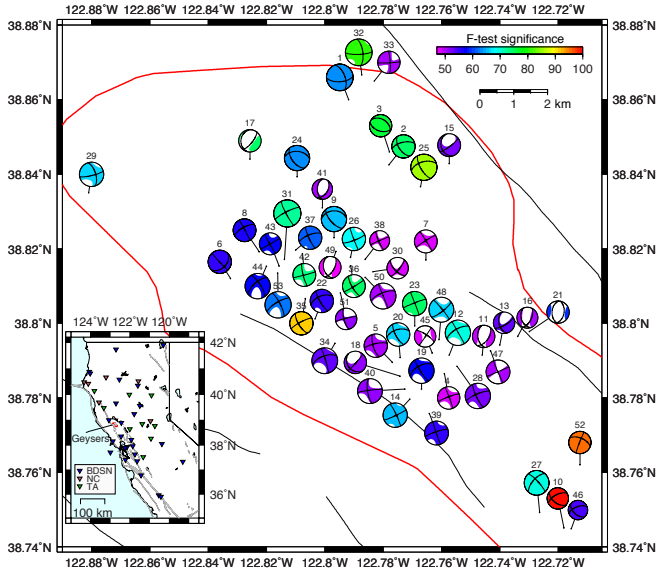

Figure 2.26.1: Full moment tensor solutions shaded by the statistical significance of the isotropic component as determined by the F-test

Acknowledgements

Data for this study come from the Berkeley Digital Seismic Network (BDSN), doi:10.7932/BDSN, operated by the UC Berkeley Seismological Laboratory, Northern California Seismic Network; and the Transportable Array. We thank Roland Gritto, P. Hellweg, T. Taira, P. Lombard, S.-H. Yoo, A. Guilhem, A. Chiang, H. Macbeth, David Oppenheimer, and C. Hartline for their help and support. This material is based upon work supported by the Department of Energy Geothermal Technologies Program under Award Number DE-EE0002756-002.Preliminary

References

Ford, S. R., D. S. Dreger, and W. R. Walter, Network sensitivity solutions for regional moment tensor inversions, *Bull. Seism. Soc. Am., 100,* 1962-1970, 2010.

Date	id #	M_w	FM fit deviatoric	FM fitFMT	FMT VR% DC/CLVD/ISO	FM fit CFMT	CFMT VR% DC/CLVD/ISO
Mar-1-2011	44	4.43	42	29	80.0 42/26/32	25	70.2 67/10/24
Feb-24-2008	37	3.99	48	23	78.7 33/19/48	21	69.5 43/19/38
May-12-2006	31	4.71	57	56	83.4 29/35/36	27	43.9 45/34/20
Jan-16-1995	9	4.14	38	40	68.9 27/8/65	23	57.4 86/4/10

Table 2.26.1: Summary of first-motion (FM) fits to deviatoric, full moment tensor (FMT), and constrained FMT (CFMT) solutions as measured by the number of discrepant first-motion observations. A high number of discrepant observations indicates a poor fit. The FMT and CFMT results are presented in columns 6 and 8, respectively, with the variance reduction (goodness of fit) and the percent components of double-couple (DC), compensated linear vector dipole (CLVD), and isotropic (ISO).

27 Moment Tensor Analysis of Shallow Sources

Andrea Chiang and Douglas S. Dreger

Introduction

For the nuclear explosion source-type identification problem, the uncertainty in a solution is as important as the best fitting parameters. A potential issue for shallow seismic sources that are effectively at the free-surface between the ground and air is that the vanishing traction at the free-surface can cause the associated vertical dip-slip (DS) Green's functions to have vanishing amplitudes (*Julian et al.*, 1998), which in turn can result in the indeterminacy of the M_{xz} and M_{yz} components of the moment tensor and bias in the moment tensor solution. The effects of the free-surface on the stability of the moment tensor method becomes important as we continue to investigate and improve the capabilities of regional full waveform moment tensor inversion for source-type identification and discrimination. It is important to understand its effects for discriminating shallow explosive sources in nuclear monitoring, but could also be important in natural systems that have shallow seismicity such as volcanic environments and geothermal systems. The HUMMING ALBATROSS quarry blast is an excellent dataset in terms of understanding the effects of free-surface vanishing traction using real data. These small chemical explosions are approximately 10 m deep and are recorded at up to several km distances. Therefore the data represent a rather severe source-station geometry in terms of vanishing traction issues. It is possible to obtain a robust full moment tensor solution that is comprised dominantly by an isotropic or explosive component, however the data provide the opportunity to evaluate capabilities of moment tensor inversion as a function of frequency and source depth.

Data and Methods

The HUMMING ALBATROSS data consist of both broadband and short-period seismic recordings (Figure 2.27.1). We applied the moment tensor based discrimination method to two ~M2-2.5 industrial explosions. Following the results of *Ford et al.* (2012) and *Chiang et al.* (2014) we incorporated full waveform data from five broadband stations and P-wave first motions from sixteen broadband and short-period stations into our moment tensor analysis. The broadband waveform data are filtered between 0.5 to 2 seconds depending on the signal-to-noise-ratios, and we examined the results in two frequency bands to understand the frequency dependence of free-surface vanishing traction. To further assess the uncertainties in the moment tensor inversion result, we looked at how the solution behaves in the *Hudson et al.* (1989) source-type space. Following the Network Sensitivity Solution (NSS) method proposed by *Ford et al.* (2010), we randomly generated 80 million moment tensor solutions that are uniformly distributed on the Hudson source-type plot, and for each random solution we compared the waveform fits and P-wave first motion picks between the data and synthetics. Here we compare two types of NSS result: waveform data only and waveform data with local P-wave polarity constraints.

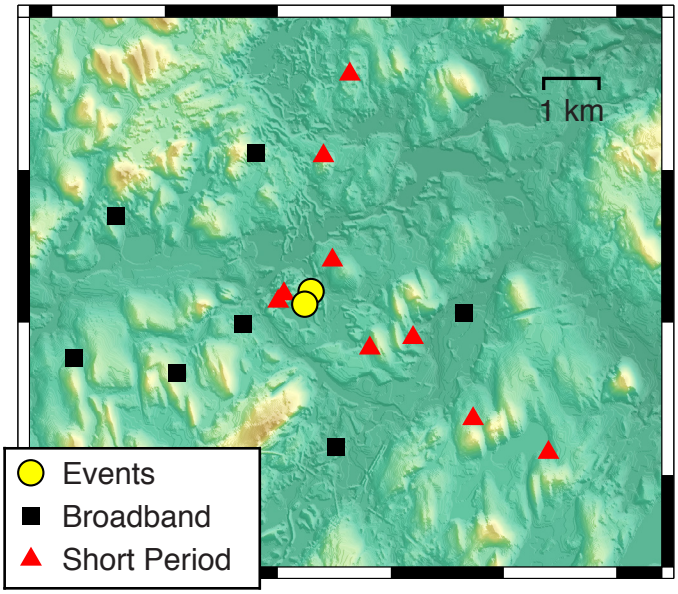

Figure 2.27.1: Event and station locations of the studied events. Circles are the two low magnitude industrial explosions, squares are the broadband stations, and triangles are the short-period stations. We used five broadband stations for the full waveform analysis and sixteen broadband and short-period stations for the P-wave first motion picks.

Source-Type Analysis

Given the frequency band and source-receiver distance, the moment tensor inversion is not sensitive to source depths shallower than ~150 m, but the solutions at these shallow depths remain stable and are dominated by a large isotropic component (Figure 2.27.2). Since we know the depth of the borehole where the explosions are detonated, we can constrain the source depth to be shallower than 15 m. The inversion result best fits the data at 11 m, so we fixed the source depth to 11 m for the subsequent NSS analysis.

In this report, we present findings for the first explosive shot since the moment tensor inversion and NSS results behave similarly for both explosions. The waveform NSS exhibits a trade off between volumetric sources and double-couple sources (Figure 2.27.3a-b). This trade off is likely caused by the combination of large Love waves on the tangential component and free-surface vanishing traction. The large Love wave causes the solution to deviate from a pure explosive mechanism. Vertical dip-slip and explosive mechanisms fitting equally well to the data (Figure 2.27.2) indicate free-surface effects also contribute to the observed trade off. The trade off becomes more pronounced at longer periods because free-surface effects are more severe at longer wavelengths. To eliminate the trade off we applied additional constraints from P-wave first motions, and the resulting NSS's show the best-fitting solutions to both waveform and P-wave first motion are constrained to mechanisms with a dom-

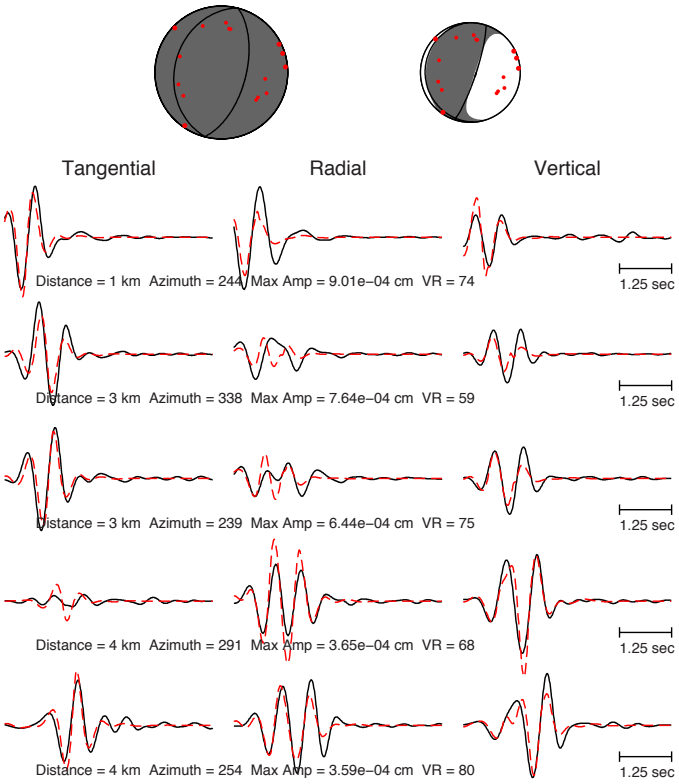

Figure 2.27.2: Full and deviatoric moment tensor solutions from waveform inversion. Displacement waveforms (black solid lines) and full moment tensor synthetics (red dashed lines) are filtered between 1.25 to 2 second period. P-wave up first motions (red dots) are plotted on top of the focal mechanisms.

inant isotropic or volumetric increase component, including the full moment tensor solution from waveform inversion (Figure 2.27.3c-d). The additional P-wave polarity information provides an important constraint because it eliminates mechanisms such as the vertical dip-slip (Figure 2.27.3), and discriminates the event as predominantly explosive.

Conclusions

Previous studies have shown that including P-wave first motions in addition to full waveform data can eliminate the common ISO-CLVD trade off (*Ford et al.*, 2012; *Chiang et al.*, 2014) and reduce the uncertainties of sparsely recorded underground explosions with strong Love waves (*Chiang et al.*, 2014). Here we demonstrated that although we cannot uniquely characterize the HUMMING ALBATROSS events as predominantly explosive using only waveform data, the combined waveform and first motion method enables the unique discrimination of these events. The combined method not only applies to larger man-made and natural seismic events, but also small magnitude, very shallow explosive sources that are effectively at the free surface. The combined method gives a well-constrained NSS even as we go towards longer periods, where the effects of free-surface vanishing traction are more pronounced. The combination of both low frequency full waveform data and high frequency P-wave polarities greatly enhances the capabilities of the moment tensor source-type discrimination method in cases

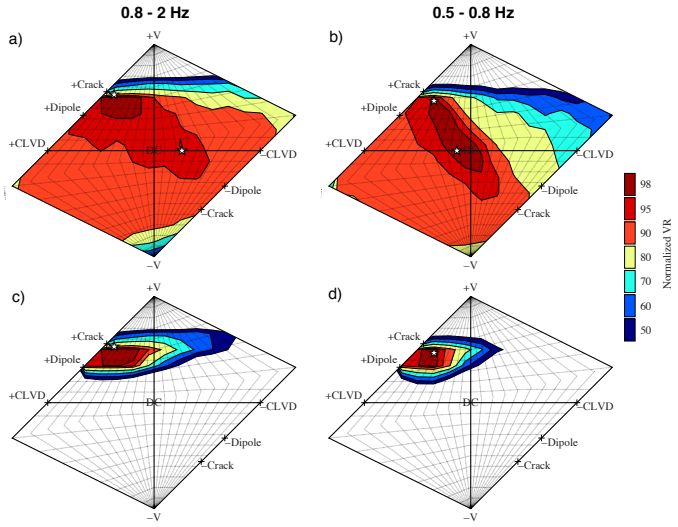

Figure 2.27.3: Network Sensitivity Solutions at two frequency bands. We plotted the full and deviatoric solutions (white stars) on top of the waveform NSS (a-b) and the combined waveform and first motion NSS (c-d).

of sparse station coverage, strong Love waves and free-surface effects due to very shallow source depths.

Acknowledgements

We acknowledge funding from the Air Force Research Laboratory, contract FA9453-10-C-0263 that is supporting this research.

References

Chiang, A., Dreger, D. S., Ford, S. R., Walter, W. R., Source characterization of underground explosions from combined regional moment tensor and first motion analysis, *Bull. Seismol. Soc. Am.*, *104*, doi:10.1785/0120130228, 2014 (*in press*).

Ford, S. R., Dreger, D. S., Walter, W. R., Network Sensitivity Solutions for regional moment-tensor inversions, *Bull. Seismol. Soc. Am., 100*, 1962-1970, doi:10.1785/0120090140, 2010.

Ford, S. R., Walter, W. R., Dreger, D. S., Event discrimination using regional moment tensors, *Bull. Seismol. Soc. Am., 102*, 867-872, doi:10.1785/0120110227, 2012.

Hudson, J. A., Pearce, R. G., Rogers, R. M., Source type plot for inversion of the moment tensor, *J. Geophys. Res., 94*, 765-774. 1989.

Julian, B. R., Miller, A. D., Foulger, G. R., Non-doublecouple earthquakes 1. Theory, *Rev. Geophys.*, *36*, 525-549, doi:10.1029/98rg00716, 1998.

28 Lessons Learned from Broadband Waveform Modeling Across the Mendocino Triple Junction

Michael Faggetter, Douglas Dreger

Introduction

The 1D calibrated Gil7 velocity model has been shown to generate realistic seismograms for Northern California *(Dreger and Romanowicz, 1994)* and is currently used for the automated calculation of moment tensors at long periods (greater than 10-20 s) at the Berkeley Seismological Laboratory (BSL). An improved model, Mend1 *(Tajima et al., 2000)*, is able to generate more realistic Green's Functions (GFs) for events in the Mendocino, CA region for the same period range. However, these 1D models are less suited to offshore, regional events near Mendocino since they cannot accurately reproduce the transitional oceanic-continental path, especially at higher frequencies. Broadband waveform modeling of offshore events is further complicated by factors such as the distance and azimuthal bias from stations. Also, the sparse distribution of earthquakes is likely to result in path-specific 1D velocity models that do not represent the full 3D structure.

In this study, a well-recorded M_w 4.47 aftershock from the recent M_w 6.8 event in the Mendocino region was used to develop an improved 1D model for offshore events. A standard forward modeling approach was adopted by comparing instrument-corrected, three-component broadband observations with synthetic data at multiple bandwidths. Station KMPB (Figure 2.28.1) was primarily used for this process due to its proximity to the hypocenter and location close to an SH-wave radiation maximum.

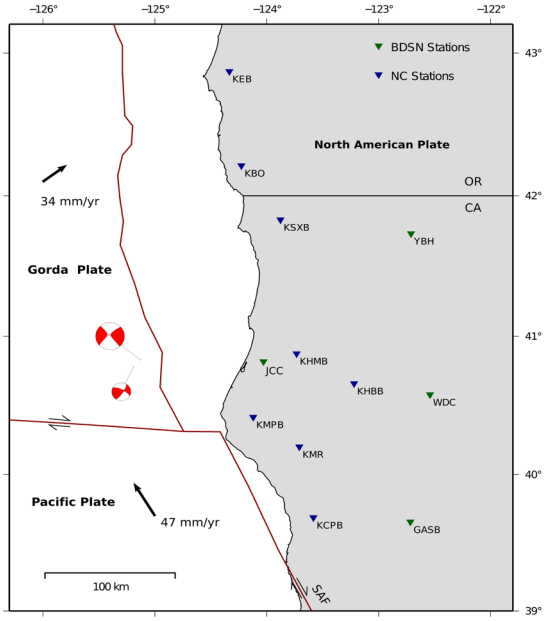

Figure 2.28.1: A map of the Mendocino region showing stations from the Berkeley Digital Seismic Network (BDSN) and Northern California Seismic Network (NCSN) that were investigated in this study. Focal mechanisms from the Berkeley Moment Tensor Catalog for the mainshock and largest aftershock are shown, scaled in size by magnitude, with lines pointing to their true epicentral locations. Single arrows depict plate motions relative to stable North America taken from the updated NUVEL-1A plate motion model of *DeMets et al.* (1994).

Synthetic Data

To generate synthetics, initial source parameters were taken from the BSL moment tensor catalog. *Chaytor et al.* (2004) hypothesized that many offshore strike-slip events in this region are the consequence of reactivating the normal, paleo-rift fabric in the central Gorda plate. Therefore, the preferred fault-plane solution was chosen based on the sub-parallel alignment to these fractures. The hypocentral depth was calibrated using the current velocity models.

1D GFs were calculated from an input velocity model using a frequency-wavenumber integration (FI) method *(Saikia, 1994)*. Fundamental-fault GFs were then summed to match the chosen mechanism and convolved with a calibrated ω^{-2} source-time function. The duration of this function was determined by comparing Gil7 synthetics with KMPB in the frequency domain. Changes to Q provided no significant improvement to the fit of the high frequency asymptote greater than the corner frequency, and initial values from Gil7 were retained for the new model.

Path Calibration

Multiple initial models were investigated based on seismic refraction studies from the Mendocino Triple Junction Seismic Experiment (MTJSE). Fits between the synthetics and observations were improved by iteratively perturbing parameters in the input velocity model.

Forward modeling by visual inspection between seismograms is reliable at long periods where fits to amplitude, and to some extent phase, can be determined. To more precisely match higher frequencies and obtain a reliable and quantitative measure of phase, a goodness-of-fit (GOF) measure was used. This measure was calculated from the weighted sum of five different metrics, each of which was converted to a normalized residual and summed following the method of *Olsen and Mayhew* (2010). The five metrics were measures of: 1) time-domain amplitudes between 0.1 and 1 Hz; 2) time-domain amplitudes for frequencies less than 0.1 Hz; 3) amplitude-independent phase for frequencies less than 0.1 Hz; 4) amplitude-independent phase at frequencies less than 0.5 Hz; 5) amplitudes of smoothed Fourier spectra less than 1 Hz.

By equally weighting each metric, this GOF measure was used as an objective function for a partially automated grid-search algorithm to improve upon the previous forward modeling.

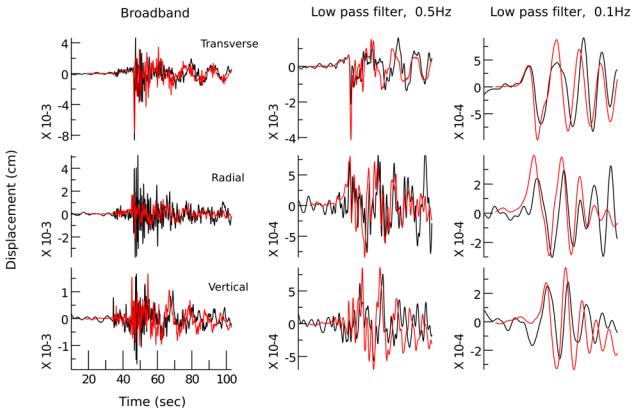

Figure 2.28.2: A comparison between MenPB synthetics (red) and instrument-corrected displacement time histories at KMPB (black). The first column shows unfiltered (broadband) data. The second and third columns show data filtered using a lowpass Butterworth filter with a corner frequency of 0.5 Hz and 0.1 Hz respectively.

Results

Table 2.28.1 lists the best 1D model for KMPB, named MenPB, obtained using this method. MenPB is derived from a complex hybrid of the current velocity models and was modified to include a double Moho. The latter feature is evidenced by *Beaudoin et al.* (1996) and others, and accurately reproduces several large amplitude reflections after the direct S wave, that are absent from structural models that simply increase with depth.

MenPB synthetics match observations well for all three components at KMPB up to 1 Hz. At least 60 seconds are well modeled on the tangential component, however the radial displacement record contains several late-arriving multi-path rays that are not reproduced with the 1D model (Figure 2.28.2). MenPB is able to fit observations particularly well for paths to stations of a similar azimuth to KMPB and to the northeast, including stations KMR and KSXB. Directly east of the event, surface wave amplitudes are significantly lower and are overestimated by the thick, low velocity surface layers in MenPB.

For a moment tensor inversion at long periods (0.02-0.05Hz), using GFs calculated using MenPB results in a mean increase in variance reduction of four compared to Gil7. For an inversion at 0.02–0.08 Hz, variance reduction increases by up to a factor of two for KMPB and KMR but with negligible change for stations to the northeast.

Conclusion

Ray paths that pervade the Gorda plate and the Franciscan accretionary complex are strongly influenced by thick, slow sediments in the shallow structure. For the northeast and southeast paths, waveforms contain large amplitude surface waves that persist for up to 50 seconds. For stations directly to the east, surface waves are damped by a predominantly continental path, and waveforms feature high frequency arrivals from reflections off the Moho and the mid-crustal high velocity layer. This wide azimuthal range of surface wave amplitudes, and the presence of multipath waves, emphasizes the difficulty of using simplified 1D models, even at long periods.

Layer Thickness (km)	Vp (km/s)	Vs (km/s)	Density (g/cc)
5	2.6	1.5	2.2
1	5.5	3.2	2.9
1	6.6	3.8	3.0
2	8.0	4.6	3.3
5	5.9	3.4	2.9
11	7.1	4.1	3.1
∞	8.0	4.6	3.3

Table 2.28.1: The Final calibrated 1D velocity model, MenPB.

A GOF measure was found to be an invaluable tool for forward modeling. Using multiple user-defined metrics provides flexibility that the routinely used 'variance reduction' does not. For example, metrics can be chosen to target specific criteria when modeling, resulting in more rapid convergence of models in a chosen passband. However, careful selection of the metrics and their weights prior to automated procedures is strongly advised.

Acknowledgements

Moment tensors were computed using the tdmt-invc_iso package developed by Douglas Dreger and Sean Ford of the Berkeley Seismological Laboratory, and Green's functions were computed using the FKRPROG software developed by Chandan Saikia. Data for this study come from the Berkeley Digital Seismic Network (BDSN), doi:10.7932/BDSN, and the Northern California Seismic Network (NCSN).

References

Beaudoin, B. C., Godfrey, N. J., et al., Transition from slab to slabless: Results from the 1993 Mendocino triple junction seismic experiment, *Geology, 24*, 195-199,1996.

Chaytor, J. D., Goldfinger, C., et al., Active deformation of the Gorda plate: Constraining deformation models with new geophysical data, *Geology, 32*, 353-356, 2004.

DeMets, C., Gordon, R. G., et al., Effect of recent revisions to the geomagnetic reversal time scale on estimates of current plate motions, *Geophysical Research Letters, 21*, 2191-2194, 1994.

Dreger, D. S. & Romanowicz, B., Source Characteristics of Events in the San Francisco Bay Area, *USGS Open-file report, 94-176*, 301-309, 1994.

Olsen, K. B. & Mayhew, J. E., Goodness-of-fit Criteria for Broadband Synthetic Seismograms, with Application to the 2008 M_w 5.4 Chino Hills, California, Earthquake, *Seismological Research Letters, 81*, 715-723, 2010.

Saikia, C. K., Modified frequency-wavenumber algorithm for regional seismograms using Filon's quadrature; modeling of Lg waves in eastern North America, *Geophysical Journal International, 118*, 142-158, 1994.

Tajima, F., Dreger, D. S., et al., Modeling of the transitional structure from ocean to continent in the Mendocino region using broadband waveform data, *EOS*, Transactions American Geophysical Union, 81, no. 48 (Fall Meet Suppl.), 2000.

Research Studies:
Enhancements to Observational Systems

29 ElarmS-2: Rapid Accurate Alerts across California

Jennifer Strauss, Richard Allen, Ronnie Grapenthin, Margaret Hellweg, Ivan Henson, Ingrid Johanson, H. Serdar Kuyuk, Doug Neuhauser

Introduction

The ElarmS methodology and algorithms are part of the ShakeAlert demonstration system in California, and are also being tested in the US Pacific Northwest and South Korea, and will be implemented for testing in Israel in the coming year. The methodology is a network-based approach to early warning in that it requires several seismic stations to detect P-waves before an alert is issued. The alerts are distributed to test users across California who receive an estimate of the shaking intensity at their location as well as the time until that shaking will start at their location.

The improved production grade E2 algorithm, released last year, improved both the early warning processing speed and the accuracy of the results. This was most apparent during the significant earthquakes (M>=4.5), which ruptured in California over the past year. The algorithm was further improved by investigating a global approach to providing magnitude estimates for early warning using only the P wave data.

Algorithm Performance

Over the last year in California, ElarmS successfully alerted on all significant earthquakes (*M*>=4.5, 10 earthquakes) and generated no false alarms. This includes events in Los Angeles, Santa Rosa, offshore Eureka, and the southern Sierra. The magnitude estimates were within 0.5 magnitude units in all cases.

The largest event was the *M*6.8 event offshore of Eureka. The initial ElarmS magnitude estimate was *M*6.3, with an estimated epicentral location only 7 km from the true location. Locations of small events are often difficult in this region stemming from the fact that the sensors are located onshore, and thus, only to the Eastern side of the rupture, and sparsely distributed. This larger event did not suffer from that effect; ElarmS also alerted on all of the larger (*M*>=4.5) aftershocks.

The speed of the alert depends on the quality of the seismic network around the epicenter. For the *M*5.1 Los Angeles Le Habra event (see Figure 2.29.2) the alert was 4.2 seconds after the origin time, which is typical for events in the Los Angeles region. For the Santa Rosa event, the alert was 6.8 seconds after the origin time, 10.8 s for the southern Sierra event, and 25.7 s for the (offshore) Eureka earthquake. Comparing the performance of ElarmS across the state for a wider range of magnitudes (*M*>=3) the effect of variable seismic network quality is very apparent. The performance is good to excellent in the San Francisco Bay and Los Angeles areas where station coverage is densest. In the greater San Francisco Bay Area, of the 38 *M*>=3.0 events reported by the ANSS, five were missed (all in the Geysers Geothermal Area) and there were no false events. In the Los Angeles region, of the 35 *M*>=3.0 events, four were missed and there were two false events.

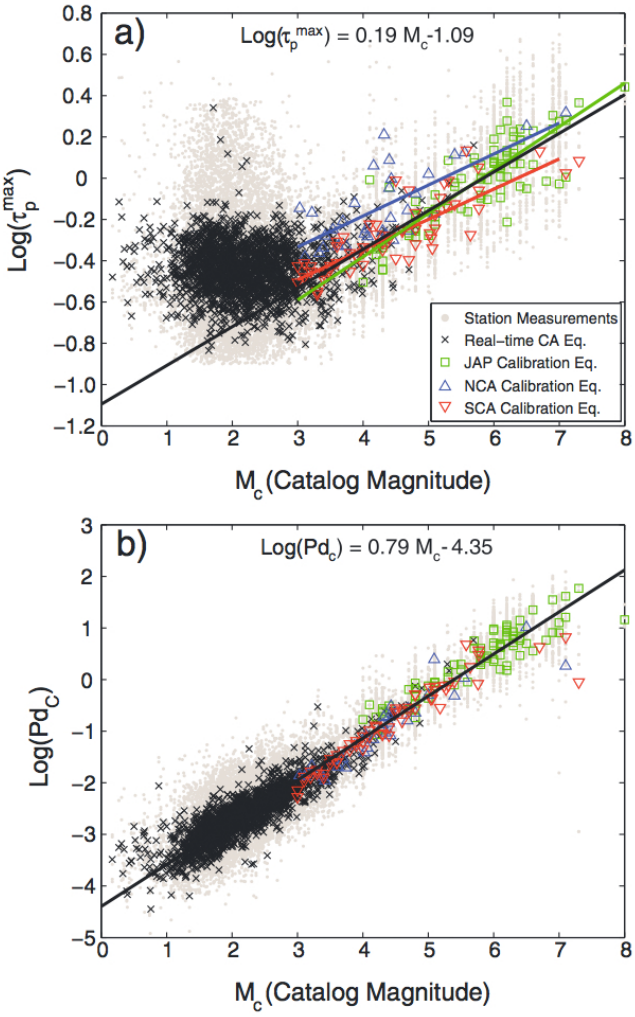

Figure 2.29.1: Scaling relationships between catalog magnitude and (a) τpmax and (b) Pdc. In (a) the best fit lines to the regional data sets are shown with colored lines, and the black line is the best linear fit to all the data excluding the real-time-detected earthquakes (equation shown). In (b) the black line (equation shown) is the least squares multiregression fit to the entire data set and represents our preferred global scaling relationship.

Global Magnitude Estimation

Rapid magnitude estimation is at the heart of Earthquake Early Warning Systems (EEWS). The challenge is to use only a few seconds of the P wave data from a limited number of stations to quickly determine a useful estimate of the earthquake magnitude. To respond to the emergency at hand, it is crucial that these magnitude estimates are as precise as possible (*Kuyuk and Allen*, 2013). For large earthquakes, substantial deviations between the estimated magnitude and the true earthquake's magnitude can lead to erroneous intensity predictions.

We have improved the precision of ElarmS by deriving a

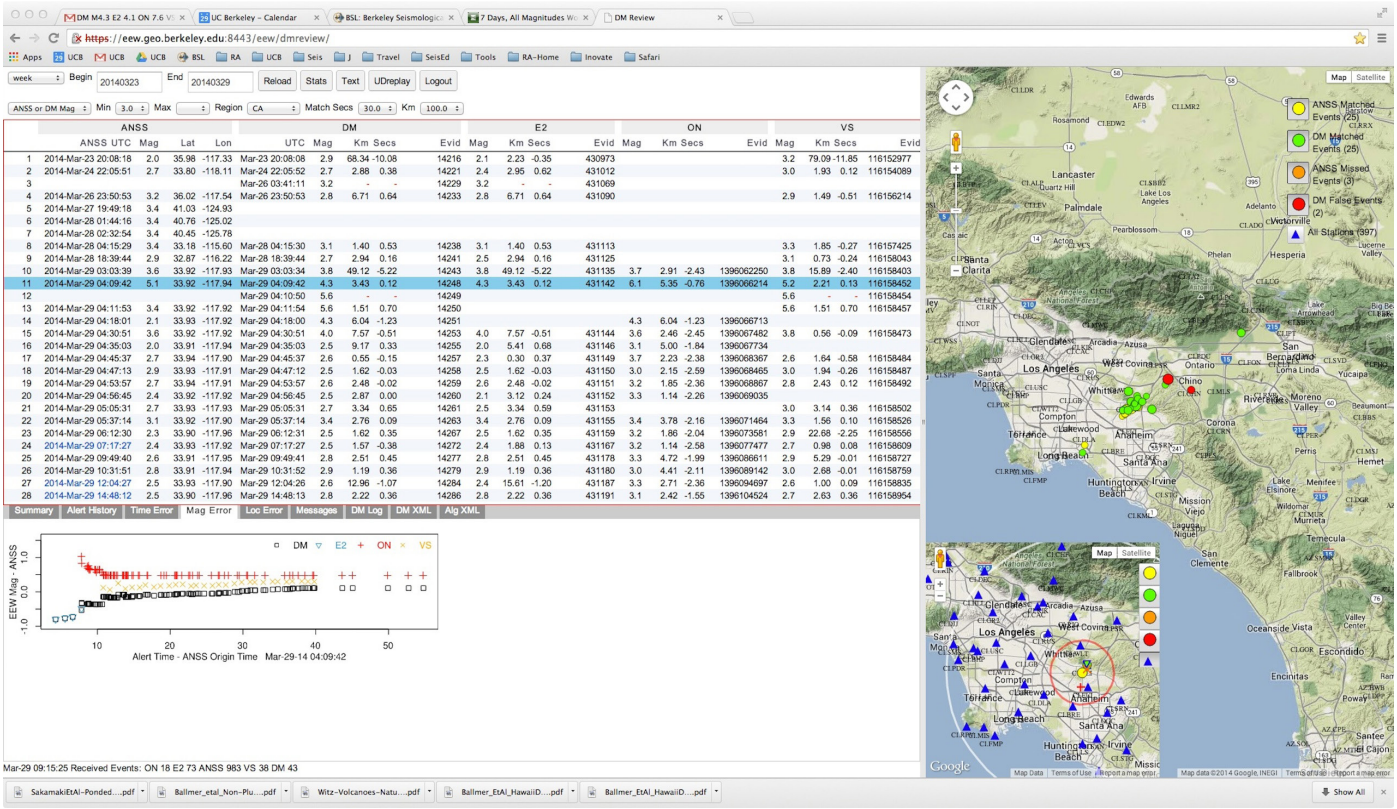

Figure 2.29.2: The Decision Module web-based performance evaluation tool was used to study the overall system response for the La Habra event. This tool aggregates information from all three algorithms individually with the overall ShakeAlert warning information. The E2 algorithm (blue triangle) can be seen in the inset plot bottom left, to have a quicker alert time for this rupture than the other algorithms. The map shows the location of the earthquake and the aftershocks in the region.

global scaling relationship to predict earthquake magnitude from P-wave data, which can be applied to data worldwide. To derive the scaling relationship we used waveform records from past/historic earthquakes and data from the current real-time ElarmS system running in California. Instead of using different scaling relationships for each individual region, we used a global data set and explored various approaches to estimate magnitude from the P-wave data.

Five different methods were investigated to estimate earthquake magnitude from P-wave data. The inclusion of real-time data provided an opportunity to test the methods on smaller earthquakes ($0.1 < M < 3.0$), which have been largely ignored in previous studies. Comparison of τ_p^{max} and Pd-based magnitude estimation methods indicate that Pd scaling is observed for all earthquakes, whereas the frequency filtering required for the τ_p^{max} observation results in sensitivity to only a limited frequency range (M>3.0 for the implementation tested here). We concluded that the best approach to derive EEW magnitude estimates is to use only the Pd parameter and the global scaling relationship

$$MGPd = 1.23\log(Pd) + 1.38\log(E) + 5.39$$

This new method provides smaller RMS errors than existing regional methods based only on Pd. Our results showed that this new technique using only Pd information is robust and delivers the most accurate global magnitude estimates for earthquakes up to $M \sim 7$. Above $M7$, a saturation effect is observed and the application of other finite source type methods is needed.

Acknowledgements

This project is possible thanks to the collaborative efforts of many people working at the CISN operating institutions: UC Berkeley, Caltech, USGS Menlo Park and USGS Pasadena. This work is funded by USGS/NEHERP awards G09AC00259 and G12AC20348, and by the Gordon and Betty Moore Foundation through Grant GBMF3024 to UC Berkeley.

References

Kuyuk, H. S. and Allen, R. M., A global approach to provide magnitude estimates for earthquake early warning alerts, *Geophysical Research Letters*, v. 40, p.6329-6333, 2013.

30 Operational Real-Time GPS-enhanced Earthquake Early Warning

Ronni Grapenthin, Ingrid A. Johanson, Richard M. Allen

Introduction

Moment magnitudes for large earthquakes (M_w>7.0) derived in real-time from near field seismic data can be underestimated due to instrument limitations, ground tilting, and saturation of frequency/amplitude-magnitude relationships. Real-time high-rate GPS resolves the build-up of static surface displacements with the S-wave arrival, thus enabling the estimation of slip on a finite fault and the event's geodetic moment. Here, we present the first operational system for real-time GPS-enhanced earthquake early warning as implemented at the BSL and currently running on data for Northern California. Using synthetic and real-data test cases, we explore its sensitivities to disturbances of *a priori* constraints (origin time, location, fault strike/dip). The work presented here is a continuation of *Grapenthin et al.* (2013a,b).

Data processing

The BSL generates real-time position estimates operationally using data from 62 GPS stations (BARD, PBO, USGS) in Northern California (Figure 2.30.1). A fully triangulated network defines 170+ station pairs for processing with the software trackRT (*Herring et al.*, 2010). The BSL uses G-larmS, the Geodetic Alarm System, to analyze the positioning time series, and determine static offsets and pre-event quality parameters. G-larmS derives and broadcasts finite fault and magnitude information through a least-squares inversion of the static offsets for slip based *a priori* fault orientation and location information. This Python implementation tightly integrates seismic alarm systems (CISN ShakeAlert, ElarmS-2) as it uses their P-wave detections to trigger its processing; quality control runs continuously.

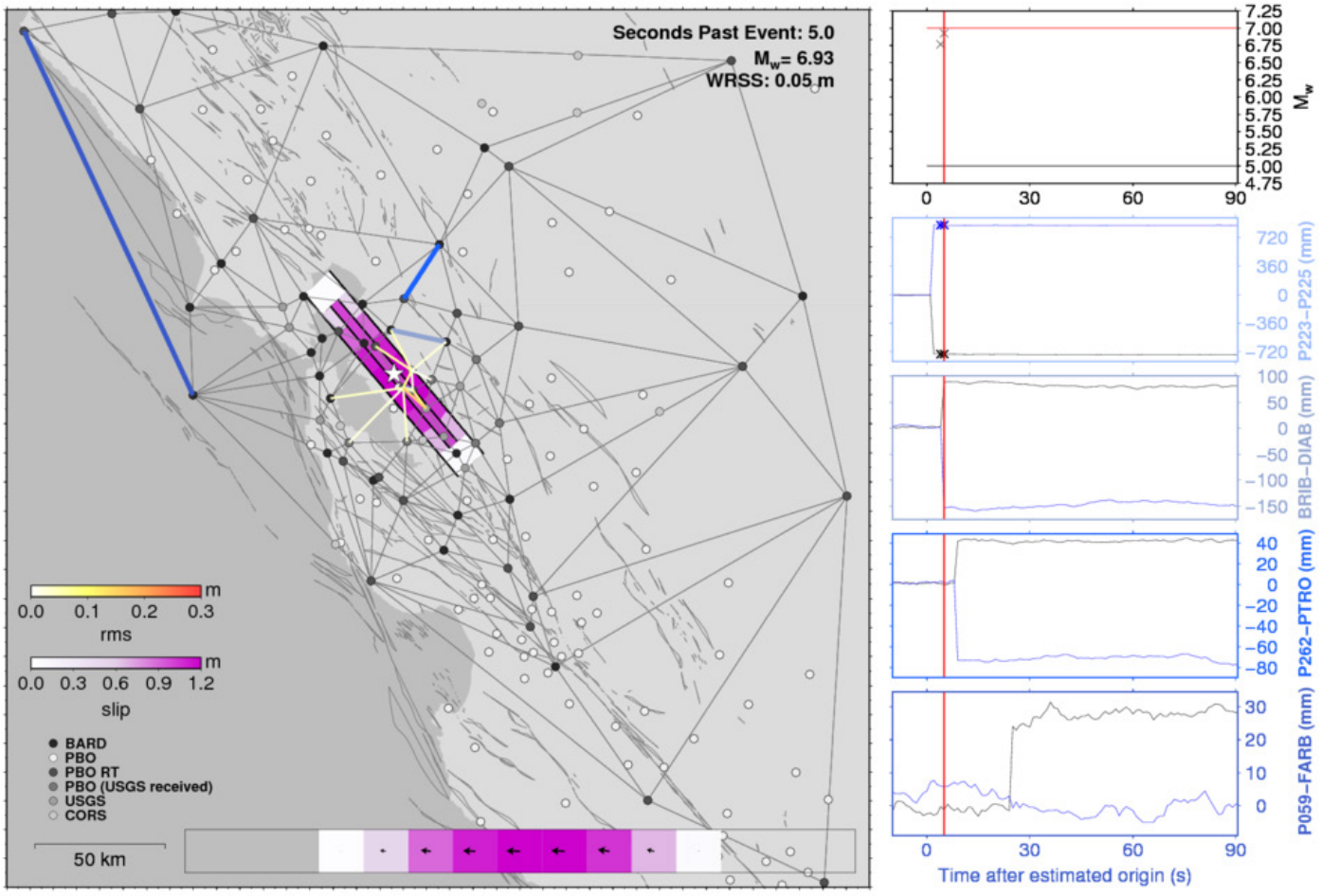

Figure 2.30.1: Snapshot during a real-time test of G-larmS (second solution, five seconds after event); the red line on the right side shows the timing of the snapshot. Top right figure shows the estimated earthquake magnitude for the slip model in purple on the left. Test is based on a simulated *M*7.0 earthquake. G-larmS begins estimating co-seismic offsets (blue and black symbols) after the S-wave arrival. Offsets are updated and input into an inversion for distributed fault slip every second. Testing was run in true real time; synthetic offsets were added to GPS position time series on-the-fly in order to capture true real-time noise and data availability.

Sensitivity Tests

To linearize the finite fault inversion step to increase processing speed we make assumptions about fault orientation and location. We test G-larmS' sensitivity to these assumptions using synthetic tests in which we add modeled offsets due to synthetic ruptures at the Hayward Fault to real-time data (Figure 2.30.1). In individual tests, we randomly perturb pre-defined fault strike and dip, and the event epicenter and origin time, which are derived from a seismic alarm message that triggers our processing.

Here, we show only the impact of misestimates in fault geometry is shown in Figure 2.30.2 (more details in *Grapenthin et al.*, 2014). We vary strike and dip of the model inversion fault by ±20 degrees and ±45 degrees, respectively. The upper row (Hayward 0 km) uses the same forward model as shown in the offset time series in Figure 2.30.1 (rupture from 0-12 km depth) and demonstrates that magnitude recovery (blue) and model fit (red) degrade quickly with small deviations from the nominal values.

The lower row in Figure 2.30.2 (Hayward 5 km) uses a forward model that slips only between 5 and 12 km depth. In the inversion, however, slip over the entire fault width along dip is assumed. While the model fits (red) are generally good for the full range of values, the magnitude recovery (blue) is poor. Asymmetries are due to asymmetries in the network (dip of 140 and 45 degrees are towards West and East, respectively which then constrained the inverse model to have lower overall magnitude.

Conclusions and Outlook

From the tests presented here, and others summarized by *Grapenthin et al.* (2014), we suggest, that slip for an earthquake occurring within small bounds of our assumptions, *i.e.* strike=320±5 degrees, dip=90±3 degrees, mislocation within 3 km orthogonal to surface trace, and surface rupture, will be well recovered for earthquakes within the network (depending on station distribution). Outside of these bounds, however, we may face unphysical slip models and poor magnitude recovery at relatively good fit of the model to the data.

While dense station coverage provides high resolution and, most importantly fast observations, it requires us to sample the parameter space for the non-linear finite slip inversion problem more thoroughly. The most problematic issue is choosing any parameter such that individual (near field) stations end up on the wrong side of the model fault. As the parameter space exploration in real-time cannot be exhaustive unless heavily parallelized, we have to exploit this property in the future. As real-time GPS is sought to contribute improved magnitude estimates within ±0.3 magnitude units and an approximate fault length for ground motion prediction to earthquake early warning, two simplifications are possible: (1) ignoring/down-weighting near-field data at single outlier stations in a dense network that produce significant misfits, (2) placing model faults between station pairs with highest strain. These can be combined and both reduce the complexity of the solution while providing approximate solutions. The trade off between speed and accuracy of the solutions is the subject of future investigation.

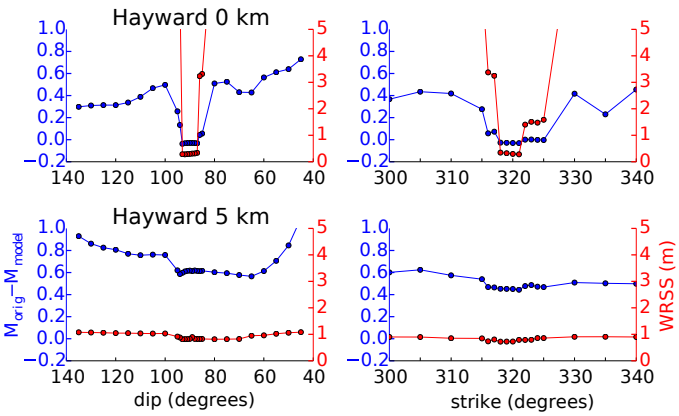

Figure 2.30.2: Sensitivities to wrong assumptions in strike and dip in the inversion. Two forward models (fault from 0-12 km and 5-12 km depth respectively) with 90° dip creating M_w7.0 equivalent slip were inverted for varying dip (left column) and strike (right column). Blue lines indicate magnitude recovery. The red line is the model misfit to the forward model.

Acknowledgements

This work is supported through the Gordon and Betty Moore Foundation, and CISN partners. We use data provided by the Plate Boundary Observatory operated by UNAVCO for EarthScope and supported by NSF (No. EAR-0350028 and EAR-0732947).

References

Grapenthin, R. et al., Operational Real-time GPS-enhanced Earthquake Early Warning, *J. Geoph. Res.*, submitted, 2014.

Grapenthin, R. et al., G-larmS - Integrating Real-Time GPS into Earthquake Early Warning I: Implementation, *BSL Annual Report 2012-2013*, 70-71, 2013a.

Grapenthin, R. et al., G-larmS - Integrating Real-Time GPS into Earthquake Early Warning II: Testing, *BSL Annual Report 2012-2013*, 72-73, 2013b.

Herring, R. T. A. et al., GAMIT/GLOBK Reference Manuals, Release 10.4, *MIT Technical Reports*, 2010.

31 Evaluation of Smartphones as Seismometers

Qingkai Kong, Richard Allen

Introduction

We are building a new seismic network using smartphones. The accelerometers in smartphones can be used to detect ground motion caused by earthquakes. Before we set up the network, we need to understand the capabilities of the smartphones as a seismic recording system. We conducted a series of tests to understand them, including a noise floor test, and shake table tests. The noise floor test shows us that the current smartphones can detect earthquakes larger than magnitude 4 within 10 km of the epicenter, and the shake table tests show us that the smartphones can reproduce the shaking quite well, even without being firmly attached to the shake table.

Noise Floor Test

A noise floor test is performed to understand smartphones' abilities to detect earthquakes. The phones are placed in a very quiet basement of a building on UC Berkeley's campus, ensuring that the signal the phones record are from internal noise of the phone and the environmental noise of the surrounding area. Altogether, we recorded about one month's noise data for each type of phone, and then we calculated the noise floor of the smartphones using the method described in *McNamara* (2004). The earthquake data showed in the plot are from *Clinton et al.* (2002).

Figure 2.31.1 shows the noise floor test results. Earthquakes above the noise floor of the phones can be recorded by the smartphones. If the earthquake is below the noise floor, then the earthquake signal will be buried into the noise.

The noise floors of the smartphone are divided into two groups based on the release time, represented by light blue and red color. The blue color noise floors are from phones released before 2012, and the red color noise floors are from phones released between 2012 and 2013. As the technology improves, one starts to see the improvement of the accelerometers across the smartphones. The best quality accelerometers in the tested phones can see earthquakes above magnitude 4 within 10 km of the epicenter.

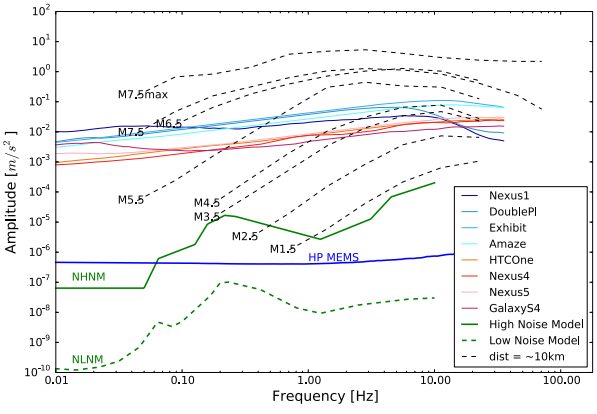

Figure 2.31.1: Noise floor plot of the smartphones. The dotted black lines represent different magnitude earthquakes' signals from within 10 km of the epicenter, as obtained by John Clinton. The green solid and dotted lines are new high noise models (NHNM) and new low noise models (NLNM) of the earth (*Peterson,* 1993). The blue solid line at the bottom is the HP MEMS sensor as a reference line of the potential future sensors. The blue and red lines are the noise floors of the different smartphones whose brands are shown in the legend

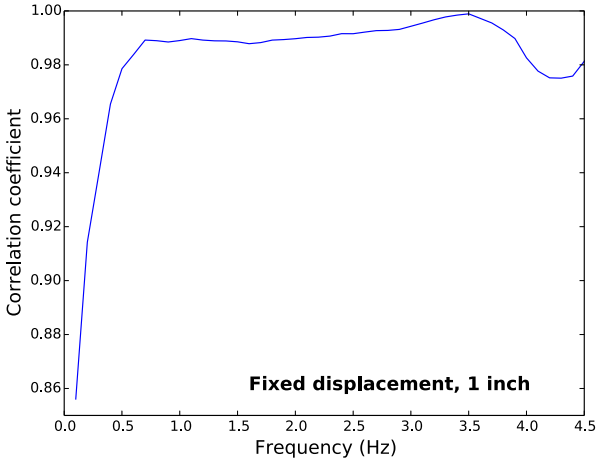

Figure 2.31.2: Correlation coefficient plot of sine wave tests with fixed displacement (1 inch) and different frequencies. The phones are fixed on the shake table, and for each frequency sine wave test, the recording time is 30 seconds. The correlation coefficient is calculated using the Pearson correlation coefficient between the signal recorded by the smartphone and that recorded by a high quality accelerometer attached on the shake table.

The HP MEMS sensor has quite a low noise floor, even comparable to the high quality traditional seismic instrument. Thus, we are hoping the noise floor of the smartphones will continue to drop.

1-Dimensional Shake Table Test

We use a small shake table to test the phone's ability to record and reproduce the shaking generated by the shake table. This shake table is 1 dimensional and can generate both sine waves and converted seismograms. The following are some results from the tests.

The first case we tested was when the smartphones are fixed on the shake table (using a clamp or putty), the smartphones can reproduce the signals quite well. We can see from Figure 2 that most of the correlation coefficients are above 0.98, which shows that the phone-recorded signals reproduce the real motion quite well. The relatively low coefficient below 0.5 Hz is due to the small amplitudes when using a fixed displacement and a small frequency.

The second test was with smartphones placed freely on the shake table. The future network will consist of smartphones

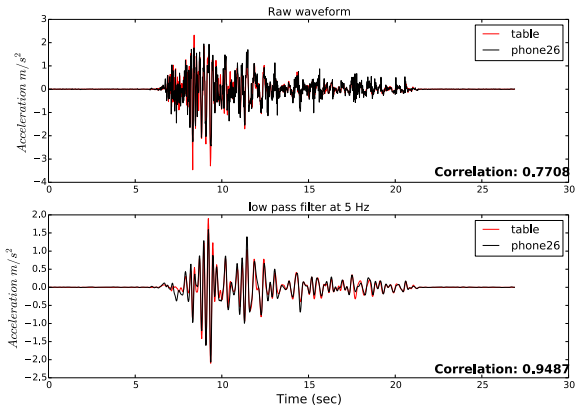

Figure 2.31.3: Waveform recorded by one Samsung Galaxy S4 (phone 26, black color) and high quality accelerometer on the shake table (red color). The top figure is the raw waveform, and the bottom figure is the filtered data (low pass at 5 Hz). This waveform is from one horizontal component of one station during the M_w 6.9 Loma Prieta earthquake, the epicentral distance is 10 km.

put freely on a table or carried by their owners. Therefore, the behavior of the smartphones not rigidly attached to the shake table is also studied.

Figure 2.31.3 shows the raw and filtered waveform from one test. This raw waveform is converted from one component of a station recording the M_w 6.9 Loma Prieta earthquake. The smartphone used in this test was put freely on the shake table, so that the phone can slide when the shaking is large. We can see it can recover the signal very well, and the content below 5 Hz has a correlation coefficient about 0.95.

We also use a one second sliding time window to extract two features from filtered data, as can be seen from Figure 2.31.4. The two features we extracted are zero crossings (when the signal across the zero baseline, we count 1, and then add this count up within the time window, so this parameter is related with frequency) and maximum acceleration (absolute value of the acceleration) from each one second window. Then we compare these features with those extracted from the high quality accelerometer on the shake table. We can see that during the duration of the earthquake, the zero crossings differences between the smartphone recordings and that of the high quality accelerometer are around zero, and the maximum acceleration differences are less than 0.4 m/s^2.

Conclusions

We showed here that smartphones can be used to record earthquake signals and those data can be used to extract useful information about the earthquake, but there are still a couple of issues that need to be addressed. When using the sliding window to extract features from the signal, the amplitude information will under estimate the real amplitude when the phone slides. Characterizing the sliding behavior will help the seismic applications of the smartphone network in the future, such as Earthquake Early Warning.

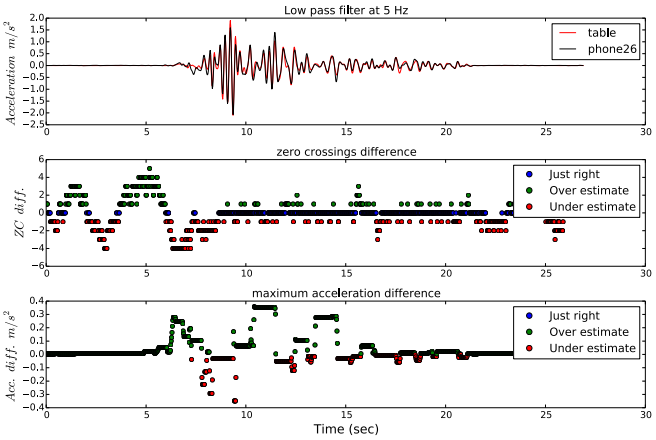

Figure 2.31.4: The top figure is the filtered waveform, the middle figure is the comparison of the zero crossings. The blue dots show when the smartphone and accelerometer have the same value; green dots show where the smartphone value is greater than the raw waveform; red dots show where the smartphone value is less than the raw waveform. The bottom figure shows the difference between the maximum acceleration.

Acknowledgements

This project is funded by Deutsche Telekom. We thank Deutsche Telekom for funding and providing all of the smartphones and developing the applications. Also, we thank Pacific Earthquake Engineering Research Center (PEER) for providing us both the 1-Dimensional and 3-Dimensional shake table.

References

Clinton, J. F., and Heaton, T. H., The potential advantages of a strong-motion velocity meter over a strong-motion accelerometer, *Seismological Research Letters,* 73, 332–342, 2002.

Clinton, J. F., Modern Digital Seismology - Instrumentation, and Small Amplitude Studies for the Engineering World, *Ph.D. Thesis*, California Institute of Technology, 2004.

McNamara, D. E. and Buland, R. P., Ambient Noise Levels in the Continental United States, *Bulletin of the Seismological Society of America*, 94 (4), 1517-1527, 2004.

Peterson, J., Observations and modeling of seismic background noise, *US geological Survey*, open file report 93–322, 1993.

32 High-rate GPS Records Reveal Basin Amplification in the San Joaquin Delta

Ingrid Johanson

Introduction

The M_w 6.9 Ferndale earthquake occurred off the coast of Northern California, near the Mendocino Triple Junction. The large strike-slip earthquake was sufficiently offshore, such that no reported damage or injuries occurred. Nonetheless, it was widely felt throughout coastal Northern California. Aftershocks suggest a northeast striking fault plane, oriented such that the California coast is roughly perpendicular to the rupture plane. Accordingly large amplitude Love waves were observed at California seismic stations. These long-period, large-amplitude surface waves were also detectable at GPS stations in the Bay Area and prompted an examination of GPS data throughout Northern California.

Data Processing

Data were processed from a total of 269 GPS stations from the Bay Area Regional Deformation (BARD) network, the Plate Boundary Observatory (PBO) and USGS, Menlo Park's network. Pairs of stations were processed individually using Track, a high-rate GPS processing algorithm developed at MIT alongside GAMIT/GLOBK (*Herring et al.*, 2010). Track is a network-based processing algorithm, hence it determines relative motion between multiple rovers and a reference site. A processing approach using a single rover and reference (one pair) was used for this study because it allows the motion of each GPS station to be determined relative to only the closest other stations. Common noise sources, in particular atmospheric noise, will then cancel out. As a result, higher precision motions can be detected than in a network solution that includes long baselines.

After processing each pair of stations to determine their relative motion, a network adjustment is performed to transform these into the absolute motion of each station. The inverse problem is underdetermined and so some type of constraint is required to perform the transformation. Potentially a single station could be held stationary and all motions would be transformed to be relative to a single stable site. However, high-rate GPS data do not have insignificant noise, even at the best stations, and a single station constraint would propagate that noise to all the others, essentially doubling their noise levels. A stable network centroid was chosen as a suitable constraint instead. This has the advantage that it averages through the motions at all stations, such that the noise level of the centroid, which is propagated to all stations, is reduced by $1/\sqrt{N}$, where N is the number of pairs in the network adjustment.

The appearance of the Love waves in the resulting GPS timeseries is improved by bandpass filtering. This removes the low frequency portion of the flicker noise spectrum attributable to atmospheric errors and signal multipath. When compared to broadband seismic records at stations where BARD network GPS sites are co-located with Berkeley Digital Seismic Network (BDSN) broadband seismometers, it is apparent that the centroid constraint adequately approximates an absolute reference frame and that the filtered results match many of the same features in the seismic data, even down to the 2–3 mm amplitude level (Figure 2.32.2).

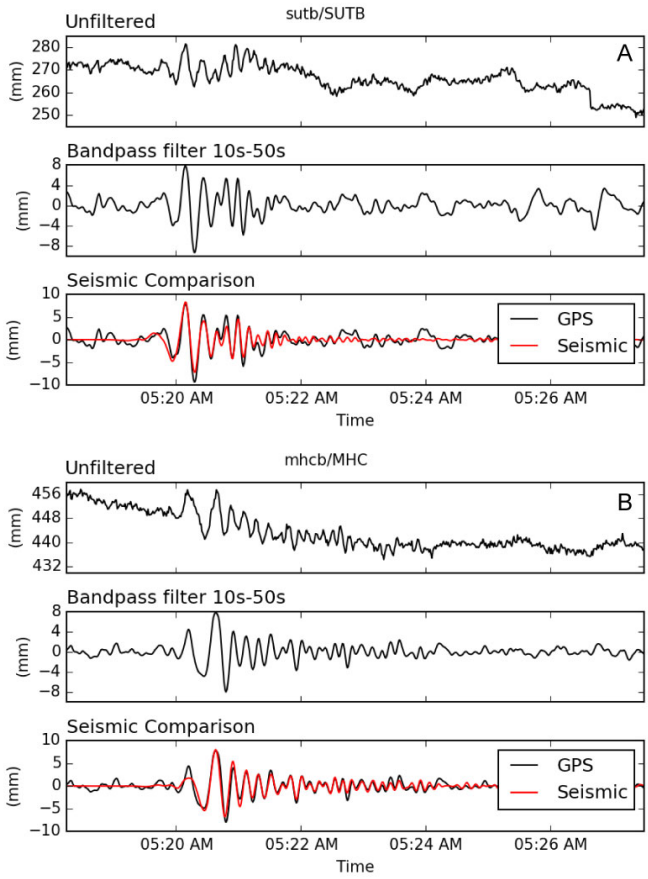

Figure 2.32.1: Comparison of BARD network high-rate GPS timeseries and data from broadband seismometers in the BDSN network. Transverse component of motion is shown (motion perpendicular to azmuthal direction to the earthquake epicenter).

Results and Discussion

The motion at each GPS station is rotated into the transverse and radial components and it is observed that nearly all the motion is in the transverse component. This can be seen quite clearly in Figure 2.32.2, where the peak dynamic displacements in the transverse direction are an order of magnitude larger than in the radial direction. Figure 2.32.2A, in particular, clearly shows the radiation pattern of Love waves propagating in a direction perpendicular to the rupture plane. However, neither Figure 2.32.2C or 2D shows a similar distribution of high radial displacements at 45° to the rupture plane that might be associated with Rayleigh waves.

While the distribution of peak dynamic displacements is dominated in long periods by the radiation pattern, at shorter periods other patterns become visible. In particular, at higher frequencies, stations in the San Joaquin Delta region show higher peak dynamic displacements than those in surrounding areas, as well as longer duration shaking (Figure 2.32.3).

The stations with higher amplitudes on the transverse component also have increased amplitudes on the radial component, suggesting that seismic waves were scattered within this area or reflected off of basin boundaries, transferring energy from the transverse to radial components. The increased duration of shaking at Delta region stations further supports the interpretation that energy is being trapped within a basin.

In general the soft sediments of the Central Valley easily explain the increased amplitudes and longer shaking duration for many of the affected stations. However, sites in the San Joaquin Delta region are more strongly affected than those elsewhere in the Central Valley. Furthermore, two amplified stations are located in the Montezuma Hills; a geologic province that is distinct from the Delta, but nonetheless contains unsorted Pleistocene silt and sand, known as the Montezuma formation (*Strand and Koenig*, 1965). That they also have energy scattered into the radial component, could suggest that the structure responsible underlies both regions.

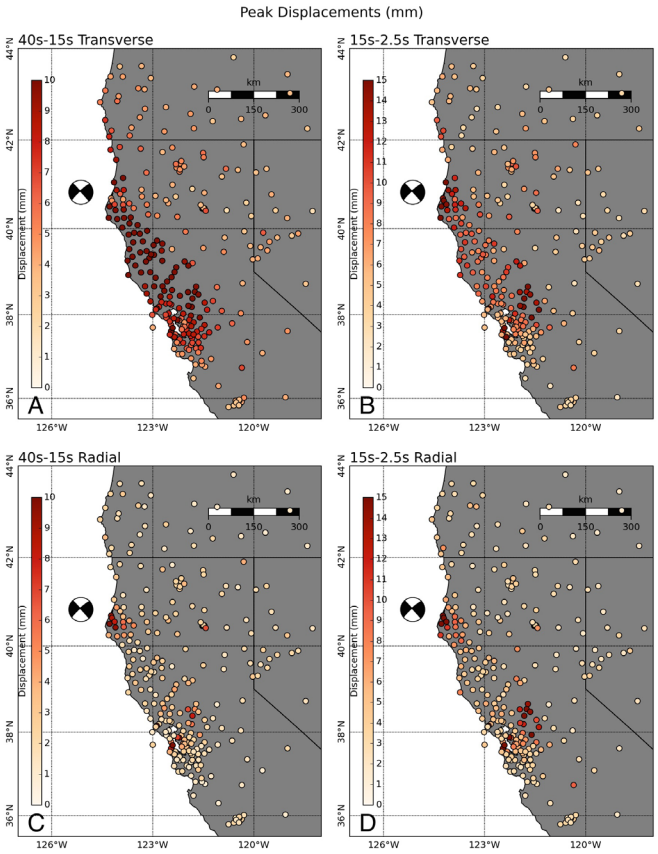

Figure 2.32.2: Peak dynamic displacements (colors) for transverse (A and B) and radial (C and D) components of motion. Left and right sides have been bandpass filtered to the limits shown. The NCSS moment tensor is plotted at earthquake epicenter.

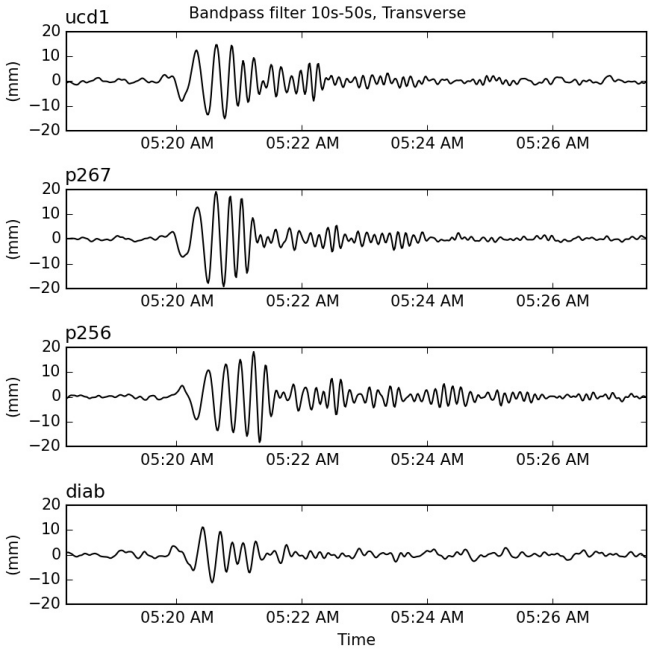

Figure 2.32.3: Comparison of San Joaquin Delta region sites (ucd1, p267, p256) and a nearby hard rock site (diab), showing higher overall amplitudes of shaking in the Delta region and longer duration wave trains.

These data provide an opportunity to probe the structure of Northern California in a way that is not possible with the much more sparsely distributed broadband seismic stations. While GPS is less sensitive than broadband seismometers, when a large earthquake generates high dynamic displacements, the increased resolution due to higher spatial density will be very valuable.

References

Herring, T. A., R. W. King, and S. C. McClusky, GAMIT: GPS Analysis at MIT - Release 10.4, MIT, 2010.

Strand, R. G., and J. B. Koenig, Geologic map of California: Sacramento sheet, California Division of Mines and Geology, (1:250,000), 1965.

33 Predictability of Hydraulic Head Changes and Characterization of Aquifer System Properties from InSAR-Derived Ground Deformation

Estelle Chaussard, Roland Bürgmann

Introduction

Groundwater management relies mostly on ground-based observations, which are expensive and spatially limited. Here, we demonstrate the benefits of space-derived ground deformation measurements for characterization of aquifer properties and groundwater levels. We use Interferometric Synthetic Aperture Radar (InSAR) time-series analysis of ERS, Envisat, and ALOS data to resolve 1992-2011 vertical ground deformation in the Santa Clara Valley, California. T-mode Principal Component Analysis successfully isolates temporally variable deformation patterns embedded in the multi-decadal time series. The data reveal uplift at 4 mm/yr between 1992–2000 and >1 mm/yr in 2000–2011, illustrating the end of the poroelastic rebound following recovery of hydraulic heads after the 1960s low stand. Seasonal elastic deformation with amplitude of 3 cm is observed over the confined aquifer sharply partitioned by the Silver Creek Fault (SCF). Integration of this deformation with hydraulic head data enables characterization of basin-wide aquifer system storativity. Additionally, we show that after a period of calibration, InSAR can be used to accurately characterize water level changes without well measurements.

Approach

We use over 100 SAR acquisitions from the ERS, Envisat, and ALOS satellites to produce ~300 interferograms covering 1992–2011. We then invert a network of small-to-moderate spatial and temporal baselines interferograms, following the Small Baseline (SBAS) technique (*Berardino,* 2002), to retrieve time-dependent ground displacement. We focus here on the vertical deformation that we isolate by combining ascending and descending viewing geometries (*Wright et al.,* 2004).

To separate transient patterns embedded in long-term trends without involving *a priori* models we use T-mode Principal Component Analysis (TPCA), a mathematical transformation of a set of inter-correlated variables into a new set of uncorrelated variables. The Principal Components (PCs) are a transformation of the time-dependent data into a set of representative spatial patterns of deformation, shown by the scores maps, which highlight a signal coherent in space but variable in time (Figure 2.33.1c). The variable gains through time are shown by the eigenvectors (Figure 2.33.1b).

Results

The change of slope of the Scree plot (Figure 2.33.1a) indicates that only the first three PCs need to be kept to represent over 90% of the data variance. The first PC corresponds to the longer-term deformation. Positive scores (red on Figure 2.33.1c) are observed in the Evergreen and Santa Clara basins. The eigenvector time series (Figure 2.33.1b, top) shows an increase (corresponding to uplift in positive-score areas) between 1992–2000 and remains nearly constant during 2000–2011. This pre-2000 uplift at 4 mm/yr can be either correlated with hydraulic head changes (short-period elastic aquifer deformation), or can be associated to delayed poroelastic rebound of aquitards due to their low hydraulic conductivity resulting in a lag of hydraulic heads compared to aquifers (*Terzaghi*, 1925). In the Santa Clara Valley, after the intense groundwater extraction of 1920–1965, artesian levels were reached in the early 1990 (*Galloway et al.,* 1999), which suggest that the post-1992 deformation is due to delayed aquitards poroelastic rebound.

The second and third PCs correspond to seasonal deformation as shown by their eigenvector time-series (Figure 2.33.1b bottom). PC2 consists of spatially extensive deformation encompassing most of the confined aquifer west of the SCF with an average peak-to-peak amplitude of ~2-2.5 cm (Figure 2.33.1c score map PC2). Peaks in PC2 occur immediately after rainfall, also confirmed by cross-correlation analysis, which suggests elastic deformation of a highly permeable aquifer system. PC3 is limited to a ~3 km wide region west of the SCF and has an average peak-to-peak amplitude of ~0.5-1 cm (Figure 2.33.1c score map PC3). Peaks in PC3 occur with a time lag of ~105 days, suggesting that it corresponds to a later phase of deformation, possibly due to delayed aquitards deformation.

Using hydraulic head data from the Santa Clara Valley Water District at 50 wells we normalize the seasonal ground deformation (PC2+PC3) by the head changes to constrain the storativity, *S* (*Burbey*, 2001). The storativity represents the volume of water taken into or released from storage per unit decline in hydraulic head, per unit area, and helps define sustainable pumping rates. *S* is roughly constant across most of the aquifer at ~2×10^{-3} (blue on Figure 2.33.2a), in agreement with values derived from traditional techniques (*Poland and Ireland*, 1988). Higher storativity near the shoreline, over the Holocene Bay mud (red on Figure 2.33.2b, constrained by one well) and around the SCF (constrained by three wells) are highlighted by this basin-wide study, with values representative of clays.

Finally, we evaluate how well seasonal water level changes can be predicted from the observed deformation and calculated storativity. We estimate the storativity using 1995–2001 deformation and water data, the first time period with good InSAR temporal sampling, and examine how well we can predict 2006–2011 hydraulic head changes from InSAR data of that period (second period with good temporal sampling). The mean prediction accuracy for each 2006–2011 season, defined as 100–(100*(observations-predictions)/observations) (*Wu et al.,* 1995) is of 70% for the entire basin (Figure 2.33.2b). The best accuracy is achieved in the confined aquifer west of the SCF, where the deformation and head changes are the largest.

Conclusion

We characterize the 1992–2011 hydrologically induced

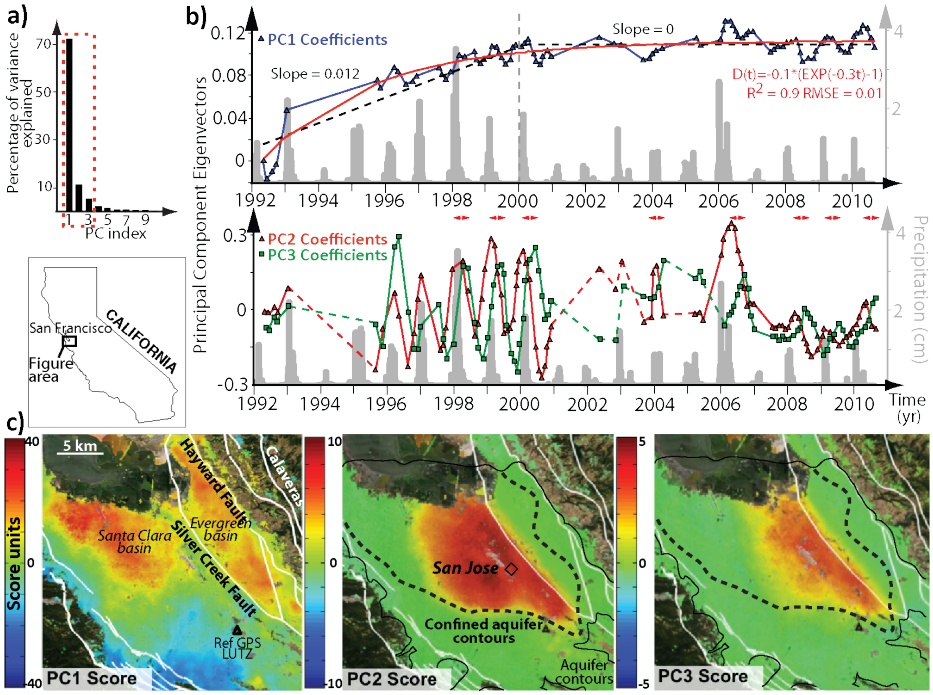

Figure 2.33.1: TPCA results for 1992–2011 InSAR SBAS vertical ground velocity in the Santa Clara Valley. a) Scree plot of the percentage of variance explained by each PC. b) Eigenvectors of PC1 (top) and PC2 and 3 (bottom) showing the temporal variability of the PCs deformation patterns. The red double arrows highlight PC2 and PC3 time lag. Grey bars show monthly precipitations. c) Scores maps showing the spatial patterns of the deformation of PC1, 2 and 3 (left to right). The score maps are converted to deformation by multiplying them by the eigenvector at a given time.

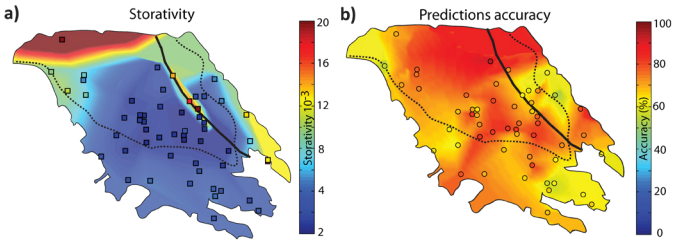

Figure 2.33.2. a) Aquifer storativity, from the ratio of seasonal deformation and head changes at the 50 wells (squares). b) Map of the mean prediction accuracy of the 2006-2011 seasonal InSAR heads compared to the measured 2006-2011 seasonal hydraulic heads.

ground deformation in the Santa Clara Valley, California, using InSAR time-series analysis. Poroelastic rebound of the aquifer system following recovery of hydraulic heads after the 1960s low stand occurs mostly prior to 2000, leading to uplift one order of magnitude smaller than its preceding subsidence.

Using TPCA we isolate temporally variable deformation embedded in the multi-decadal time-series without *a priori* constraints, which show the potential of TPCA for improving characterization of complex deformation. In the Santa Clara Valley two patterns of seasonal deformation exist, both sharply partitioned by the SCF, illustrating that the fault is a barrier to across fluid flow. Combining this seasonal deformation with hydraulic head data, enables characterizing of basin-wide aquifer system properties.

Finally, we show that InSAR-derived ground deformation can be used to evaluate basin-wide water level changes without well measurements with an accuracy of ~70%, which demonstrates its benefits for groundwater management.

Acknowledgements

We thank NASA for support through grant NNX12AQ32G and we thank the Santa Clara Valley Water District for their close collaboration and for sharing the hydraulic head data.

References

Berardino, P., G. Fornaro, R. Lanari, and E. Sansosti, A new algorithm for surface deformation monitoring based on small baseline differential SAR interferograms: *IEEE Transactions on Geoscience and Remote Sensing*, v. 40, no. 11, p. 2375–2383, doi:10.1109/TGRS.2002.803792, 2002.

Wright, T. J., B. E. Parsons, and Z. Lu, Toward mapping surface deformation in three dimensions using InSAR: *Geophysical Research Letters*, v. 31, no. 1, doi:10.1029/2003GL018827, 2004.

Galloway, D., D. R. Jones, and S. E. Ingebritsen, Land subsidence in the United States. US *Geological Survey Circular 1182*, 1999.

Terzaghi, K., Principles of soil mechanics: IV; settlement and consolidation of clay: *Erdbaummechanic*, v. 95, no. 3, p. 874–878, 1925.

Burbey, T. J., Stress-Strain Analyses for Aquifer-System Characterization: *Ground Water*, v. 39, no. 1, p. 128–136, 2001.

Poland, J. F., and R. L. Ireland, Land subsidence in the Santa Clara Valley, California, as of 1982: U.S. *Geological Survey Professional Paper*, 497-F , 1988.

Wu, G., M. Baraldo, and M. Furlanut, Calculating percentage prediction error: a user's note: *Pharmacol Res*., v 32, no. 4, p241-8, 1995.

34 TremorScope: Imaging the Deep Workings of the San Andreas Fault

Roland Bürgmann, Richard Allen, Douglas Dreger, Robert Nadeau, Barbara Romanowicz, Taka'aki Taira, Margaret Hellweg

Introduction

Until recently, active fault zones were thought to deform via seismic slip during earthquakes in the upper, brittle portion of the crust, and by steady, aseismic shear below. However, in the past decade, this view has been shaken by seismological observations of seismic tremor deep in the roots of active fault zones. First recognized on subduction zones in Japan and the Pacific Northwest, tremor has also been found to be very active on a short section of the San Andreas to the southeast of one of the most densely monitored fault segments in the world, near Parkfield (*Nadeau and Dolenc*, 2005). This deep (~20–30 km) zone of activity is located right below the nucleation zone of the great 1857 Fort Tejon earthquake. Thus, learning more about the temporally and spatially complex faulting processes in this zone may help us better understand the conditions that lead to such large ruptures.

The Project Plan and Implementation

The tremor source region is southeast of existing seismic networks around Parkfield, along the San Andreas Fault. We are adding eight seismic stations, the TremorScope (TS) network, in this area to complement existing instrumentation.

In the past year, TS activities have been concentrated on drilling, casing and instrumenting the four boreholes. In the summer of 2013, we hosted walk-throughs for prospective drilling companies in preparation for their bids. Drilling began in November, following the selection of the drilling company.

Since the landowner at seismic station TPPG had leased acreage near our site for oil exploration, we sought an alternative and found a site near the San Andreas Fault near the intersection of Bitterwater Road and Bitterwater Valley Road (Figure 2.34.1). Drilling at all four sites, TRAM, TRAY (Figure 2.34.2), TCAS and TSCS was completed in early April. TSCS

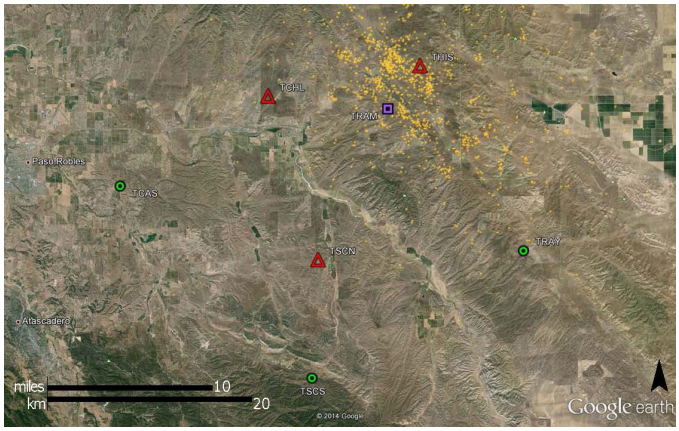

Figure 2.34.1: Google Earth image showing the locations of the TremorScope stations. Circles and triangles indicate borehole and surface sites, respectively. The square marks TRAM, the site with both surface and borehole deployments.

Figure 2.34.2: Drilling commences at TRAY in early March.

is 750 ft deep and from a depth of 350 ft onward is in solid rock. The other three boreholes are 1000 ft deep and mostly in softer material. All exhibit very little drift. The boreholes are cased with Schedule 21 PVC, with an inner diameter of 6 inches. We hope this proves to have less electrical noise than a steel casing would, and also that it provides more protection from lightning strikes and lower resonances.

Huts have been installed over the boreholes to offer a mounting surface for the solar panels which will power the stations, but also to provide protection for the equipment from the sun and cattle (Figure 2.34.3). The borehole sites will have an accelerometer installed at the surface in the hut.

TS data are used in real-time earthquake monitoring (see Operational Section 4.7), as well as for tremor studies. Data from the four surface stations are now being archived and analyzed. In addition to contributing to investigations of tremor, the TS stations also improve our ability to characterize the seismicity in the region. Figure 2.34.4 shows details of the rupture of the December 12, 2013 M_w 4.1 earthquake in nearby Lost Hills, CA, determined from TS data using empirical Greens function deconvolution.

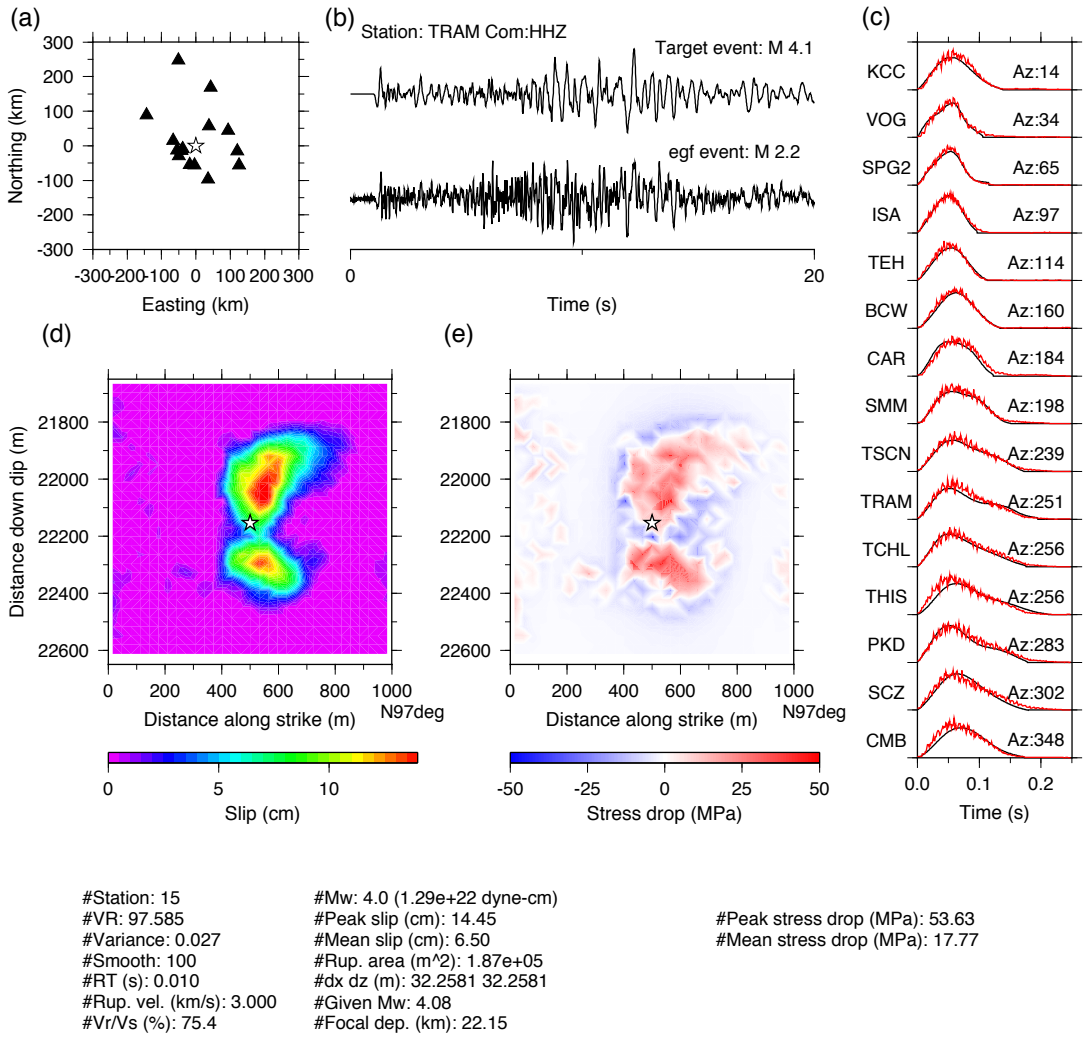

#Station: 15
#VR: 97.585
#Variance: 0.027
#Smooth: 100
#RT (s): 0.010
#Rup. vel. (km/s): 3.000
#Vr/Vs (%): 75.4

#Mw: 4.0 (1.29e+22 dyne-cm)
#Peak slip (cm): 14.45
#Mean slip (cm): 6.50
#Rup. area (m^2): 1.87e+05
#dx dz (m): 32.2581 32.2581
#Given Mw: 4.08
#Focal dep. (km): 22.15

#Peak stress drop (MPa): 53.63
#Mean stress drop (MPa): 17.77

Figure 2.34.4: Triggered tremor in the surface waves of the April 11, 2012, M8.6 earthquake which occurred off the West Coast of Northern Sumatra. Tremor is apparent in the records of HRSN stations CCRB and MMNB as well as at TremorScope station TSCN.

Figure 2.34.3. Installation of the surface hut at TRAM. Solar panels will be mounted on the south-facing roof. The door is 8 ft tall to allow access for installation of borehole equipment.

Perspectives

Data from the TremorScope project are improving earthquake monitoring in the region south of Parkfield. Insights from the project will also contribute to understanding tremor and slip in other regions of the world that are not nearly as accessible. Should a great San Andreas earthquake occur during this experiment, the network will also provide unprecedented and exciting insights into the seismic rupture process. More information about the Tremorscope Project can be found at http://seismo.berkeley.edu/research/tremorscope.html

Acknowledgements

This work is funded by grant 2754 from the Gordon and Betty Moore Foundation.

References

Nadeau, R., and D. Dolenc, Nonvolcanic tremors deep beneath the San Andreas fault, *Science*, 307, 389, doi:10.1126/science.1107142, 2005.

35 Normal Modes: Investigating Signal and Noise Phenomena Across Instrument Types and Deployment

Margaret Hellweg, Taka'aki Taira, Robert A Uhrhammer, Eiichiro Araki (JAMSTEC), Horst Rademacher, Murray McGowan (Guralp)

Introduction

Whether a seismic signal in a certain frequency band can be detected in a recording depends primarily on four factors: the amplitude of the signal at the site, the conditions at the site which affect the ambient noise in that band, the sensitivity and self-noise of the sensor in the band, as well as the sensitivity and self-noise in the digitizer in the band. For the very long period band, between 1.0 and 5.5 mHz, the normal modes provide an excellent signal for exploring the effects of the latter three contributions, since after a large or great earthquake, their amplitudes are similar all over the earth.

The Data

In the past, observatory equipment in an observatory setting were required to observe them. We observed normal modes in the 1.0-5.5 mHz band with good signal-to-noise ratio in the aftermath of the M_w 8.3 Sea of Okhotsk deep earthquake on May 24, 2013 at many stations of the Berkeley Digital Seismic Network and at other stations in other networks. They are equipped with a variety of sensors, including those with a flat passband extending to frequencies lower than the normal modes, and digitizers (Table 2.35.1). They are also deployed in a variety of geologic settings, including cabled ocean bottom stations, like MOBB in California, the Japanese cabled "Dense Ocean-Network for Earthquake and Tsunamis (DONET)" and the IODP seafloor borehole in the south of Japan (Table 2.35.1). The sites have varying physical infrastructure and site preparation.

Observations

Figure 2.35.1 allows one to explore the factors that contribute to the observation of the normal modes on vertical and horizontal components at a suite of amplitudes of excitation. It shows normal mode spectra from a suite of recent earthquakes with magnitudes between 7 and 9.1. Signal-to-noise ratios for the normal modes for a given magnitude of earthquake vary more by deployment type and location than by instrumentation.

Table 1. Stations, equipment and deployment

Station	Seismometer	Data Logger	Deployment
BKS	STS1	Q330	Tunnel
CMB	STS1	Q330	Vault
HOPS	STS1	Q330	Vault
KCC	STS1	Q330	Tunnel
MHC	STS1	Q330	Pier in buliding
SAO	STS1	Q330	Vault
SCZ	STS1	Q330	Old adit (10m)
ORV	STS1	Q330	Pier in building
YBH	STS1	Q330	Old adit (35m)
BDM	STS2	Q330	Old adit (150m)
BRK	STS2	Q330	Pier in building
CVS	STS2	Q330	Wine tunnel
FARB	STS2	Q330	Vault
GASB	STS2	Q330	Vault
HUMO	STS2	Q330	Old adit (100m)
JCC	STS2	Q330	Vault
JRSC	STS2	Q330	Vault
MNRC	STS2	Q330	Vault
MOD	STS2	Q330	Tunnel
PACP	STS2	Q330	Surface vault
PKD	STS2	Q330	Vault
WDC	STS2	Q330	Tunnel (50m)
WENL	STS2	Q330	Wine tunnel
HATC	STS2	Q330	TA vault
HAST	STS2	Q330	TA vault
HELL	STS2	Q330	TA vault
MCCM	STS2	Q330	Vault
RAMR	STS2	Q330	TA vault
SUTB	STS2	Q330	TA vault
BRIB	CMG-3T	Q330	Posthole (10m)
BL67	CMG-3T	Q330	Surface vault
TCHL	CMG-3T	DM-24	TS vault
THIS	CMG-3T	DM-24	TS vault
TRAM	CMG-3T	DM-24	TS vault
TSCN	CMG-3T	DM-24	TS vault
VAK	CMG-3T	Q330	Tunnel
WOL	CMT-3T	DM-24	Borehole (80m)
MOBB	CMG-1T	DM-24	OBS
BHC2	CMG-3T	DM-24	OB borehole (910m)
KMB05	CMG-3T	DM-24	OBS
KMB08	CMG-3T	DM-24	OBS
KMC09	CMG-3T	DM-24	OBS

Figure 2.35.1: Normal modes in the frequency band between 1.5 and 5.5 mHz. The top panel shows normal modes from the vertical channels. For the bottom panel, the normal mode spectra from the two horizontal channels have been summed. All spectra are normalized to 1. Where the traces are missing, no data are available from that station for the earthquake. Station equipment and deployment conditions are listed in Table 2.35.1.